



Algorithm Theoretical Basis Document (ATBD)
for the
Conical-Scanning Microwave Imager/Sounder (CMIS)
Environmental Data Records (EDRs)

Volume 5: Precipitation Type and Rate EDR

Version 1.2 – 15 March 2001

Solicitation No. F04701-01-R-0500

Submitted by:
Atmospheric and Environmental Research, Inc.
131 Hartwell Avenue
Lexington, MA 02421-3126

With contributions by:
Grant W. Petty^{*}, Sid-Ahmed Boukabara, Ned Snell and
Jean-Luc Moncet.

^{*}University of Wisconsin

Prepared for:
Boeing Satellite Systems
919 Imperial Avenue
El Segundo, CA 90245

AER Document P757-TR-EI-ATBD-PRECIP-20010315

This page intentionally left blank.

REVISION HISTORY

Version	Release Date	POC	Comments
1.0	April 2000	G.W. Petty	Initial partial draft / no figures or equations
1.1	10 July 2000	G.W. Petty	Added RTE and retrieval descriptions
1.1b	8 January 2001	G.W Petty	Returned to AER for material on land retrievals
1.1c	10 January 2001	AER	Added results for retrievals over land. Returned to G.W. Petty for further updates.
1.1d	21 Feb 2001	G.W. Petty	Added material on simulated retrievals over water; added reference list, numerous corrections.
1.2	22 Feb 2001; 15 March 2001	AER	Final revisions and clean-up before delivery; Reformat title pages and footers

RELATED CMIS DOCUMENTATION

Government Documents

Title	Version	Authorship	Date
CMIS SRD for NPOESS Spacecraft and Sensors	3.0	Associate Directorate for Acquisition NPOESS IPO	2 March 2001

Boeing Satellite Systems Documents

Title		Covering
ATBD for the CMIS TDR/SDR Algorithms		
ATBD for the CMIS EDRs	Volume 1: Overview	Part 1: Integration Part 2: Spatial Data Processing <ul style="list-style-type: none"> • Footprint Matching and Interpolation • Gridding • Imagery EDR
	Volume 2: Core Physical Inversion Module	
	Volume 3: Water Vapor EDRs	Atmospheric Vertical Moisture Profile EDR Precipitable Water EDR
	Volume 4: Atmospheric Vertical Temperature Profile EDR	
	Volume 5: Precipitation Type and Rate EDR	
	Volume 6: Pressure Profile EDR	
	Volume 7: Cloud EDRs	Part 1: Cloud Ice Water Path EDR
		Part 2: Cloud Liquid Water EDR
		Part 3: Cloud Base Height EDR
	Volume 8: Total Water Content EDR	
	Volume 9: Soil Moisture EDR	
	Volume 10: Snow Cover/Depth EDR	
	Volume 11: Vegetation/Surface Type EDR	
	Volume 12: Ice EDRs	Sea Ice Age and Sea Ice Edge Motion EDR Fresh Water Ice EDR
	Volume 13: Surface Temperature EDRs	Land Surface Temperature EDR Ice Surface Temperature EDR
	Volume 14: Ocean EDR Algorithm Suite	Sea Surface Temperature EDR Sea Surface Wind Speed/Direction EDR Surface Wind Stress EDR
	Volume 15: Test and Validation	All EDRs

Bold = this document

TABLE OF CONTENTS

RELATED CMIS DOCUMENTATION	4
LIST OF TABLES	8
LIST OF FIGURES	9
1. Introduction.....	13
1.1. Purpose.....	13
1.2. Scope	13
2. Overview and Background Information.....	14
2.1. Objectives of the Precipitation Rate and Type EDR retrieval	14
2.2. Summary of EDR requirements	14
2.2.1. Remarks concerning EDR requirements	14
2.3. Historical and background perspective of proposed algorithm.....	16
2.3.1. Emission-, attenuation- and scattering-based retrievals	16
2.3.2. A polarization-based multifrequency algorithm for ocean precipitation	18
2.3.3. Precipitation estimation over land	21
2.3.4. Inversion methods using physically detailed cloud/radiative transfer models	25
2.4. Instrument Characteristics.....	28
2.4.1. Primary CMIS Channels	28
2.4.2. CMIS Resolution and Sampling Density	29
2.4.3. CMIS Surface Scan Incidence Angle	30
2.4.4. Sensor NEDT	31
2.5. Supplemental Data Required.....	31
2.5.1. Static data	31
2.5.2. CMIS-derived data	31
2.5.3. Cross-Sensor data	32
3. Algorithm Description	33
3.1. Summary of derived requirements on the Precipitation Module.	33
3.2. Overview of Retrieval Strategy.....	33
3.2.1. Ocean algorithm	33
3.2.2. Land algorithm	36
3.2.3. Precipitation Type (Land and Ocean).....	38
3.3. The Forward Radiative Transfer Problem.....	39
3.3.1. Macroscopic cloud structure	43
3.3.2. Microphysical properties	45

3.3.3. Microwave optical properties	47
3.3.4. Radiative transfer simplifications	59
3.3.5. Forward Model Used For Rain-Rate Studies Over Land	62
3.4. Mathematical Description of Algorithm	64
3.4.1. Ocean algorithm	64
3.4.2. Land algorithm	73
3.4.3. Precipitation Type (Land and Ocean).....	75
3.5. Comments on the Uniqueness of the Solution	75
3.6. Algorithm Performance.....	77
3.6.1. Algorithm Performance Over Ocean.....	78
3.6.2. Algorithm Performance Over Land.....	85
3.6.3. Limiting Conditions	95
3.7. Variance/Uncertainty Estimates.....	99
3.8. Sensitivity Studies	99
4. Algorithm Calibration and Validation Requirements.....	100
4.1. Pre-launch.....	100
4.2. Post-launch	100
4.3. Special considerations for Cal/Val.....	100
4.3.1. Measurement hardware	100
4.3.2. Field measurements or sensors	100
4.3.3. Sources of truth data.....	100
5. Algorithm Processing Outline.....	101
5.1. Processing Flow for the specific algorithm.....	101
5.2. Input Data; algorithm output(s).....	101
5.3. Dependencies and Processing Flow	101
5.4. CMIS data processing flow	101
5.5. Ancillary databases	101
5.6. Processing time benchmark data	101
6. Practical Considerations.....	102
6.1. Numerical Computation Considerations	102
6.2. Programming/Procedure Considerations.....	102
6.3. Computer hardware or software requirements	102
6.4. Quality Control and Diagnostics	102
6.5. Exception and Error Handling.....	102

6.6. Special database considerations	102
6.7. Special operator training requirements	102
6.8. Archival requirements	102
7. Constraints, Limitations, Assumptions.....	103
8. References	103
8.1. Government Documents and Communications.....	103
8.2. HSC Documents.....	103
8.3. Technical Literature	103
LIST OF ACRONYMS.....	109

LIST OF TABLES

Table 1: Precipitation EDR Requirements	14
Table 2: Primary CMIS Channels - Ocean Precipitation Rate.....	28
Table 3: Primary CMIS Channels - Land Precipitation Rate.....	29
Table 4: Composite Field of View sizes at which CMIS channels.....	30
Table 5: Rain cloud parameters used to show radiometric ambiguity.	76
Table 6: Atmospheric parameters used for generating the geophysical dataset (ice included). The statistics are shown for the cloud liquid water (CLW), the rain water path (RWP), the surface rainfall rate (RR) and the ice water path (IWP) and the liquid water path (LWP).	88
Table 7: (a) Precision, (b) accuracy, and (c) correlation results of the neural-net retrieval of the RR alone.....	90
Table 8: (a) Precision, (b) accuracy, and (c) correlation results of the neural-net retrieval of the RR along with IWP and LWP.	91

LIST OF FIGURES

Figure 1: Utilization of brightness temperature and polarization information over water. Left panel: brightness temperature as a function of nominal rain rate for selected frequencies, vertical and horizontal polarization. Middle panel: the normalized polarization P . Right panel: The scattering index S	19
Figure 2: Model brightness temperatures versus nominal rain rate over land. Horizontal dashed lines indicate approximate natural range of variability of background brightness temperature.....	23
Figure 3: Flow diagram illustrating the overall logic of the ocean rainfall retrieval.	36
Figure 4: Flow diagram illustrating the overall logic of the precipitation type classification.	39
Figure 5: An example of a Backwards Monte Carlo simulation of a high-resolution satellite image at 37 GHz for a mesoscale convective system (MCS) viewed at 53° incidence. Each panel represents one model domain with dimensions 50 km x 50 km. Right: Horizontally polarized brightness temperature. Bottom: Vertically polarized brightness temperature. Left: Normalized polarization P . Top: Polarization-corrected scattering index S . 42	42
Figure 6: Rain effect on simulated brightness temperatures for both vertical (dashed lines) and horizontal (solid lines) polarizations. Rain has been added in the lowest two layers of the profile. The surface wind speed is 7 m/s. The sea surface emissivity model is based on Wilheit. Results are shown for cases without rain, cases with rain rate of 2 mm/hr, 10 mm/hr and 20 mm/hr. All simulations are done using the U.S. standard atmosphere.64	64
Figure 7: Example of the relationship between rain rate retrieval cells (contiguous parallelograms) and sensor FOVs (ellipses) for a single AMSR scan. a) 18.7 GHz b) 89.0 GHz.	69
Figure 8: Organization of neural-net algorithm aiming at the simultaneous retrieval of the rain rate, total liquid water path (LWP) and the ice water path (IWP).	74
Figure 9: Vertical distributions of horizontally uniform precipitation. The surface rain rates are (a) 8.0 mm/hour and (b) 6.1 mm/hour.....	77
Figure 10: Satellite-observed microwave spectrum for the two precipitation cases described in Table 5 and shown in Figure 9.	77
Figure 11: Selected validation statistics for SSM/I algorithms submitted to the 3d Algorithm Intercomparison Project (AIP-3). The Petty (1995b) algorithm is identified by “PE1”. The	

LIST OF FIGURES

mean ratio of satellite to radar rainfall is of questionable absolute value owing to concerns about the absolute calibration of the radar rain rates.	79
Figure 12: Selected validation statistics taken from PIP-3. The Petty (1994b) algorithm is identified as “pur”.	80
Figure 13: Simulated CMIS brightness temperature swath data from one time step of the MM5 model run. Only the middle of the swath is shown here. Note the absence of strong scattering at 89 GHz (right panel) despite the presence of large surface precipitation rates at some locations in the model domain. The lack of an apparent scattering signature appears to be due to very large amounts of cloud liquid water produced by the model at locations where graupel is also produced.	83
Figure 14: Comparison of “actual” (left) and “retrieved” (right) surface rain rate fields, after averaging of both to 15 km resolution. Note logarithmic color scale spanning three orders of magnitude. Rain rates below approximately 0.3 mm/hr were below the sensitivity threshold of the CMIS retrieval algorithm. Also, instances of very high surface precipitation rate in the model-generated rain rate field are highly localized and could not be resolved by the retrieval algorithm.....	84
Figure 15: Results of simulated retrievals. Left panel: Distribution of “actual” rain rates in MM5 simulation, at 15 km resolution. Rain rates in excess of 5 mm/hr were rare and highly localized. Right panel: Retrieved vs. “actual” rain rates. Solid line represents the average of the retrievals for each 1 mm/hr “actual” rain rate bin. Dashed lines indicated the standard deviation above and below the mean. Note that retrieval accuracy and precision are very good below 5 mm/hr. At localized higher rain rates, a systematic underestimate occurs because of “smearing” of the retrieved rain rate over a larger area than that occupied by the actual rain cells.....	85
Figure 16: Schematic diagram showing vertical distribution of cloud constituents used for the generation of hydrometeor profiles (Kummerow and Giglio, 1994). The rain-rate (R) is selected randomly within a predetermined range using a random number (Ψ) between 0 and 1. For the case shown here, the RR falls in the range from 0-20.	87
Figure 17: Detailed stratified performance estimates of (a) precision, (b) accuracy, and (c) the scatterplot for the RR retrieval with the simultaneous retrieval of LWP and IWP. This corresponds to the case in Table 8 using the Tbs only for all CMIS channels. The solid horizontal lines correspond to the threshold requirements.....	92
Figure 18: Detailed stratified performance estimates of (a) precision, (b) accuracy, and (c) the scatterplot for the RR retrieval with the simultaneous retrieval of LWP and IWP. This	

LIST OF FIGURES

figure is the same as the previous figure except that performance is only calculated for low values of rain-rate.....	93
Figure 19: Detailed performance estimates of (a) precision, (b) accuracy, and (c) scatterplot for the RR retrieval with the simultaneous retrieval of LWP and IWP. This corresponds to the emissivity of “ice”. The solid horizontal lines correspond to the threshold requirements.	94
Figure 20: Detailed performance estimates of (a) precision, (b) accuracy, and (c) scatterplot for the RR retrieval with the simultaneous retrieval of LWP and IWP. This corresponds to the emissivity of “snow”.....	95
Figure 21: Precipitation geometry effects. The dashed lines mark the cloud extent; the plain solid curve marks the polarization index with infinitesimal resolution; the curve with dots marks the polarization index convolved with the cross-scan antenna pattern, where the dots are at 12.5 km intervals marking the sample spacing.	98

LIST OF FIGURES

This page intentionally left blank.

1. Introduction

1.1. Purpose

This Algorithm Theoretical Basis Document (ATBD) describes the theoretical background, implementation, and validation plan for the Precipitation Rate and Type algorithm (hereafter "Precipitation Module") for the Conical-scanning Microwave Imager/Sounder (CMIS). Atmospheric and Environmental Research, Inc. (AER) has developed this algorithm in support of the National Polar-orbiting Operational Environmental Satellite System (NPOESS). The Precipitation Module consists of two independent sub-modules for the retrieval of precipitation over ocean and non-ocean (i.e., land or sea ice) regions, respectively.

The retrieval products yielded by this algorithm include (1) estimates of near-instantaneous surface precipitation intensity at the time of the satellite overpass, and (2) characterization of the surface precipitation as "liquid", "frozen", or "indeterminate".

In addition to describing the theoretical basis for the algorithm design, this ATBD also highlights numerous unresolved theoretical and practical issues that inherently limit the expected global performance of any passive microwave rainfall estimation/classification algorithm.

1.2. Scope

2. Overview and Background Information

2.1. Objectives of the Precipitation Rate and Type EDR retrieval

2.2. Summary of EDR requirements

The required data products are precipitation rate and identification of type as rain or ice. The requirements in the table below apply under both clear and cloudy conditions.

Table 1: Precipitation EDR Requirements

Para. No.	Description	Thresholds	Objectives
C40.3.4-1	a. Horizontal Cell Size	15 km (TBR)	0.1 km
C40.3.4-2	b. Horizontal Reporting Interval	(TBD)	(TBD)
C40.3.4-3	c. Horizontal Coverage	Global	Global
	d. Measurement Range		
C40.3.4-4	1. Precipitation Rate	0 - 50 (TBR) mm/hr	0 - 250 mm/hr
C40.3.4-5	2. Precipitation Type	rain and ice	rain and ice
C40.3.4-6	e. Measurement Accuracy, Precip. Rate	2 mm/hr	2 mm/hr
C40.3.4-7	f. Measurement Precision, Precip. Rate	1 mm/hr	1 mm/hr
C40.3.4-8	g. Correct Typing Probability, Precip. Type	(TBD) %	(TBD) %
C40.3.4-9	h. Mapping Uncertainty	3 km	0.1 km
C40.3.4-10	i. Swath Width	1700 km (TBR)	3000 km (TBR)

2.2.1. Remarks concerning EDR requirements

Precipitation rate refers to the rate of accumulation of water from discrete falling hydrometeors passing through (or impinging upon) a horizontal surface. As such, precipitation rate is inherently a stochastic variable that cannot be defined unambiguously in the limit as the time averaging interval goes to zero. Consequently, the assumption of a finite time averaging window, either explicit or implicit, cannot be avoided. In the absence of specific requirements, “true” precipitation rates (for the purpose of defining retrieval accuracy and precision) are taken in this ATBD to mean actual surface precipitation rates averaged over the horizontal reporting cell and over a time interval of 10 minutes (TBR), commencing at the time of the satellite overpass. This time interval allows for the fact that microwave imagers are most directly sensitive to vertically integrated precipitation amounts in the lower troposphere, and that 10 minutes is adequate for the majority of the falling hydrometeors present in the atmospheric column at the time of the overpass to reach the surface.

As required for this EDR, precision and accuracy are evaluated for discrete bins of true precipitation rate, where the bin size is small (e.g., 1 mm/hr) compared to the measurement

range. The formal requirements for this EDR are interpreted as applying to global data within a given intensity bin, without regard for surface type, geographic location, or season. However, it must be emphasized that the difficulty of retrieving precipitation rate and type is inherently dependent on these three factors (see section 3.3). An algorithm that meets threshold requirements globally may in fact consistently perform poorly in certain restricted regions. Issues pertaining to global performance and validation will be discussed further in Section 3.5 and Section 4.

As indicated in Table 1, the Precipitation EDR requirement for measurement accuracy is 2 mm/hr, independent of precipitation rate. Note that this maximum allowable systematic bias is approximately 17 times the global annual average precipitation rate, implying that precipitation estimates could meet the accuracy requirement within the lightest intensity bins (e.g., 0-1 mm/hr) and still be unusable for climatological purpose.

The EDR requirement is for precipitation type to be determined as either "rain" or "ice". Typing accuracy is given in terms of these discrete choices. In reality, mixtures of snow and rain are not uncommon. There is therefore an ambiguity in the determination of "correct typing probability." For the purposes of evaluating performance, AER proposes to treat mixtures of snow and rain as "ice" and to reserve the designation of "rain" for purely liquid precipitation. In addition, there will be cases in which a clear determination cannot be made, in which case the designation of either "ice" or "rain" could be misleading. For this reason, the algorithm will sometimes return a third classification, "indeterminate."

The EDR requirements for precipitation typing are stated in terms of "correct typing probability" (%). Note however that, globally, snowfall constitutes a relatively small fraction of all precipitation events (weighted by area and time). Therefore an algorithm can exhibit a comparatively high "correct typing probability" *globally* even if it erroneously classifies all precipitation as "rain." A preferred measure of performance would be "correct typing skill", as quantified by an accepted statistical metric for discrete classification schemes, such as the Heidke Skill Score. In the case of unequal prior probabilities, a scheme that yields the best skill will not necessarily yield the best "correct typing probability." In the development of the precipitation type module, AER seeks to maximize classification *skill* while still meeting the threshold "correct typing probability."

2.3. Historical and background perspective of proposed algorithm

Algorithms for retrieving rainfall rates from microwave imagery have evolved and multiplied enormously since their first appearance in 1977. In order to justify the basic approach pursued by AER for CMIS it is useful to trace the heritage of the proposed methods and to compare and contrast these with the known alternatives.

2.3.1. Emission-, attenuation- and scattering-based retrievals

The first quantitative satellite microwave rainfall retrieval method was published by Wilheit et al. (1977). This algorithm estimated rainfall rate by way of increased thermal emission of the atmosphere viewed against the low-emissivity ocean background at 19.35 GHz. Algorithms of this type are commonly referred to as "emission-based" algorithms and are generally applicable to microwave frequencies at and below 37 GHz. Emission-based algorithms are not practical over land or sea ice, because the surface emissivity is high and variable; therefore, changes in atmospheric optical depth do not lead to readily discernible changes in microwave radiance. An additional limitation of emission-based algorithms is that microwave radiances tend to saturate once the rain cloud becomes optically thick at higher rain rates. Beyond that point, brightness temperatures may decrease again, leading to an inherent ambiguity in the estimation of precipitation rate from single-channel brightness temperatures.

Spencer (1986) and Spencer et al. (1989) first elucidated the phenomenological basis for "scattering-based" rain rate algorithms. According to this general approach, the presence and comparative intensity of precipitation is inferred via depressions of observed microwave brightness temperatures (especially at frequencies greater than 37 GHz) relative to a brighter background. The source of the depression is volume scattering of microwave radiation by precipitation-size ice particles in the upper portions of clouds. Scattering-based algorithms are less physically direct in their measure of precipitation intensity than emission-based algorithms, because not all rain clouds produce ice phase hydrometeors aloft and, in those that do, the relationship between the concentration of frozen precipitation aloft and surface rain rate is far from unique. However, notable advantages of scattering-based methods include the following: (1) they are useful over high-emissivity surfaces, such as bare or vegetation-covered land, and (2) saturation is not believed to be a serious issue, as increasing rain rates tend to be statistically associated with ever-increasing concentrations and sizes of frozen particles aloft, leading to continued reductions in microwave brightness temperature.

The application of single-channel scattering-based algorithms over water is problematic in that the ocean background is already radiometrically cold. Therefore, these methods tend to suffer from the same ambiguities over water that emission-based methods experience over land. Spencer (1986) proposed an elegant solution to this problem for the case that dual polarization brightness temperatures are available at a single frequency. The proposed method is based on the observation that land and non-precipitating clouds tend to be associated with warm, weakly polarized brightness temperatures whereas the open ocean yields cold, strongly polarized brightness temperatures. By contrast with both background types, precipitating clouds yield relatively cold but weakly polarized brightness temperatures. Spencer therefore proposed a linear combination of the vertical and horizontal channels that is essentially orthogonal to the radiometric signatures of non-precipitating cloud against an ocean background and also insensitive to the contrasting emissivity of land and ocean. These ideas were refined by Spencer et al. (1989) and demonstrated for the 85.5 GHz channels of the SSM/I, which are more strongly sensitive to scattering by ice in ordinary precipitating clouds than the 37 GHz SMMR channels utilized by Spencer (1986).

With the advent of the "polarization-corrected temperature" (PCT) algorithm of Spencer et al. (1989), it became possible to distinguish precipitation against both a land and ocean background using the same basic estimation method. However, this method still had two drawbacks: (1) the technique is sensitive to the inconstant relationship between scattering by ice aloft and surface precipitation rate, and (2) the fixed linear coefficients proposed by Spencer et al. proved inadequate for global retrievals, because the algorithm did not entirely discriminate precipitation changes from regional variations in surface and atmospheric temperature, ocean surface roughness and other sources of cross-talk.

Although modern passive microwave rain rate algorithms have evolved substantially beyond the pioneering methods described above, all are still dependent on the same basic types of radiometric evidence for the presence and intensity of precipitation. In general, emission- or attenuation-based algorithms are regarded as more direct and reliable over open water than scattering-based techniques, but they are essentially useless over land or sea ice. Scattering-based methods function over both land and water but are less physically direct, and therefore less dependable, as indicators of surface precipitation rate. Moreover, scattering-based methods may have difficulty distinguishing the signature of ice particles aloft from that of surface scatterers, such as snowpack or desert sand.

Over water, hybrid methods are possible that combine the best features of both scattering- and attenuation- or emission-based methods. The history and rationale behind one such algorithm, which is the foundation for the ocean component of the Precipitation Module for CMIS, is described in the next subsection.

2.3.2. A polarization-based multifrequency algorithm for ocean precipitation

Petty and Katsaros (1990, 1992) revisited the utilization of polarization information at a single frequency, focusing not on scattering however but rather on an attempt to improve the characteristics of emission-type algorithms over water. They noted that rain rate is a double-valued function of observed single-channel brightness temperature, as utilized in classic emission-based algorithms such as Wilheit et al. (1977), but a single-valued function of the polarization *difference* at the same frequency. This relationship occurs because polarization differences over the ocean arise primarily from the polarization-dependent emissivity of the surface; hence, increases in rain cloud optical depth reduce the observed polarization difference in a monotonic fashion (barring minor polarizing effects of oriented non-spherical ice particles). Furthermore, Petty and Katsaros found from model calculations that the polarization difference, expressed as a fraction of the cloud-free (or open-ocean) value, is a nearly invariant function of the total rain cloud transmittance at the frequency in question. This led them to define a so-called *normalized polarization* P , in which the observed polarization difference is divided by the hypothetical cloud-free polarization difference for the same scene. The cloud-free difference is either estimated from the highest polarization differences observed within a specified radius of the pixel in which rainfall was to be retrieved or else can be computed from a forward model applied to estimated values of environmental parameters, such as surface wind speed and total column water vapor. The latter has become the preferred approach.

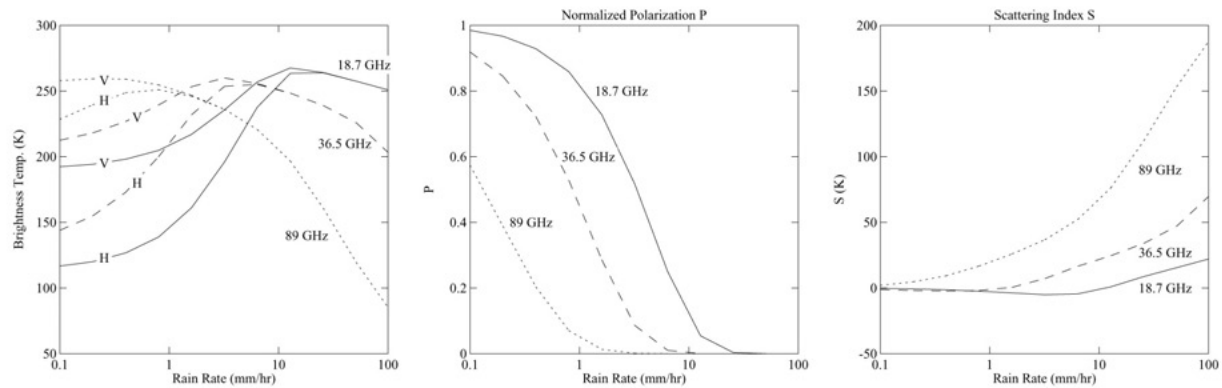


Figure 1: Utilization of brightness temperature and polarization information over water. Left panel: brightness temperature as a function of nominal rain rate for selected frequencies, vertical and horizontal polarization. Middle panel: the normalized polarization P . Right panel: The scattering index S .

Petty (1994a,b) also refined the Spencer et al. (1989) PCT method by defining a linear transformation of the T_B computed in terms of P , a cloud-free vertically polarized brightness temperature T_{BV0} , and a nominal effective cloud radiating temperature T_C . The result is a so-called polarization-corrected brightness temperature depression S , which is approximately zero in the absence of scattering and positive (>10 K) for significant scattering by ice:

$$S \equiv PT_{BV0} + (1 - P)T_C - T_{BV}$$

The cloud-free values of the dual-polarized brightness temperatures may be approximated as functions of column water vapor and surface wind speed, or they may be estimated via a more detailed retrieval of atmospheric properties coupled with a forward model. The idealized behavior of both S and P as a function of rain rate is depicted in Fig. 1. These two parameters effectively decouple the signature of scattering due to ice from that due to attenuation (mostly by liquid water) of the ocean surface signal through the total atmospheric column.

To summarize, the principal improvements claimed for a normalized polarization-based (or attenuation-based) method, as compared with a single-polarization emission-based method, include: (1) elimination of the double-valuedness of the relationship between the observable and surface precipitation rate; (2) elimination of water vapor and surface wind speed as important sources of cross-talk; and (3) the ability to express the observable P as a simple (if approximate) analytic function of a well-defined optical property of the rain cloud, namely, the total optical depth or transmittance associated with condensed water in the column.

Other problems common to both emission- and attenuation-based methods remained: the relationship between microwave observable and surface rain rate, even if monotonic in the case of the normalized polarization, is non-linear. When rainfall not uniformly distributed throughout the 20-50 km field-of-view (FOV) of the SSM/I sensor, the rain rate estimated from footprint-averaged radiances is generally a gross underestimate of the actual footprint-averaged rain rate. Eliminating the so-called footprint-filling (or beam-filling) bias requires an independent estimate of the nature and degree of the inhomogeneity. Other researchers have traditionally applied a constant effective mean footprint-filling correction, based on the statistical properties of rainfall observed by radar in regional field campaigns such as the GARP Atlantic Tropical Experiment (GATE). Unfortunately, there is little reason to expect such a fixed correction to be valid everywhere, owing to widely varying physical and statistical properties of ocean rainfall around the globe (Petty 1995a; Petty 1999).

An additional complicating factor in emission- and attenuation-based algorithms is the tradeoff between spatial resolution, dynamic range, and sensitivity as one varies the observing frequency. Lower microwave frequencies (e.g., 10-20 GHz) have the largest dynamic range in their response to rain rate, saturating at rain rates as high as 10-20 mm/hr. These frequencies are therefore also most nearly linear in their response to variations in smaller rain rates, thus potentially mitigating the beamfilling bias problem. On the other hand, the signal-to-noise ratio with respect to light rainfall is poorer at long wavelengths; also the spatial resolution is also worse in proportion to wavelength. At higher frequencies (e.g., 20-50 GHz), sensitivity to light rain is optimized and spatial resolution is improved, but saturation occurs early (< 3 mm/hr). At yet higher frequencies (e.g., 80-90 GHz) even the lightest rainfall quickly saturates the response of the channel, and variations in brightness temperature and/or polarization are increasingly dominated by the effects of ice particles aloft, limiting the usefulness of these frequencies in an attenuation mode, except to delineate the boundaries of probable rainfall.

Petty (1994a,b) proposed to exploit the complementary multi-frequency information content of normalized polarizations observed by the SSM/I: lower frequencies provide information on relatively heavy rainfall rates averaged over somewhat larger FOVs; high frequency channels yield accurate spatial delineation of rainfall and sensitivity to the lightest rain rates. Petty thus developed a unique spatial inversion algorithm in which a relatively densely sampled array of rainfall rates is retrieved which is simultaneously consistent (to within specified tolerances) with

normalized polarization images at 19.35, 37 and 85.5 GHz. Not only does this method attempt to maximize the extraction of rain rate information from all channels, with due allowance for their respective sensitivities and spatial resolutions, it also mitigates the beam-filling problem by finding a high-resolution rain rate field which is radiometrically consistent with over-sampled low-resolution imagery.

The above method by itself still cannot yield information about rain rates in excess of the saturation value for the lowest frequency channels (approximately 10 mm/hr at 19.35 GHz). Therefore, Petty initialized the first-guess rain rate field using scattering information derived from the 85.5 GHz channels, which are less direct as estimators of precipitation intensity but also less prone to saturation. High values of the first-guess rain rate were left in place during the subsequent physical inversion unless the objective of consistency with observed normalized polarizations *required* them to be reduced.

By the above combination of methods, Petty (1994a,b) thus sought to maximize the utilization of multi-channel attenuation- and scattering-based information and to do so in a physically self-consistent way. In so doing, it was recognized that theoretical models for the relationship between polarization and rain rate were both approximate and inherently uncertain; thus the criteria for consistency were deliberately kept loose in order to avoid over-fitting of the retrieved rain rate field to the microwave observations.

2.3.3. Precipitation estimation over land

There is inherently less unambiguous information concerning precipitation rates in microwave radiances over land. There are several reasons for this:

- Land surface emissivities are generally high and only weakly polarized. Therefore variations in atmospheric optical depth (without scattering) yield only small changes in microwave brightness temperature or polarization. Moreover, the sign of brightness temperature changes may be either positive or negative, depending on the precise surface emissivity and on the vertical absorption and temperature structure of the atmosphere.
- Land surface emissivities may be highly variable in both time and space, due to variations in vegetation cover, soil structure, surface moisture, snow cover and other variables. Thus, any

OVERVIEW AND BACKGROUND INFORMATION

precipitation signature in the microwave radiances must be larger than this background noise source in order to be reliably observed. Furthermore, the potential for local biases exists if an algorithm does not compensate for these variations.

- As a consequence of the above, emission-based and attenuation-based retrieval techniques, and the direct utilization of microwave frequencies much below 37 GHz, is effectively ruled out over land.
- Scattering signatures of ice at 37 GHz and higher frequencies are more readily observed against a land background. However they are inherently indirect as measures of surface precipitation intensity. In particular, surface rainfall from certain clouds lacking a significant ice phase may not necessarily be detectable by any passive microwave method over land.
- Scattering signatures of ice particles aloft may be readily confused with similar signatures associated with snow cover and sandy soil, unless the sensor channel is "surface blind" owing to its location in a water vapor or oxygen absorption band. In the latter case, the channel also loses sensitivity to the presence of precipitation in the lower troposphere, so shallow rain clouds may escape detection.

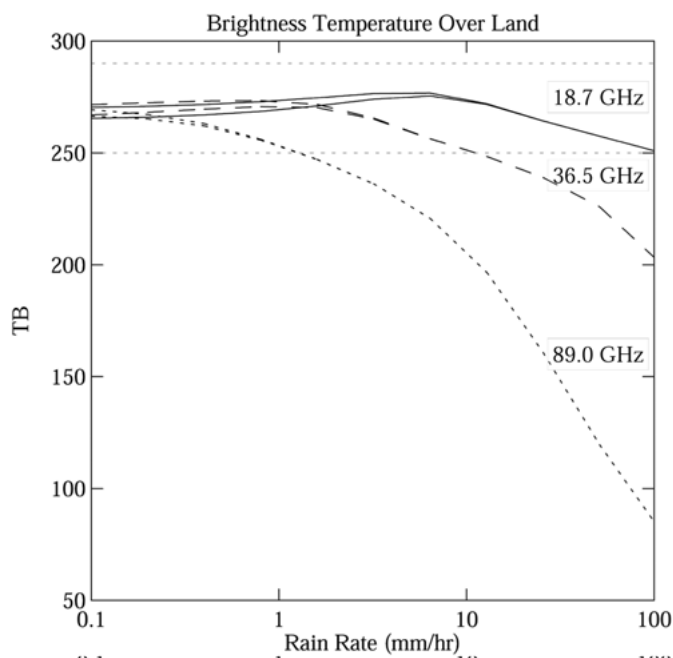


Figure 2: Model brightness temperatures versus nominal rain rate over land. Horizontal dashed lines indicate approximate natural range of variability of background brightness temperature.

In view of the above difficulties, most modern algorithms for over-land precipitation retrievals using window frequencies tend to have the following features in common:

- Most of the algorithm logic is devoted to the problem of initially classifying pixels as raining or non-raining in the presence of variable land surface emission (the so-called screening problem).
- The actual extraction of rain rate information is usually based on simple empirical or semi-empirical relationships between brightness temperature depressions at a single frequency (e.g. 85.5 GHz) and surface precipitation rate. In algorithms that depend on physical models, results are sensitive to the details of the parameterization of cold cloud microphysical processes in the model and to the manner in which ice water content is modeled for radiative transfer purposes (e.g., assumed sizes and shapes).
- Most current-generation algorithms do not attempt precipitation retrievals over problem surface types, such as snow cover or sea ice.

The most successful over-land precipitation retrieval schemes to date, as determined via organized intercomparisons of competing algorithms developed for the SSM/I (e.g., PIP-3; Adler et al. 2001), appear to be those which deal most effectively with variability in the land surface background. The primary strategy for over-land precipitation retrieval for CMIS is thus similar to that of Conner and Petty (1998), but with theoretical and empirical refinements based on recent observational data and improved models of microwave radiative transfer in rain clouds. Improved performance over problem surface types will also be achieved by exploiting selected sounding channels on CMIS, as discussed later in this document.

According to the method of Conner and Petty, maps of mean multi-channel "background" (or "baseline") brightness temperatures are constructed at comparatively high spatial resolution but low temporal resolution (e.g., monthly). This may be accomplished either by way of radiative transfer models coupled with detailed, dynamically updated maps of surface emissivity, or by

reference to prior actual satellite overpasses sampling precipitation-free locations. The baseline maps are subtracted from the current satellite overpass to yield multi-channel brightness temperature anomalies. These anomalies are traceable to local environmental variations on time scales shorter than the original averaging period used to create the baseline maps. Examples of variables contributing to long-term and short-term local changes in brightness temperature include seasonal changes in vegetation cover, and short-term variations in surface wetness, snow cover, surface temperature, and precipitation in progress. Variations in vegetation cover are assumed to occur slowly enough to be accounted for in the season-dependent baseline brightness temperature maps. Surface wetness and surface temperature have characteristic signatures that allow the influence of these variables to be identified and subtracted from the multi-channel anomaly map derived from a single overpass. The residual anomaly is assumed to be associated with precipitation or surface snow cover. Empirical screening criteria (e.g., Grody 1991) are utilized in an attempt to distinguish surface snow cover from precipitation in progress. In current versions of the algorithm, rain rate retrievals are not attempted where surface snow cover is detected. Otherwise, precipitation intensity is estimated from empirical relationships applied to the residual brightness temperature anomaly.

Although the details vary, the Conner/Petty algorithm is fairly characteristic of most current-generation over-land rain rate estimation algorithms, in that instantaneous brightness temperature anomalies in one or more channels (but invariably including the 85.5 GHz channels) are determined relative to a baseline brightness temperature field which may be derived either from prior observations over a period of time or else from an empirical formula applied to the sensor's lower frequency channels (e.g., the *SI* scattering index of Grody 1991). The local rain rate is then inferred as a simple linear or non-linear function of the anomaly.

Experience with global validation of passive microwave rainfall estimates to date (e.g., PIP-3) reveals that current-generation algorithms, while yielding useful information about precipitation over most snow- and ice-free land areas, still exhibit marginal precision and accuracy even with respect to monthly gauge totals. No recognized intercomparison exercise to date has shed any light on the global performance of current algorithms stratified by rain intensity over the range 0-50 mm/hr, but all available evidence suggests that substantial advances beyond the current state-of-the-art outlined above would be needed in order to meet the CMIS EDR threshold precision and accuracy requirements over land, especially at high rain rates. There are only a few obvious

avenues for achieving such improvement, and the likely net impact of some of these on global performance remains a matter of conjecture.

Examples of such opportunities, in order of decreasing likelihood of major impact, include:

- Improved mapping and dynamic updating of background surface emissivity. Advances in this area would substantially improve the likelihood of detecting light precipitation over the widest variety of surface types.
- Development of estimation techniques that are less sensitive to surface properties, especially using "surface blind" sounding channels. The general validity of this approach is already being demonstrated using selected channels of the AMSU-B sensor.
- Improved models of the relationship between scattering by ice aloft and surface precipitation rate, and improved characterization of regional and seasonal variability in these relationships.
- Development of improved spectral criteria for distinguishing scattering due to instantaneous precipitation from similar signatures due to surface snow cover and other problem surface types

2.3.4. Inversion methods using physically detailed cloud/radiative transfer models

There is another class of algorithms, not yet discussed, that is potentially applicable to both ocean and land precipitation retrievals. These methods attempt to find detailed vertical profiles of hydrometeors and other environmental variables that are radiometrically consistent with the observed multi-channel brightness temperatures. One such algorithm (Smith et al. 1994) iteratively adjusts the hydrometeor profiles until forward-calculated radiances using a radiative transfer model agree with the observations. Another well-known approach (Kummerow et al. 1996), currently utilized for operational rainfall and latent heating profile retrievals from the Tropical Rainfall Measuring Mission (TRMM) Microwave Imager (TMI), performs a library look-up to identify all cloud model-generated profiles whose pre-calculated brightness temperature vector is "close" to the observation vector. The retrieved profile and surface rain rate are then computed as an average of the selected profiles, weighted by the closeness of the match to the observations.

Attractive properties of these so-called physical model-based retrieval methods include the following:

- At least in theory, they should allow maximum utilization of the physical information content of the multi-channel microwave radiances as well as minimizing errors associated with the simplifying physical assumptions characteristic of other types of retrieval algorithms.
- In theory, a cloud profile database utilized in a Bayesian retrieval scheme can be tailored to a wide range of precipitation types and cloud geometries, potentially incorporating regional and seasonal variations in the *a priori* distribution of candidate profiles.
- Most importantly, physical cloud model/radiative transfer model-based inversions can potentially yield estimates of associated environmental parameters (e.g., latent heating profiles) not directly observable by satellite.

The above theoretical advantages are offset by certain practical disadvantages:

- They are computationally very expensive to run if real-time forward radiative transfer calculations are required. This problem is much more severe for rainfall retrievals than for other types of profile retrievals, because of the necessity of including multiple scattering in the forward radiative transfer equation.
- Forward radiative transfer calculations are inherently sensitive to microphysical and radiative transfer assumptions made (e.g., the calculation of the scattering properties of snowflakes based on the idealized model of solid ice spheres). The multi-channel signatures that distinguish one candidate cloud profile from another can be subtle, and attempting to detect and exploit these small differences can greatly amplify the influence of errors in the forward cloud/radiative transfer model.
- Current knowledge of global variations in rain cloud properties and their regional and seasonal dependence is insufficient for the purpose of generating credible *a priori* distributions of cloud structures and accompanying multi-channel radiances. Dynamic cloud

model simulations can theoretically provide realistic distributions of cloud properties in different environments, but it has been found that different cloud models and microphysical parameterizations often yield vastly different results, especially as regards the ice phase hydrometeors responsible for the microwave scattering signature. Indeed, some models yield results that are generally irreconcilable with actual microwave observations of rain clouds.

- Moreover, the effective number of independent, radiometrically, geometrically and/or thermodynamically significant environmental variables in a realistic rain cloud structure is large. If this number of degrees of freedom is designated N , and A is a number greater than, say, 3, then on the order of A^N distinct profiles and cloud and viewing geometries are needed to adequately populate the a priori solution space. For N as small as 10, as many as 60,000 or more distinct cases must be provided, and, as noted previously, it must be ensured that their distribution in N -space is reasonably realistic for the region and season in question in order for Bayesian-style retrievals to yield unbiased results.
- Despite the greater physical sophistication, these algorithms are still subject to the same fundamental limitations as the simpler "emission-", "attenuation-", and "scattering-based" algorithms described earlier. That is, the use of physically detailed cloud/radiative transfer models does not substantially improve the utility of lower frequency channels over a variable and strongly emitting land background, nor does it directly mitigate the beam-filling problem (although a solution data base could theoretically include variable distributions of rainfall within a finite field-of-view).

In addition to the above practical difficulties of developing a globally applicable physical model-based precipitation algorithm that demonstrably meets EDR requirements globally, we note that algorithms in this category have not been shown to consistently outperform simpler algorithms (e.g., that of Petty 1994) in recent organized algorithm intercomparisons, despite the former's substantially greater investment in development and real-time computational effort. Consequently, AER has elected to pursue a middle road between simple empirical or semi-empirical algorithms on the one hand and highly detailed model-based inversion algorithms on the other. Instead, we seek to maximize the extraction of physical and spatial information from CMIS radiances while at the same time minimizing exposure to errors due to as-yet-uncertain statistical, microphysical and radiative transfer properties of global rain clouds.

2.4. Instrument Characteristics

2.4.1. Primary CMIS Channels

2.4.1.1 Ocean Retrievals

The primary source of direct precipitation information over water is CMIS dual-polarization window channels in the range 6.8 through 89 GHz (Table 2).

Table 2: Primary CMIS Channels - Ocean Precipitation Rate

Frequency (GHz)	Polarization
6.8	V+H
10.65	V+H
18.7	V+H
23.8	V+H
36.5	V+H
89.0	V+H

The possible utility of additional channels near 50, 166 and 183 GHz is the subject of ongoing study.

2.4.1.2 Land Retrievals

Retrievals of precipitation rate over land will rely on selected window and sounding channels at and above 18.7 GHz. For window channels, dual-polarization information is required. Sounding channels whose weighting functions peak too high in the atmosphere to be sensitive to most rain clouds are generally excluded. A complete list of candidate channels is given in Table 3. (See [EN #13](#) response.) Unlike the case over ocean, over-land retrievals will be undertaken using all channels averaged to a common resolution of 15 km, corresponding to the size of the reporting cell for this EDR.

Table 3: Primary CMIS Channels - Land Precipitation Rate

Frequency (GHz)	Polarization
18.7	V+H
36.5	V+H
50.300	V
51.240	V
53.570	V
89.0	V+H
166.6	V
183.310±0.7125	V
183.310±3.10	V
183.310±7.7	V

It is likely that a smaller subset of these channels will be utilized in the final algorithm, based on model sensitivity studies and experience with data from the current AMSU-A and AMSU-B sensor.

2.4.2. CMIS Resolution and Sampling Density

The over-ocean algorithm seeks to mitigate beam-filling biases by explicitly retrieving sub-FOV-scale rainfall variability. It therefore utilizes data from each channel at the highest available spatial resolution and sampling density.

For consistency with other EDR retrieval modules, the ocean precipitation module will utilize re-mapped brightness temperatures produced by the footprint-matching algorithm that constitutes the front end of the EDR processing chain. After the footprint matching, each channel is available at a set of Composite Field of View (CFOV) sizes. The precipitation algorithm uses each channel at the CFOV size most consistent with the cross-scan size of the original footprint data (Table 4). CFOV sizes significantly larger than the original footprint size are avoided because they induce unnecessary smoothing of precipitation information and CFOV sizes significantly smaller than the original footprint size are avoided because they may have matching-induced sidelobes. For channels which are oversampled in either the along-scan direction or cross-scan direction or both, the re-mapping and resampling procedure will include partial deconvolution of the imagery so as to retain as much information as possible while reducing the sampling density.

Over land, precipitation information comes from higher frequency channels whose native resolution is about equal to the reporting cell size for precipitation. Consequently, all primary channels in Table 4 will be spatially averaged to a common resolution of approximately 15 km prior to calling the over land precipitation module.

Table 4: Composite Field of View sizes at which CMIS channels are used in the Precipitation EDR algorithm.

Frequency (GHz)	CFOV size (km)
6.8	50
10.65	40
18.7	25
36.5	15
50.300	15
51.240	15
53.570	15
89.0	15
166.6	15
183.310±0.7125	15
183.310±3.10	15
183.310±7.7	15

2.4.3. CMIS Surface Scan Incidence Angle

Because of the reliance of the algorithm on polarization information, oblique viewing at near-constant incidence angle is an essential characteristic of the CMIS. Over land, where polarization information is not as important, near-constant incidence angle is nevertheless useful because it alleviates the need to account for limb effects in the sounding channels. It also permits more reliable discrimination against wet soil and standing water. The algorithm allows for differences in incidence angle among the CMIS channels ($< 5^\circ$) small enough that the channels all traverse approximately the same slant path through the atmosphere.

However, non-nadir observations are also more susceptible to 3-D geometric effects in rain clouds, including parallax effects, cloud reflections from the ocean surface, and emission from the sides of convective clouds. These effects are difficult to account for precisely in a precipitation algorithm because they depend on the details of the 2-D and 3-D structure of the rain clouds. To first order, modeling studies suggest that the primary effect of parallax effects on ocean rain rate retrievals is to “smear” the apparent image of the rain cloud by several kilometers

(both toward and away from the sensor) in the cross-scan direction. Another consequence is the displacement of the apparent location of the scattering cloud tops observed at higher frequencies from the true surface location of the rain cloud. Both effects can be mitigated relatively simply by utilizing parallax-corrected antenna gain patterns in the retrieval algorithms.

2.4.4. Sensor NEDT

Rain clouds exhibit large structural and microphysical variations that are difficult to fully account for in forward model calculations or in the retrieval algorithm itself. These variations therefore contribute “geophysical noise” on the order of several K to the rainfall estimation problem. By comparison, sensor noise-equivalent delta-T (NEDT) figures of less than 1 K for the footprint-matched data are believed to have negligible impact on precipitation retrieval performance and are therefore not considered further in this ATBD.

2.5. Supplemental Data Required

In addition to CMIS brightness temperatures, other CMIS-derived and non-CMIS data are required for the Precipitation Module. These include the following:

2.5.1. Static data

Land-sea-ice mask. In order to determine where the ocean and land sub-modules should be applied, CMIS pixels must be pre-classified into one of the following three categories: (1) ocean, (2) land, and (3) sea ice. Pixels in the first class must contain no more than 5% land or sea ice, weighted according to the lowest-resolution antenna gain pattern. The sea ice classification will be determined for a given CMIS overpass by the appropriate algorithm module. The land-ocean classification will be obtained from a static geographic mask having 1/6-degree resolution or better.

2.5.2. CMIS-derived data

Cloud-free brightness temperature: Both the land and ocean precipitation modules require reasonable estimates of the “background” brightness temperatures for all relevant channels. These brightness temperatures would be observed if all hydrometeors (frozen and liquid) were removed from atmospheric column while leaving surface emissivity and temperature and humidity profiles unchanged. At locations outside of moderate or heavy precipitation, these estimates will be available as a direct byproduct of the Core Module. Within moderate or heavy

precipitation, Core Module retrievals may be unreliable. In such cases, cloud-free brightness temperatures must be interpolated into precipitating areas from surrounding locations.

Surface emissivity database. One of the byproducts of the CMIS Core Module is a dynamically updated global map of surface emissivity. This database will merge recent observations of snow and vegetation cover and surface wetness with static maps of mean emissivity for all relevant CMIS channels. The estimates of surface emissivity will be utilized primarily in the land precipitation submodule, in conjunction with the cloud-free brightness temperatures described above.

2.5.3. Cross-Sensor data

The Precipitation Module has no direct requirement for data from non-CMIS sensors. In principle, visible and/or infrared imagery could be used to further constrain precipitation retrievals under some conditions – e.g., localized and/or shallow rain clouds, but the potential performance benefits must be weighed against the additional algorithmic complexity. This remains a topic for further research and development.

3. Algorithm Description

3.1. Summary of derived requirements on the Precipitation Module.

Except to flag the possible occurrence of retrieval errors due to precipitation contamination, other algorithms in the CMIS EDR processing chain do not utilize the precipitation estimates produced by this module. Therefore, there are no derived requirements on the algorithm.

3.2. Overview of Retrieval Strategy

Two distinct retrieval strategies are employed; one for open ocean areas and the other for land and coastal zones, and sea ice. Over open water, observed multi-channel brightness temperature depolarization (relative to a hypothetical cloud-free scene) is used to infer path integrated rain cloud attenuation at each applicable frequency, supplemented by information on precipitating ice content inferred from brightness temperature depressions at higher frequencies. Over other surface types (land, sea ice, etc.), surface precipitation rates must be inferred indirectly from the ice signature alone. The ocean and land sub-modules are discussed separately in this and subsequent sub-sections.

3.2.1. Ocean algorithm

The ocean precipitation algorithm is a non-linear physical inversion scheme that exploits spatial oversampling at lower frequencies to find a high-resolution rain rate field that is simultaneously consistent with radiances from all available imager channels. This algorithm thus directly retrieves sub-pixel rainfall variability (relative to the low-resolution channels), partially alleviating the classic beamfilling ambiguity described by (e.g.) Wilheit (1986).

The algorithm utilizes observed polarization differences, rather than raw brightness temperatures, in the inversion in order to circumvent the non-monotonicity of the brightness temperature-rain rate relationship and to reduce the sensitivity of the retrieval to uncertainties in the vertical structure and microphysical characteristics of the rain cloud. Such uncertainties are particularly important with respect to ice phase microphysics. The polarization differences are normalized by an independently estimated cloud-free polarization difference to yield a *normalized polarization* P at each frequency whose value exhibits the following advantageous characteristics:

- It approximately obeys a simple power-law relationship to the path transmittance due to hydrometeors (in the plane-parallel approximation).
- It is approximately orthogonal to brightness temperature variations associated with volume scattering by ice.
- Its quantitative interpretation is not strongly affected by background variations in column water vapor, temperature, surface wind speed, and other variables.

A second linear transformation of dual-polarization brightness temperatures, S , contains information complementary to that of P . The scattering index S is sensitive primarily to volume scattering and rain cloud effective temperature, yielding significant positive values only in the presence of volume scattering by ice and large raindrops. Because ice concentration aloft is a relatively unreliable proxy for surface precipitation rates, S is relegated to a supplemental role in that it helps constrain the solution when more direct information is unavailable. For example, S may yield the only usable information concerning precipitation rate in cases that either (a) the melting level is at or near the surface, in which case total cloud attenuation may be too weak to be accurately estimated via P ; or (b) intense rainfall is occurring through a deep layer, in which case the more direct attenuation based index P may saturate. Petty (1994a) discusses the definitions and complementary information content of P and S in greater detail.

The final rain rate field is obtained at high resolution by iteratively eliminating inconsistencies between forward calculated polarizations from the first-guess field and observed normalized polarizations for all frequencies utilized in the retrieval. An inconsistency is considered to exist if and only if the observed discrepancy exceeds the assumed uncertainty in the forward calculations. This assumed uncertainty must allow for deviations of actual rain clouds from ideal assumptions incorporated in radiative transfer models. Examples of such deviations include 3-D cloud geometry, oriented non-spherical scatterers, non-standard vertical hydrometeor profiles, and finite uncertainties in estimates of the background polarization difference.

The retrieval may be based on as many or as few dual-polarization channels as are available. The utilization of a greater number of channels increases the opportunity to identify and iteratively remove physical inconsistencies (as defined above) in the first-guess rain rate field. In

general, lower frequency channels (6.8, 10.7, 19.35 GHz) respond more linearly to rainfall rate over a larger range of intensities but do so at the cost of reduced sensitivity to light rainfall and poorer spatial resolution. Higher frequency channels (37, 89 GHz) are more sensitive to light rainfall and can localize rain cloud edges with greater accuracy but suffer from saturation at low rain rates. Thus, all primary channels listed in Table 2 yield complementary information concerning intensity and spatial distribution and a rain rate field is sought which does not conflict with the observations at any frequency.

The manner in which the high-resolution rain rate field is adjusted in response to discrepancies between forward-calculated and observed polarizations from lower-resolution channels is analogous to back-propagation in simulated neural networks. That is, the rain rate adjustment in the j^{th} grid box is weighted according to $\partial P_i / \partial R_j$, where P_i is the forward-calculated normalized polarization for the i^{th} pixel at the frequency in question.

This same framework also readily accommodates non-CMIS (e.g., visible or infrared) information in the algorithm when available, provided only that appropriate objective criteria are developed for classifying a given rain rate estimate as *physically inconsistent* with the data in question. An example of such an inconsistency would be a large non-zero rain rate at a location classified as cloud-free based on visible and/or infrared imagery. The current version of the algorithm, however, does not utilize cross-sensor data.

An important characteristic of the over-ocean retrieval strategy is that less direct (e.g., statistical) information concerning likely surface rain rates is retained where, and only where, it does not conflict with more physically unambiguous evidence. In particular, scattering information from the 89 GHz channels, as embodied by the S index, provides the basis for initializing the first-guess rain rate field. If this first guess rain rate field is subsequently found to be inconsistent with the observed polarization P , then it is modified. In locations of heavy rainfall, where P usually saturates, the first-guess value may be left unmodified if it is not contradicted by the lower-frequency observations.

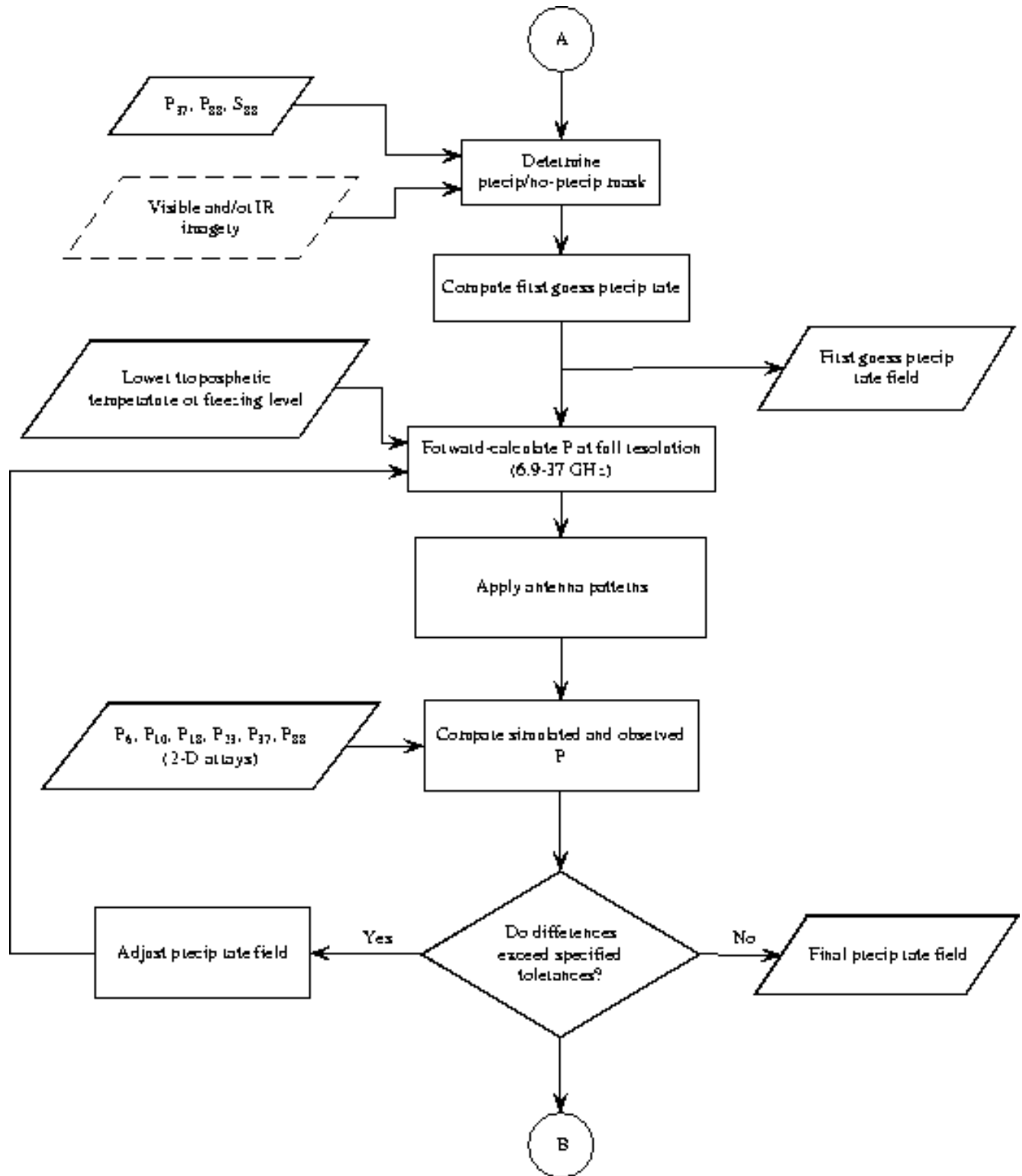


Figure 3: Flow diagram illustrating the overall logic of the ocean rainfall retrieval.

3.2.2. Land algorithm

Because of the large (~0.9) yet highly variable emissivity of land surfaces, rainfall estimation techniques based primarily on passive microwave measures of atmospheric emission and

attenuation are of little utility over land. Rather, it is generally necessary to rely on the detection of reduced brightness temperatures associated with deep, optically thick rain clouds, especially those containing substantial amounts of precipitating ice aloft. The microwave signature of such clouds is most evident at higher microwave frequencies, although there is then also increasing sensitivity to non-precipitating cloud ice. Thus, the central strategy of the retrieval algorithm is to detect brightness temperature anomalies (depressions) relative to the predicted cloud-free background radiances and to assign surface rain intensities based on the spatial and spectral characteristics of those anomalies. The dynamic database of surface emissivity and the estimates of clear-sky radiance provided by the CMIS Core Module therefore play a crucial role in determining the minimum sensitivity of the algorithm to light rainfall and in minimizing regional biases due to variable surface properties.

The detection of precipitation via brightness temperature depressions becomes more problematic when the land surface itself behaves as a volume scatterer of microwave radiation, as is the case when snow or ice cover is present. In fact, no known passive microwave algorithm currently attempts precipitation rate retrievals over ice- or snow-covered regions using window channels. Even a dynamically updated surface emissivity data base may not be sufficiently reliable in regions of snowfall to allow the precipitation signal to be cleanly separated from that of the surface using window channels. In order for the CMIS Precipitation Module to be applicable globally, it is therefore necessary to incorporate sounding channels whose weighting functions peak low enough in the troposphere to be able to detect shallow precipitation but high enough so as to reduce the risk of cross-talk from surface variables such as snow cover. Although empirical algorithms (e.g., simulated neural networks) have been demonstrated over North America using selected channels of the AMSU-A and AMSU-B sensors, the development of unbiased *global* algorithms using CMIS sounder depends on a thorough survey of regional and seasonal precipitation microphysical structure and its implications for microwave radiative transfer. Global microwave data sets available from current sensors, such as SSM/I, TMI, AMSU, and AMSR, will be of great value in this regard.

The retrieval algorithm is currently designed as a neural network-type algorithm applied to multichannel brightness temperature anomalies, where the anomalies are referenced to the computed brightness temperatures in the absence of precipitation. The CMIS Core Module retrievals of atmospheric temperature and humidity, coupled with a dynamic database of surface emissivity, will be the primary source of baseline multichannel brightness temperatures.

3.2.3. Precipitation Type (Land and Ocean)

When the atmospheric freezing level is near the surface, precipitation may reach the surface as snow or may melt shortly before reaching the surface and arrive as rain. From a microwave radiative transfer standpoint, the two cases may be nearly indistinguishable unless the vertical extent of the liquid precipitation is substantial (i.e., more than ~ 0.5 km). In addition, if the freezing level is within a few hundred meters of the surface, it is likely that precipitation will reach the surface as a mixture of snow and rain, which is unlikely to be distinguishable from pure rainfall on the basis of microwave radiometry alone. Yet mixtures of rain and snow are to be classified as ‘frozen’, as discussed in section 3.2.1.

Consequently, the primary strategy for classifying precipitation as ice or liquid depends on the availability of independent information concerning atmospheric temperature structure in the vicinity of precipitation. The CMIS Core Module yields such information in the form of retrieved temperature profiles, which are interpolated into areas of precipitation. The freezing level height (above terrain) Z_L is estimated from these retrievals and if $Z_L < Z_{L,snow}$ then the precipitation is classified as frozen; otherwise it is liquid.

An additional factor that may be considered for classifying precipitation over water is the detectability of a unique spectral signature of liquid precipitation in the column. The potential viability of this approach requires additional study.

ALGORITHM DESCRIPTION

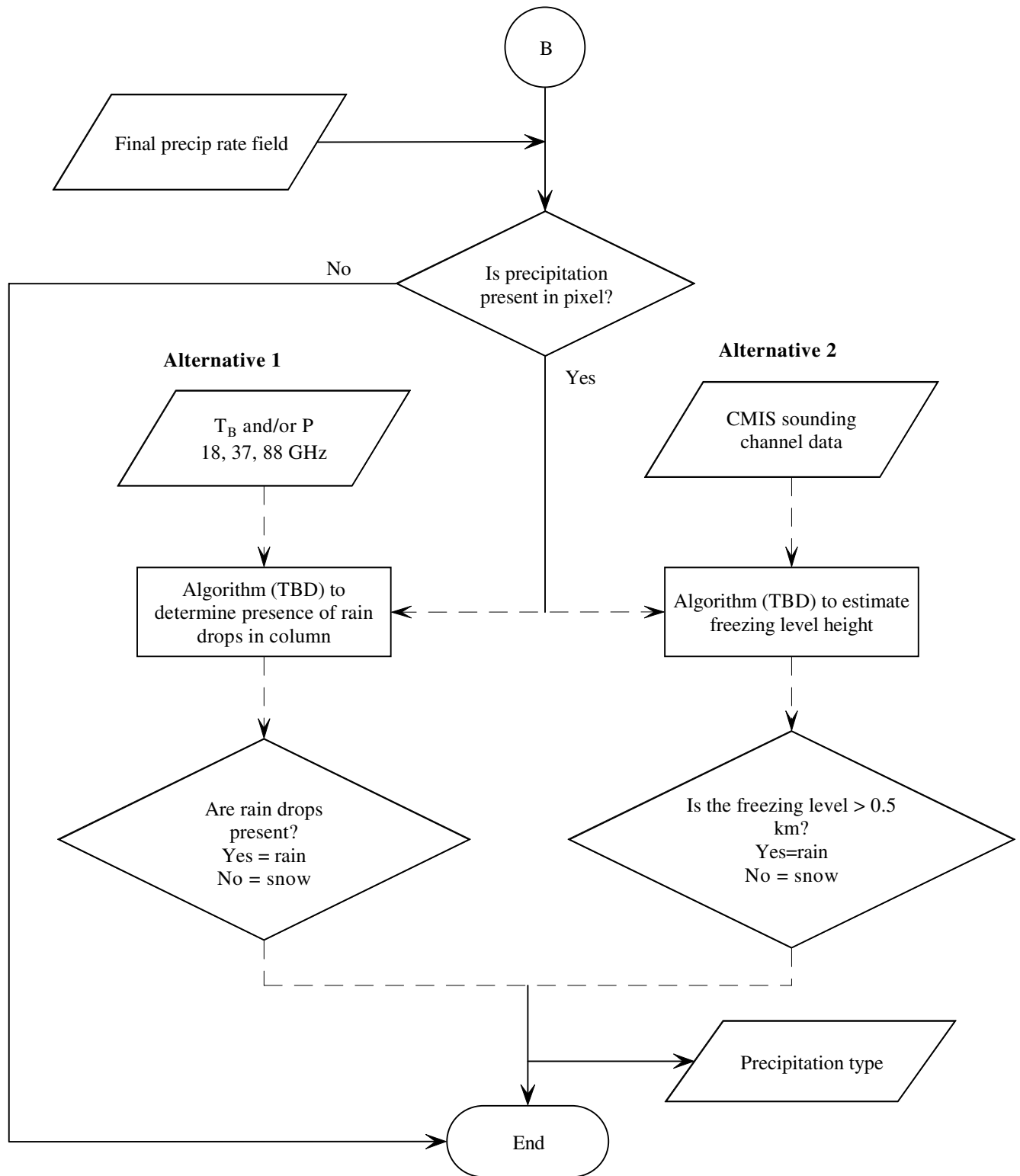


Figure 4: Flow diagram illustrating the overall logic of the precipitation type classification.

3.3. The Forward Radiative Transfer Problem

Because of their high computational cost in comparison to the expected benefits for retrieval performance, real-time forward radiative transfer calculations are not undertaken as part of the

precipitation retrieval algorithm. Nevertheless, it is useful to review the details of the radiative transfer equation (RTE) as it applies to passive microwave remote sensing of precipitation, so as to highlight the numerous areas of uncertainty and ambiguity in model-derived relationships between surface precipitation rate and CMIS brightness temperatures. The existence and likely magnitude of these uncertainties not only justifies the highly simplified physical inversion approach utilized for ocean rainfall retrieval, they also underscore the difficulty of making confident estimates of true algorithm global performance based solely on simulated retrievals from model-generated data.

Utilizing the Rayleigh-Jeans approximation, the full differential form of the RTE for polarized monochromatic microwave brightness temperatures is written:

$$\hat{\mathbf{s}} \cdot \nabla \mathbf{T}_B(\mathbf{r}, \hat{\mathbf{s}}) = -\boldsymbol{\alpha}_e(\mathbf{r}, \hat{\mathbf{s}}) \cdot \mathbf{T}_B(\mathbf{r}, \hat{\mathbf{s}}) + \boldsymbol{\alpha}_a(\mathbf{r}, -\hat{\mathbf{s}})T(r) + \int_{4\pi} \mathbf{P}(\mathbf{r}, \hat{\mathbf{s}}, \hat{\mathbf{s}}') \cdot \mathbf{T}_B(\mathbf{r}, \hat{\mathbf{s}}) d\Omega \quad \text{Equation 1}$$

where

$$\mathbf{T}_B = \begin{bmatrix} T_{Bv} \\ T_{Bh} \\ T_U \\ T_V \end{bmatrix} \quad \text{Equation 2}$$

is the brightness temperature expressed as a modified Stokes vector, \mathbf{r} is the position vector, and $\hat{\mathbf{s}}$ is a unit vector describing the direction of propagation. The local optical variables appearing in Equation 1 are the extinction matrix $\boldsymbol{\alpha}_e$, the absorption vector $\boldsymbol{\alpha}_a$, the scattering phase matrix \mathbf{P} , and the thermodynamic temperature T .

If the above variables are known at every point \mathbf{r} in a 3-D domain and for every orientation vector $\hat{\mathbf{s}}'$ (where applicable), and if suitable boundary conditions are supplied, such as the cosmic background brightness temperature T_{cosmic} and the surface bidirectional reflectance matrix $\mathbf{R}(\hat{\mathbf{s}}, \hat{\mathbf{s}}')$, then the DRTE may in principle be integrated numerically to determine the top-of-the-atmosphere polarized brightness temperatures along a given ray $\hat{\mathbf{s}}$ intersecting the earth's surface at position (x, y) .

ALGORITHM DESCRIPTION

Note that this form of the RTE does not neglect scattering, and does not assume plane parallel geometry, in contrast to the usual assumptions for microwave radiative transfer outside of precipitation. Microwave scattering is invariably important in rain clouds because of frozen and liquid hydrometeors (raindrops, snow flakes, graupel, etc.) whose diameters (typically 0.1 to 10 mm) are comparable to the wavelengths of the radiation. Although a few stratiform rain clouds exhibit relatively homogeneous horizontal structure over large areas, so that they may be reasonably approximated as plane-parallel, field observations by aircraft and radar reveal that such rain clouds are the exception rather than the rule. On the contrary, all convective rain cells, and many instances of stratiform precipitation, reveal significant microphysical variability on scales of 1-10 km or less in both the horizontal and vertical dimensions.

In the full form given above, the numerical solution of the RTE is computationally cumbersome, but it may nevertheless be solved, in principle, to almost arbitrary accuracy using a Backwards Monte Carlo code, as discussed by Petty (1994a), Petty et al. (1994), and Roberti et al. (1994).

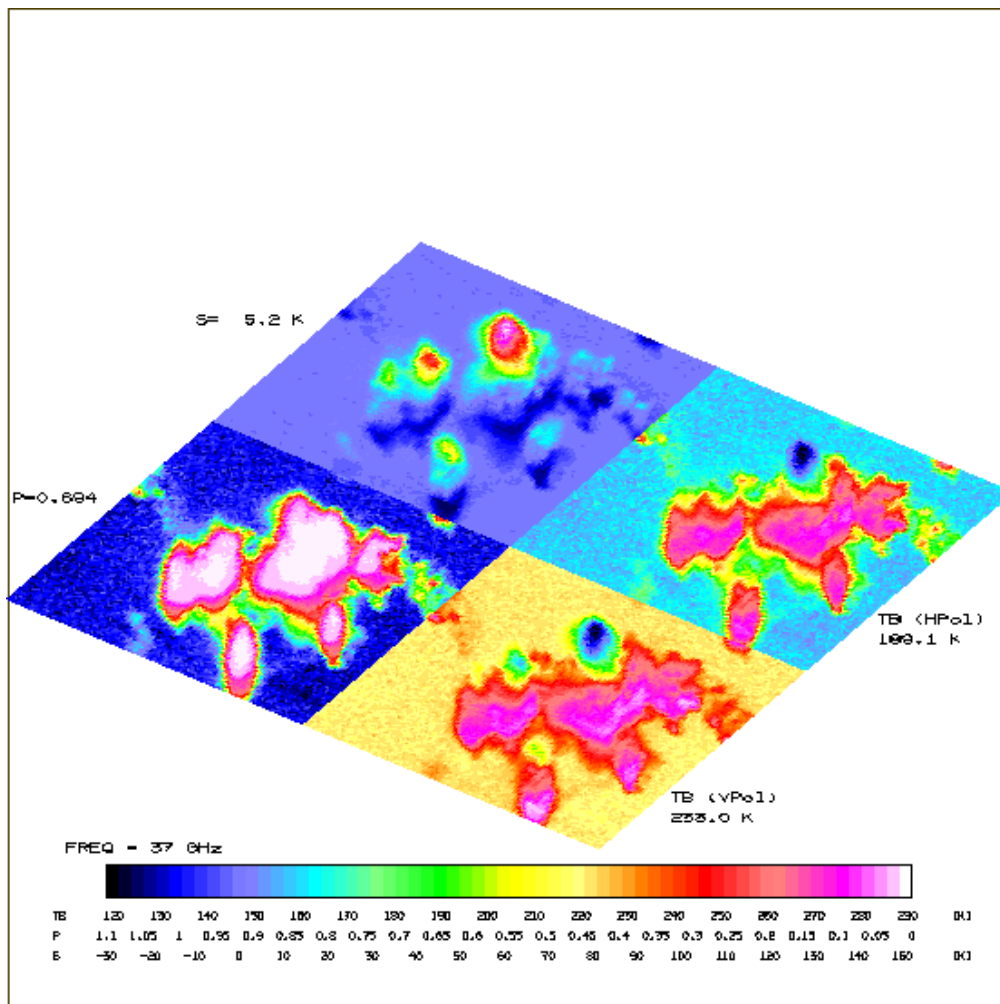


Figure 5: An example of a Backwards Monte Carlo simulation of a high-resolution satellite image at 37 GHz for a mesoscale convective system (MCS) viewed at 53° incidence. Each panel represents one model domain with dimensions 50 km x 50 km. Right: Horizontally polarized brightness temperature. Bottom: Vertically polarized brightness temperature. Left: Normalized polarization P . Top: Polarization-corrected scattering index S .

In theory, the ability to undertake simulations of radiative transfer in realistic rain clouds permits the relationship between cloud optical properties and CMIS radiances to be investigated in detail and also allows arbitrarily detailed and varied test cases to be developed for assessing algorithm performance. In practice, however, even current Monte Carlo codes invoke numerous simplifications and assumptions in order to make the problem manageable. Most commonly, these include the utilization of simplified scattering phase functions, neglect of the dependence of optical parameters on \hat{s} (i.e., directionally isotropic scattering and extinction), utilization of scalar rather than vector radiative transfer, and other compromises. These approximations introduce errors into the calculations whose magnitude can in many cases only be guessed.

In addition to the above generic simplifications to the radiative transfer code itself, the specification of local extinction and scattering properties for a “representative” rain cloud involves a long chain of assumptions and approximations, some of which are of an *ad hoc* nature and therefore of questionable applicability to real rain clouds. A single poor approximation at any point in the chain may have serious consequences for the overall accuracy of the RT results, which in turn affects the quality of the retrieval algorithm based on those results and the confidence one may have in any model-based assessment of algorithm performance.

The following outlines the usual approach to specifying 3-D optical parameters in rain clouds for microwave RT purposes and highlights some of the important weak links in the chain of assumptions:

3.3.1. Macroscopic cloud structure

Historically, rain clouds have most often been assumed to be 1-dimensional (plane-parallel) for microwave radiative transfer purposes. Typically, a stratiform rain cloud is modeled as a single elevated layer of cloud, some portion of which usually extends above the 0° isotherm and is therefore supercooled. Within the supercooled layer, precipitation growth occurs via vapor deposition (the so-called Bergeron process), leading to snow crystals, possibly followed by aggregation these snow crystals into snowflakes and/or accretion of supercooled cloud droplets, leading to rimed particles called graupel. These frozen particles then fall through the 0° level and melt within 0.5 km or so to form raindrops. Within the cloud layer, the raindrops may continue to grow by collision-coalescence; below cloud in subsaturated air, they begin to evaporate and may or may not reach the surface.

In the early development of passive microwave algorithms for rain rate retrieval, it was common to simply prescribe the total column cloud water in the cloud layer, the freezing level, and a constant effective precipitation rate from the surface through the freezing level. It was then assumed that precipitation above the 0° level was entirely frozen (i.e., snow or graupel). This frozen precipitation was modeled as an exponential (e.g., Marshall-Palmer) size distribution of solid ice spheres. Beyond these basic assumptions, no provision was made for ensuring the meteorological realism or microphysical self-consistency of the rain cloud model. For example, evaporation of rainfall below cloud base can significantly alter the relationship between total

column attenuation due to precipitation and surface precipitation rate, but in the early models, rainfall rate was assumed constant between the surface and the freezing level.

Recently, Petty et al. (2000) attempted to develop a more rigorous and physically self-consistent approach to specifying 1-D profiles of hydrometeors in stratiform rain clouds. For example, vertical derivatives of the precipitation rate profiles associated with various hydrometeor classes are explicitly parameterized in terms of environmental humidity, temperature, cloud water content, etc. According to their method, approximately 10 free parameters are required to completely specify a 1-D rain cloud for microwave radiative transfer purposes.

Even in a relatively complete and physically self-consistent 1-D model, certain processes are not well constrained by observations or existing theory and must therefore be parameterized in an arbitrary manner. For example, precipitation growth and evaporation rates can be sensitive functions of assumed particle size distributions, shapes, and fall speeds, especially for graupel and snow particles. A wide range of combinations of model parameter values yield plausible precipitation profiles; however it remains impossible, due to scarcity of suitable observations, to ascertain which of these combinations are most representative of actual rain clouds in any given environment.

Moreover, there is now growing recognition that 1-D representations of rain clouds are seldom realistic for any but the most ideal stratiform cases. This is both because of the 3-D nature of the radiative transfer equation itself (when scattering is important) and because microphysical properties and processes in many rain clouds, especially convective clouds, simply do not lend themselves to a one-dimensional description whenever there are significant lateral exchanges of moisture, energy, etc., between the rain cloud and the surrounding environment.

Until fairly recently, there were few satisfactory alternatives to 1-D representations. 3-D radiative transfer codes (e.g., forward Monte Carlo) were prohibitively expensive to run for all but the simplest geometric structures. Computational expense aside, there has been no completely satisfactory basis for representing to a RT model the complex and highly variable shapes of real rain clouds.

The first of the above two problems was partly alleviated as computers became more capable and also with the emergence of backwards Monte Carlo radiative transfer codes, which are

reasonably efficient for simulating satellite microwave images of 3-D rain clouds viewed from a single vantage point.

In principle, utilizing cloud-resolving weather prediction models to generate realistic 3-D distributions of hydrometeors could solve the second problem. In practice, there remain several difficulties:

- Current-generation dynamic cloud models still have difficulty producing realistic fine-scale (1 km or less) structure in simulations of mesoscale and synoptic-scale cloud systems. Simulated microwave images generated from cloud model simulations of precipitating weather systems typically appear much smoother, and reveal significantly different mesoscale and synoptic scale organization, than their real-life counterparts. The use of nested high-resolution subdomains in the model simulations does not appear to completely alleviate this problem.
- Even if a given cloud model simulation were perfect in its reproduction of a particular instance of a rain cloud structure, a single such case is not enough. Rather, the development of an optimal global rainfall retrieval algorithm, and any credible assessment of the true global performance of such an algorithm, requires a *statistically representative spectrum* of cloud structures for each of many widely differing environments in which precipitation occurs. A comprehensive library of high-resolution cloud model simulations for all different seasons and regions of the globe simply does not yet exist.

3.3.2. Microphysical properties

In addition to the problem of specifying the 3-D distribution of bulk condensed water (liquid and solid) at 1 km or better horizontal resolution over a mesoscale to synoptic-scale model domain, it is further necessary to describe the microphysical form (or habit) of the hydrometeors. Cloud microphysical parameterizations widely today only distinguish between a few broad hydrometeor categories: *cloud water*, *rain water*, *graupel* or *hail*, *snow*, and *cloud ice*. For each of these hydrometeor categories, most practical models only provide a bulk mass mixing ratio or density. The assumed particle size distributions are usually “hardwired” functions of total hydrometeor concentration, and most cloud models yield no predictions whatsoever concerning particle shapes and densities.

In reality, graupel and snow particles in particular exhibit a tremendous range of morphologies, which in turn are associated with variable fall speeds, growth rates, and particle densities. For example, snow may occur as pristine vapor-grown ice crystals of various habits (depending on the growth environment), as large aggregates of unrimed or rimed crystals, or anything in between. Distinctions of this type are critically important for the hydrometeor growth and fallout processes which a cloud model attempts to simulate, but it is not yet practical to accommodate these distinctions in any but the most sophisticated and computationally expensive experimental models.

Recently, Petty et al. (1999) ran the MM5 community mesoscale model in two 36-hr simulations of the same extratropical oceanic cyclone. The two model runs were identical except for the choice of the bulk microphysical scheme used: one utilized Reisner et al. (1998) while the other utilized Tao and Simpson (1993). The resulting differences were profound: one yielded considerably more snow and graupel aloft than the other, and both yielded large-scale precipitation patterns that bore as little resemblance to each other as either did to the precipitation patterns observed in the actual cyclone by the SSM/I.

In summary, current-generation cloud models incorporating conventional bulk microphysical schemes cannot yet accommodate the variety of particle types and size spectra that are known to exist in rain clouds. Because hydrometeor growth and fallout rates are sensitive to such details, there is further reason to question whether cloud models can yet produce *statistically representative* microphysical and macrophysical representations of real rain clouds for microwave radiative transfer purposes. This does not prevent the use of dynamic models coupled with 3-D radiative transfer models for understanding the qualitative influence of various cloud properties on satellite microwave observations of rain clouds. However, it does undermine their utility for developing *unbiased, quantitative multichannel relationships* between microwave observables and surface rain rates.

Additional information concerning cloud microphysical structure is provided by instrumented aircraft and by radar observations. Airborne microphysical observations have yielded considerable insight into the variety of hydrometeor types and growth processes that occur in rain clouds and their relationship to certain environments. However, it is not clear how to generalize from storm-specific, localized aircraft observations to reasonably credible and

detailed 3-D representation of the mesoscale and microphysical structure of precipitating cloud systems and their regional and seasonal variability.

Another important source of insight into km-scale (or smaller) rain cloud structure is radar. However, conventional radar is currently able to provide only the following types of information: (1) 3-D distribution of radar reflectivity, which in turn is approximately proportional to the sum of the 6th powers of the particle diameters in a unit volume of air, and (2) qualitative indications of particle category (e.g., hail, rain, snow) based on observed backscatter polarization properties, when available. Furthermore, most standard radar equipment cannot detect non-precipitating cloud water or ice.

3.3.3. Microwave optical properties

Once the 3-D distribution of hydrometeors in representative rain clouds, including detailed shapes, sizes, and densities, are specified for use in microwave radiative transfer calculations, it remains necessary to accurately translate these particle geometric properties into 3-D distributions of (in the scalar approximation) the microwave volume extinction coefficient k_{ext} , single scatter albedo ω and scattering phase function $p(\Theta)$. This is yet another potentially weak link in the chain of assumptions that ultimately relate microwave observables to surface precipitation rate. We address each of the different major classes of hydrometeors in turn.

3.3.3.1 Cloud liquid water

The simplest case is that of cloud liquid water, which consists of spherical droplets much smaller than 100 μm in radius. For these droplets, the Rayleigh small-particle approximation applies over much of the microwave spectrum, yielding the following expression for mass extinction coefficient, independent of droplet radius:

$$\kappa = \frac{6\pi\nu}{\rho c} \text{Im} \left(\frac{m^2 - 1}{m^2 + 1} \right) \quad \text{Equation 3}$$

In addition, the single scatter albedo ω for small droplets is negligible; therefore microwave extinction and emission due to cloud liquid water may be treated in a manner analogous to that of an absorbing gas. The sole potential source of major uncertainty in cloud water absorption/emission calculations appears to lie in the model for the dielectric constant of water at microwave frequencies. Commonly used models (e.g., Ray 1972, Liebe et al. 1991) are

reasonably well tuned to laboratory observations at temperatures above freezing and at low to moderate microwave frequencies. At sub-freezing temperatures, on the other hand, laboratory measurements are scarce, and models of the dielectric constant of water tend to diverge from one another, especially at higher microwave frequencies (Petty 1990, Lipton et al, 1999).

Although direct validation of the absorption coefficient due to cloud water has not been possible, due to a lack of suitable in situ measurements, Westwater (19XX) examined the ratios of apparent total absorption due to clouds at three different frequencies (20.6, 31.65, and 90 GHz) and found that these ratios deviated from theory by up to 30%. Although some of the discrepancy may be explained by other error sources, there is an implication that the spectral dependence of the dielectric coefficient for water may be somewhat in error in the standard models. This subject requires further investigation.

3.3.3.2 Rain drops

Raindrops are liquid water drops large enough to fall an appreciable distance from their point of origin in a cloud. Conventionally, the radius threshold that is taken to distinguish cloud droplets from raindrops is 100 μm . Unlike cloud droplets, raindrops generally do not satisfy the criterion for the Rayleigh approximation and thus the more general Mie theory must be used. Microwave extinction is a fairly strong function of drop radius, and scattering is non-negligible, though ω remains of the order of 0.6 or less for most combinations of drop size and wavelength.

Larger raindrops are not strictly spherical but rather flattened or even cupped in shape (Beard et al. 1989). The non-sphericity of large raindrops alters the extinction and scattering properties relative to Mie results for spheres and has been shown to lead to detectable polarization effects for passive microwave measurements taken at oblique elevation angles.

However these are generally regarded as a second order effects relative to other sources of brightness temperature variability; hence the modeling of raindrops as equivalent-volume spheres is probably acceptable for most purposes.

Crucial for determining the precise relationship between microwave optical properties of rainfall and bulk microphysical properties, such as precipitation rate or precipitation water content is the drop size distribution $N(D)$, which is defined such that $N(D)dD$ is the number of raindrops per unit volume whose volume-equivalent spherical diameter D falls in the range $[D, D+dD]$. Bulk

microphysical or optical properties are then computed as suitable moments of $N(D)$. For example, the rain water content (mass per unit volume air) is given by

$$w_R = \rho_l \frac{\pi}{6} \int_0^\infty N(D) D^3 dD \quad \text{Equation 4}$$

The precipitation rate through a fixed horizontal surface is given by

$$R = \frac{\pi}{6} \int_0^\infty N(D) D^3 (v(D) - W) dD \quad \text{Equation 5}$$

where W is the local updraft speed and $v(D)$ is the terminal fall speed of a rain drop in still air. This fall speed depends not only on drop diameter but also air density and viscosity; therefore the same $N(D)$ will yield different precipitation rates under different conditions of pressure and temperature. Empirical expressions for $v(D)$ for raindrops are given by Pruppacher and Klett (1997).

Note that it is R , evaluated at the earth's surface, that is retrieved by the CMIS Precipitation Module. At the surface, the updraft speed W can be taken to be zero. However, W may be significantly different from zero even a short distance above the surface, especially in convective situations. This possibility introduces a potentially substantial uncertainty into the relationship between *surface* rain rate and the mean drop size distribution $N(D)$ in even the lowest kilometer above the surface.

Bulk microwave extinction and scattering properties of falling rain are evaluated at a particular microwave frequency ν in a similar fashion, by integrating the Mie-derived extinction and scattering cross-sections over all drop sizes. Thus, the volume extinction coefficient k (dimensions of length^{-1}) is given by

$$k = \frac{\pi}{4} \int_0^\infty Q_{ext}(D) D^2 N(D) dD, \quad \text{Equation 6}$$

where Q_{ext} is the extinction efficiency. Similarly, the single scatter albedo and scattering phase function are given by

$$\omega = \frac{\int_0^\infty Q_{sca}(D) D^2 N(D) dD}{\int_0^\infty Q_{ext}(D) D^2 N(D) dD} \quad \text{Equation 7}$$

$$P(\Theta) = \frac{\int_0^{\infty} P(\Theta; D) Q_{sca}(D) D^2 N(D) dD}{\int_0^{\infty} Q_{sca}(D) D^2 N(D) dD} \quad \text{Equation 8}$$

where Q_{sca} is the scattering efficiency and $P(\Theta; D)$ is the scattering phase function for an individual particle of diameter D .

In addition to expressions for the above efficiencies Q and the scattering phase function P , evaluation of all of the above integrals requires a suitable assumption concerning $N(D)$.

Most commonly, the size distribution of rain drops is modeled as exponential, so that

$N(D) = N_0 \exp(-\Lambda D)$. For any particular choice of N_0 , Equations 4 and 5 govern the functional relationship between the slope parameter Λ and the rain rate R (in still air) and between Λ and w_R . The empirically derived Marshall and Palmer (1948) relationship sets N_0 constant at $8 \times 10^6 \text{ m}^{-4}$. Marshall and Palmer also specify Λ as a power-law function of rain rate R , but utilization of this relationship leads to moderate inconsistencies ($\sim 10\%$) between the nominal rain rate and the computed rain rate obtained from equation 5 when using an accurate fall speed relationship.

Although the Marshall-Palmer relationship is regarded as generally valid as a model for the *mean* drop size distribution observed over a large number of diverse rain events, it is frequently a poor approximation to reality in individual rain events. Differing precipitation particle growth mechanisms, and subsequent evaporation and/or drop size sorting (due to the dependence of fall speed on D), can lead to local drop size distributions that deviate wildly from the Marshall-Palmer model and, indeed, from any simple mathematical model of $N(D)$. Although a variety of other empirical relationships (including three- or four-parameter models) have been published for specific types of precipitation (e.g., convective vs. stratiform, etc.), there is as yet no accepted basis for accurately prescribing $N(D)$ for all of the many different meteorological environments encountered in rain events around the world.

An attractive alternative to specifying the form of $N(D)$ *a priori* for rain rate retrievals would be to simultaneously retrieve one or more moments or parameters of $N(D)$ along with the rain rate. Unfortunately, experience to date suggests that the microwave spectral signature of these parameters is not sufficiently strong or distinct to permit their retrieval in the presence of

numerous other sources of geophysical noise. This is especially true when a layer of frozen precipitation aloft is situated between the satellite vantage point in space and the layer of rain below the melting level.

In summary, uncertainty in the correct specification of $N(D)$ for rainfall at various points throughout a 3-D model domain is an important source of uncertainty in the calculation of the microwave optical properties k , ω , and $p(\Theta)$ at those points. Not only does it introduce potentially significant errors into forward calculations of microwave radiance, but uncertainties in $N(D)$ are also major sources of uncertainty in the estimation of surface rain rate from radar data, which is frequently (and often too uncritically) employed as “ground truth” for satellite precipitation estimates.

3.3.3.3 Cloud ice

Cloud ice particles are either significant for microwave radiative transfer calculations or not, depending on their size relative to the wavelength. It is generally assumed that ordinary cirrus particles are too small, and too weakly absorbing, to have a noticeable impact on observed radiances at most common microwave frequencies. When the cloud ice particles are larger, as is often the case in some denser cirrus clouds (e.g., remnants of cumulonimbus anvils) they may have a non-negligible impact on microwave observations, especially at higher frequencies. When that is the case, the computation of their optical properties follows the methods described for precipitating ice (see below), and is subject to similar uncertainties.

3.3.3.4 Frozen Precipitation

As noted in Section 4.3.1, frozen precipitation commonly develops in the supercooled portions of clouds. In fact, the majority of rainfall reaching the surface in most climate zones originates as frozen precipitation aloft. Initially, ice particles introduced into a supercooled cloud grow by vapor deposition, leading to the formation of snow crystals. These are typically highly structured and delicate. The precise manner of snow crystal growth is highly sensitive to the environment: various combinations of humidity and temperature may lead to ice columns, needles, plates, dendrites, and any of an infinite number of possible combinations of these basic forms.

Under favorable conditions (e.g., warm temperature and/or dendritic crystal structure), individual snow crystals may aggregate into larger assemblages known as snowflakes. Snowflakes are

typically of very low density (approximately 1 part ice to 10 or more parts air) but may achieve diameters of up to several centimeters in extreme cases.

As vapor-grown snow crystals particles become large enough to fall relative to suspended cloud water droplets, they may begin to accrete supercooled droplets in a process known as riming. If continued, the particle evolves from a vapor-grown snow crystal to an amorphous, irregular particle of rime ice, known as graupel. Frozen precipitation particles observed in the field may be found at any point on the morphological continuum between delicate vapor-grown crystals and densely rimed graupel particles.

Because graupel and snowflakes are not only non-spherical but may exhibit highly irregular and variable shapes from one particle to the next, one cannot, in general, specify a unique relationship between particle size and fall speed, unlike the case for raindrops. Rather, it is often preferable to specify a mass-weighted mean fall speed \bar{v} and total hydrometeor density w (mass of ice per unit volume of air), in which case the liquid-equivalent precipitation rate through a fixed horizontal surface is approximately given by

$$R \approx \frac{[\bar{v} - W]w}{\rho_l} \quad \text{Equation 9}$$

where ρ_l is the density of liquid water ($\sim 1000 \text{ kg/m}^3$) and W is the updraft speed of the air in which the particles are suspended. Mass weighted fall speeds typically range from less than 1 m/s for snowflakes to 3-6 m/s or more for denser graupel particles. Because of the low fall speed of snow ($\sim 1 \text{ m/s}$ or less), a given precipitation rate may correspond to a fairly high concentration of total snow mass concentration w . For example, a 10 mm/hr liquid-equivalent precipitation rate might correspond to a snow mass concentration approaching 3 g/m^3 .

Note further that because the fall speed of snow is three to four times smaller than that of rain, even a weak updraft or downdraft in the atmospheric column can have a large effect on the relationship between mean w and surface snowfall rate. Since microwave radiometers like CMIS are sensitive to column-integrated optical properties of hydrometeors, uncertainty in W in any given case can introduce large uncertainty into retrieved instantaneous surface precipitation rate.

The next subsections describe techniques for modeling the microwave extinction and scattering properties of frozen precipitation particles.

3.3.3.4.1 Graupel

Graupel particles are distinguished from snowflakes by their amorphous (non-crystalline) macroscopic structure, relatively high density and compact shape. Graupel may come in various forms, depending on the precise mode of growth and the degree to which riming has obscured the structure of the original vapor-grown snow crystal or aggregate. Sometimes, graupel particles maintain constant orientation as they fall, so that growth by riming occurs predominantly on the downward-directed base of a conically shaped particle. Otherwise, graupel particles appear as irregular lumps or spheroids. Graupel particles may range in diameter from approximately 0.1 mm to several mm.

A common approach to modeling microwave properties of graupel is to treat them as spheres composed of a mixture of ice and air. Typically, the proportion of ice by volume is estimated to be 80-90%. Presumably, the exact proportion is variable, but inadequate field data exist to allow a more precise characterization.

Given a dielectric mixture in which the scale of the heterogeneity is small compared to the wavelength, one may define an effective bulk dielectric coefficient for the mixture and then compute scattering properties for the entire particle (e.g., using Mie theory) as though it were homogeneous. Two general dielectric mixing formulas are in wide use: that of Bruggeman (1935) and Maxwell Garnett (1904). The Maxwell Garnett formula is derived by assuming that one of the two constituents takes the form of small inclusions embedded in a matrix consisting of the second constituent. The computed effective dielectric constant derived from the Maxwell Garnett mixing formula is, in general, sensitive to a reversal of the roles of the two constituents.

The Bruggeman formula gives an alternative method of computing the bulk dielectric constant of a mixture. Unlike Maxwell Garnett, the Bruggeman formula treats the two components symmetrically – i.e., there is no need to specify which one is the inclusion and which one is the matrix. The numerical results for Bruggeman tend to lie between those produced by Maxwell Garnett for the two permutations of matrix and inclusion.

It is not clear whether graupel is better modeled as a mass of ice inclusions (i.e. frozen cloud droplets) embedded in a matrix of air or rather a matrix of solid ice with air inclusions, or whether instead the Bruggeman formula is more realistic in its symmetric treatment of both constituents. Fortunately, in the case of ice-air mixtures the choice has only a relatively minor effect on the results, because of the relatively weak interaction of ice with microwave radiation.

More problematic is the specification of the particle size distribution $N(D)$ for graupel. There are few published measurements of graupel size spectra, and there is little reason to suppose that size spectra will be the same from one rain cloud to another. On the contrary, individual particle size depends primarily on total time spent growing in cloud and on the supercooled cloud water density, not necessarily on total precipitation rate or graupel water content. Unlike raindrops, graupel is not subject to breakup due to collisions or hydrodynamic instability at large sizes. Therefore, there is less opportunity for a predictable size spectrum to emerge via a steady state balance between growth and breakup processes.

In the absence of specific evidence to the contrary, most investigators model graupel as following an exponential size distribution $N(D)$ similar to that for raindrops, where D is now the liquid-equivalent (melted) spherical diameter of the particle. Indeed, some models even utilize the Marshall-Palmer relationship between the slope parameter Λ and rain rate R , though there is no particular reason to believe that this relationship holds for graupel.

The non-spherical nature of many graupel particles also calls into question the use of Mie theory to compute microwave extinction properties. A number of computational techniques exist for obtaining optical properties of non-spherical particles. Graupel particles are reasonably good candidates for most of these methods owing to the relatively small dielectric constant of ice, relatively modest ratio of graupel particle size to microwave wavelength, and the comparatively compact shapes of these particles. Nevertheless, such calculations remain tedious and time consuming when whole families of shapes, sizes and orientations must be considered. Furthermore, the specification of a realistic statistical distribution of each of these properties for graupel is problematic, in view of the lack of quantitative observations.

Turk et al. (1999) modeled microwave radiative transfer in a rain cloud assuming that graupel particles were conical in shape and oriented with their axes predominantly vertical. Their calculations of microwave brightness temperature for an obliquely viewing satellite radiometer

revealed a strong polarization effect due to the presence of oriented particles. Although polarization effects are indeed observed in some rain clouds by satellite radiometers, the observed magnitude of the polarization difference is generally smaller than that predicted by the above model. Hence, we conclude that a compromise between the standard assumption of spherical particles and that of highly oriented non-spherical particles might yield more realistic results. No such model has ever been tested, to our knowledge.

To summarize, we believe that uncertainty in the size distribution of graupel particles constitutes a major source of uncertainty in the calculation of the microwave optical properties of graupel. Fall speed relationships are also variable and inadequately documented, introducing uncertainty into the relationship between graupel particle concentration in the atmospheric column and precipitation rate, as well as into the parameterization of cold cloud processes in dynamic cloud models used to generate 3-D hydrometeor fields for radiative transfer simulations. Secondary sources of uncertainty probably include (1) the effects of variable particle density (ice-air ratio), (2) the choice of dielectric mixing formula, and (3) the effects of variable shape. A high priority of future research should be to quantify some or all of these uncertainties.

3.3.3.4.2 Snow

There currently exist no fully validated models for microwave interactions with snow crystals and snowflakes. The reasons are threefold:

1. There is as yet no generally accepted model for realistically representing the detailed, quasi-fractal physical structure of a typical snowflake. Such a model is a prerequisite for performing rigorous electrodynamic simulations of scattering and extinction by snowflakes
2. Even if such a physical model existed, the fine-scale structure of a snowflake, combined with its fairly substantial total diameter relative to microwave wavelengths, would test the limits of computational methods otherwise suitable for highly non-spherical particles, such as the Discrete Dipole Approximation (DDA).
3. Field observations of the relevant microwave properties of falling snow, other than radar backscatter, are spotty at best.

In the absence of completely satisfactory theoretical models or empirical observations of microwave extinction and scattering by snow at CMIS frequencies, radiative transfer calculations must be based on somewhat speculative analogues. Examples include the following:

1. Model a snowflake as an equivalent-mass solid ice sphere.
2. Model a snowflake as an equivalent-mass ensemble of numerous smaller, independently scattering solid ice spheres.
3. Model a snowflake as an equivalent-mass spherical ice-air mixture, using Maxwell Garnett or Bruggeman theory to compute an effective mean dielectric constant. In this case, the ice fraction by volume is often taken to be near 10%, a value that is plausible but nevertheless *ad hoc* in the absence of relevant measurements.
4. Apply the Discrete Dipole Approximation to a subjectively defined non-spherical particle shape intended to at least qualitatively approximate that of a real snowflake.

Various authors have utilized methods 1 through 3, but no systematic intercomparison of the three methods has yet been undertaken, to the best of our knowledge. Evidence collected by Petty (2001a) from SSM/I observations of tropical rain clouds suggest that Method 2 or 3 may yield reasonable brightness temperature simulations, provided only that the particle size and/or density assumptions are empirically tuned to match the observed spectral dependence of multifrequency brightness temperatures. In general, it has been found that the mean ice particle sizes must be significantly smaller than those predicted by a standard snow particle size distribution model such as that of Sekhon and Srivastava (1970), otherwise predicted scattering is too intense at 37 GHz relative to that observed at 85.5 GHz.

Unfortunately, none of the empirical evidence to date allows a clear choice to be made among the first three methods, in part because field or satellite observations of microwave radiances or extinction have rarely been coupled with suitable direct measurements of the relevant physical properties of the particles (e.g., mass and diameter). Furthermore, it is not certain whether surface-based observations of snowflake properties (sizes, shapes, fall speeds, etc.) can be safely extrapolated to higher altitudes and colder temperatures in rain clouds.

While potentially the most rigorous of four methods (if the particle structure is correctly specified), Method 4, to our knowledge, has never been attempted except for relatively small, simple ice particle shapes more characteristic of cirrus than of complex snow aggregates.

In theory, radar observations of microwave backscatter can yield some insight into the validity of candidate models for snowflakes. However, radar backscatter is sensitive to different aspects of

the particle geometry than are the optical parameters k , ϖ , and $\mathbf{P}(\Theta)$ required for forward radiative transfer calculations. It is possible, though not certain, that a model that yields satisfactory results for radar backscatter may significantly over- or underestimate microwave extinction and/or scattering, especially scattering at relatively small angles.

In summary, several potential methods exist for parameterizing the microwave optical properties of snowflakes. However, it is presently impossible to attach meaningful estimates of the uncertainty or error to any such model.

3.3.3.4.3 Hail

In terms of the growth processes involved, hailstones are merely an extreme form of graupel. The primary differences lie in the particle size, which can exceed 10 cm or more in rare cases, and in the fact that hailstones often experience wet growth (i.e., freezing of liquid that has spread over the surface) rather than riming.

Because of their large size relative to the wavelength, the presence of hailstones in the atmospheric column can potentially have significant effects on microwave radiative transfer. Furthermore, hail is probably present in at least the upper half of most convective storms producing heavy rain rates at the surface. Because the EDR threshold performance requirements include the ability to measure heavy rain rates of up to 50 mm/hr, the potential implications of hail for CMIS rain rate retrievals must be considered.

Because of the typically wet growth of larger hailstones, the air fraction in hailstones is presumably negligible, thus the dielectric coefficient of pure ice may be used in the interior of the hailstone. However, a surface film or shell of liquid water may be present due to latent heat of freezing, even when the hailstone is well above the melting level. The presence of a liquid water film has profound effects on the microwave scattering properties of an ice particle because of the much larger complex index of refraction of water.

From a theoretical perspective, modeling the microwave properties of a hailstone is straightforward, as analogues to Mie theory have been derived for coated spheres. However, in order for such computations to be quantitatively useful, it is necessary to accurately specify not only the radius of the inner ice core but also the thickness of the outer water shell. At present, even cloud models that explicitly predict the growth and fallout of hail in convective storms

(sometimes in place of graupel) generally do not provide sufficiently detailed information concerning such hailstone properties. These must therefore be specified in an *ad hoc* way, with unknown implications for the error budget of the radiative transfer calculations.

3.3.3.4.4 Mixed phase precipitation

The melting zone, which extends perhaps 0.5 km or so below the 0°C isotherm, corresponds to a zone of anomalously high radar reflectivity known as the “bright band.” The bright band is normally observed in stratiform precipitation, where snowflakes and aggregates melt and collapse in a fairly orderly fashion as they descend to lower altitudes. Theoretical explanations for the bright band generally invoke a combination of (1) a dramatic increase in snow particle reflectivity, as large aggregates begin to become coated with a film of liquid water, followed by (2) a subsequent reduction in per-volume reflectivity due to two factors: a reduction in the particle diameter as the low-density snowflake collapses to a raindrop and a corresponding increase in the fall speed, reducing the number concentration of particles in a given volume of air.

There is growing recognition that the melting zone may have important implications for passive microwave radiometry as well, owing to enhanced microwave extinction and emission per unit volume relative to either the snowfall above the 0°C isotherm or the pure rain below the melting zone. One study (ref?) suggested that precipitation in the melting zone may be up to four or more times as attenuating (per unit distance) as rainfall of the same intensity. However, conclusions about this and related issues are extremely sensitive to one’s assumptions about particle fall speed and to the model used for microwave extinction by melting snowflakes.

Similar to the case for dry snowflakes, one may utilize the dielectric mixing formula of either Maxwell Garnett or Bruggeman. However, now three constituents (ice, water, and air), rather than two, must be considered. This requires an extension of the mixing formulas, which were originally derived for only two components. The method employed by Petty (2001b) entails computing an effective dielectric coefficient for a mixture of two of the three components and then using the formula a second time applied to a combination of the first mixture and the third pure component. In the case of the Maxwell Garnett method, there are 12 different possible permutations of the three constituents and, as noted by Meneghini et al. (1999), the computed effective dielectric function is very sensitive to which one is utilized. Unfortunately, in the

absence of suitable direct measurements of the microwave properties of melting snowflakes, there is little clear support for any particular choice.

In summary, modeling of the melting layer in rain clouds for microwave radiative transfer purposes remains a relatively new area of endeavor that, to date, has yielded little reliable guidance. It is therefore difficult to characterize the likelihood of gross errors in computed microwave radiances resulting from ad hoc assumptions of the type outlined above.

3.3.4. Radiative transfer simplifications

In view of the numerous uncertainties in key optical parameters in rain clouds, there is little justification for using the most accurate and comprehensive form of the microwave radiative transfer equation as given by Equation 1. The introduction of certain simplifications greatly reduces the conceptual complexity and computational burden associated with solving the RTE, while contributing errors that are believed to be tolerable in comparison to the other error sources. Key simplifications utilized in microwave remote sensing of precipitation include the following:

3.3.4.1 Directionally isotropic optical properties

In general, when preferentially oriented non-spherical hydrometeors (e.g., ice crystals, flattened raindrops) are present, microwave extinction and scattering coefficients in a volume of cloud depend on the direction of the incident radiation. The specification of such a directional dependence at every point in a 3-D domain is cumbersome and depends on highly uncertain models of mean radiative extinction and scattering by oriented non-spherical hydrometeors. We ignore the directional dependence and specify all optical properties to be independent of incident direction except for reflection from the lower boundary. It is not known how much uncertainty this simplification introduces, but it is believed to be on the order of a few K or less.

3.3.4.2 Scalar radiative transfer

Scattering and extinction of polarized microwave radiation is most accurately treated via the vector form of the radiative transfer equation, in which the radiance is characterized by 4 Stokes parameters, and all transformations of this vector (e.g., via scattering or reflection) are represented via 4x4 matrix operators. Again, the full vector treatment of radiative transfer is considerably more cumbersome than is warranted by the expected additional accuracy.

Therefore we utilize a scalar approximation to the radiative transfer equation in which each polarization (vertical and horizontal) is considered independently. Scattering and extinction parameters aloft are then the same for both polarizations, and only the polarization-dependence of surface emissivity/reflectivity is deemed responsible for most polarization differences observed from space.

Implicit in the above approach is the idea that the original polarization state of a propagating photon is completely “scrambled” the first time the photon undergoes a scattering event. Thus, only radiation directly transmitted (i.e., without scattering) from the surface through the rain cloud contributes to differences in radiances observed in vertical or horizontal polarization. This assumption, though crude, is of great practical importance for the ocean precipitation retrieval algorithm described herein. Its approximate validity has been confirmed through more accurate radiative transfer calculations; the resulting errors are on the order of a few K or less.

3.3.4.3 Simplified scattering phase function

The scattering phase function associated with a given particle, or ensemble of particles, may be a relatively complicated function of the scattering angle. It is common to approximate phase functions for diverse particles as truncated series expansions expressed in terms of orthogonal functions. The number of coefficients that must be retained for good accuracy is generally similar to the size parameter x of the particle, where $x = 2\pi r/\lambda$, r is the particle radius and λ is the wavelength. For a frequency of 150 GHz and a snowflake radius of 5 mm, the size parameter is approximately 15, implying that a similar number of coefficients would be needed to accurately describe the phase function in this case. At the lower frequencies and smaller particle sizes most commonly considered in microwave radiative transfer calculations, the size parameter is proportionally reduced.

For ideal spherical particles, Mie theory is used to compute the phase function. For less ideal particles, other methods exist but are cumbersome. It is therefore common to represent non-spherical particles as “equivalent Mie spheres,” based on mass, surface area, effective dielectric constant, etc., even though there is little theoretical or observational support for the validity of this practice or for the optimal choice of equivalent particle parameters.

Details of the phase function are most important for radiative transfer calculations when a highly directional source of radiation (e.g., the sun) appears in the problem. In passive microwave remote sensing of precipitation, the primary source of radiation is thermal emission, which tends

not to be highly directional (as seen from a given point within the scattering media), except perhaps when a localized strong emitter is viewed at a distance against a cold background (e.g., space, or a strongly reflecting surface). Consequently, the details of the phase function are washed out when radiation arriving from numerous different directions is scattered into the viewing direction. It is therefore reasonable to substitute highly simplified representations of the scattering phase function for the true (e.g., Mie-calculated) phase functions. The simplest common representation utilizes only one free parameter, the scattering asymmetry factor g , to completely characterize the phase function. The angular dependence of scattering is given as a simple idealized function of g . The most widely used function of this type is the Henyey-Greenstein phase function.

For computations in which an analytic phase function is required (e.g., for Monte Carlo computations in 3-D domains), we utilize the Henyey-Greenstein phase function. For 1-D polarized radiative transfer calculations formulated in terms of series expansions of Mie-derived phase matrices, we utilize the full Mie-derived results, but with the understanding that these may in any case give poor approximations to scattering from non-spherical hydrometeors.

The effect of the utilization of simplified phase functions on the accuracy of microwave radiative transfer calculations is unknown but assumed to be of the order of a few K or less. Direct comparisons between exact and approximate methods are needed to quantify the likely contribution to the total error.

3.3.4.4 Surface reflection

Over a perfectly smooth water surface, microwave emissivity and reflectivity is accurately given by the well-known Fresnel relations, which require only the incidence angle and the dielectric coefficient of the water. In general, natural water surfaces are almost never smooth but are roughened to varying degrees by the action of wind. When wind-induced roughening is present, a water surface is no longer strictly a specular reflector. Both small- and large-scale perturbations in the surface height, as well as the presence of wind-induced foam and spray, lead to perturbations in surface emissivity and also broaden the angular distribution of reflected radiation. No completely rigorous model yet exists for modeling these effects. Therefore, it is common to utilize the specular approximation to surface reflection and, where necessary, to apply empirical adjustments for wind roughening. In particular, in cases involving precipitation, surface effects associated with wind roughening and raindrop splashing are believed to be of

second order importance in observed brightness temperature variability. Hence, we adopt the Fresnel model of ocean surface reflectivity with simple adjustments for roughness-induced emissivity changes where required.

With few exceptions, land surfaces are far from smooth on scales of millimeters and larger and therefore cannot be represented as specular reflectors. Rather, inhomogeneities in the soil, vegetation, and topographic variability scatter incident radiation in a variety of directions. Theoretical models for land surface scattering are based on strong idealizations of surface structure and are generally regarded as highly approximate. Moreover, no model can yet accommodate the wide variety of surface and vegetation types encountered globally. We therefore rely heavily on empirical maps of surface emissivity and simple (e.g., Lambertian) models of the angular distribution of scattering

As is the case for several other simplifications discussed earlier, we have no accurate basis for quantifying the errors introduced by this approximation but we believe them to be on the order of ~ 1 K.

3.3.5. Forward Model Used For Rain-Rate Studies Over Land

The general radiative transfer approach, and the OSS implementation, are described in detail in the Core Module ATBD. The tests described here use a specialized version of OSS, called OSSCAT. Since this is a non-polarized radiative transfer code, no explicit distinction is made between the horizontal and the vertical polarizations. OSSCAT is a combination of OSS and an extension of the CHARTS model (Code for High-resolution Accelerated Radiative Transfer with Scattering) to the microwave-submillimeter region (Moncet and Clough 1997). CHARTS is based on the adding-doubling method, with a specified number of discrete angles for the radiance computation. The individual electromagnetic efficiencies are computed off-line, using the Mie code, and the integration over the particle size distribution can be done outside or inside the forward model. The main advantage of this latter option is that it eases the modification and the impact study of the distribution. It also gives us the flexibility of modifying (and retrieving) the effective radius and the variance of the particle size distribution. When several hydrometeor types are present in the same layer, the resulting absorption and scattering coefficients are the sum of each individual absorption and scattering coefficient. The asymmetry coefficient is in this case the weighted average of the individual asymmetry coefficients, the weights being the individual scattering coefficients. The particle size distribution of the liquid rain follows

Marshall and Palmer (1948). The frozen rain particle size distribution follows Sekhon and Srivastava (1970). The non-precipitating cloud liquid water particle size distribution is assumed to follow a gamma function.

Examples of the forward model simulations (over ocean) are shown in Figure 6. It shows the spectral variation of the simulated brightness temperatures for a non-raining situation and for rain rates of 2, 10, and 20 mm/hour. The calculations have been made using the ‘U.S. Standard Atmosphere’ with a wind speed of 7 m/s. The variation of the brightness temperature with the rain rate is consistent with our understanding of the physics. The clear sky brightness temperature is low because the simulations are done over ocean (emissivity ≈ 0.5). As the rain rate increases, the spaceborne instrument sees less and less of the highly polarized radiation emitted by the sea surface, and increasingly sees the radiation emitted by the rainy layer which is both radiometrically warmer and less polarized than the surface. Thus the resulting brightness temperature increases and the polarization difference decreases with increased rain rate.

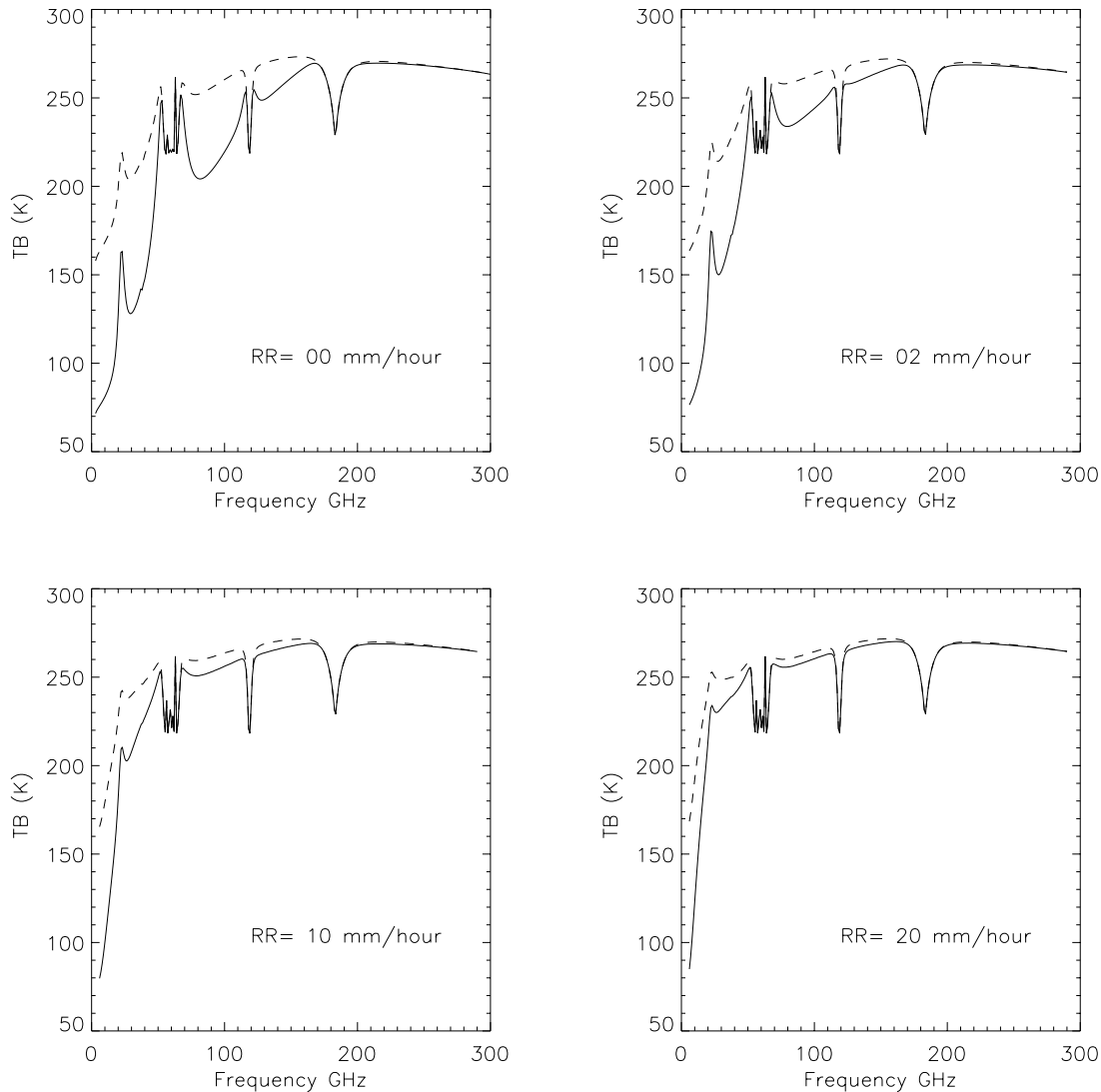


Figure 6: Rain effect on simulated brightness temperatures for both vertical (dashed lines) and horizontal (solid lines) polarizations. Rain has been added in the lowest two layers of the profile. The surface wind speed is 7 m/s. The sea surface emissivity model is based on Wilheit. Results are shown for cases without rain, cases with rain rate of 2 mm/hr, 10 mm/hr and 20 mm/hr. All simulations are done using the U.S. standard atmosphere.

3.4. Mathematical Description of Algorithm

3.4.1. Ocean algorithm

The ocean precipitation rate algorithm has two main parts: (1) a highly simplified forward radiative transfer model that permits the FOV-averaged polarization difference field to be

computed at each frequency from the 2-D surface rain rate field in the CMIS swath, and (2) an algorithm for iteratively improving the agreement between observed and forward-calculated polarization fields.

3.4.1.1 Simplified forward model for polarization

A highly simplified algebraic treatment of the forward radiative transfer for polarized brightness temperatures in idealized rain clouds suggests that the polarization difference (vertical minus horizontal) due to the polarized emissivity of the ocean surface is reduced approximately in proportion to the square of the transmittance of the rain layer. This approximate relationship is borne out by detailed plane-parallel radiative transfer calculations, assuming realistic (1-D) rain cloud structures and hydrometeor properties. Thus, the normalized polarization difference P , defined as

$$P \equiv \frac{T_{BV} - T_{BH}}{T_{BV0} - T_{BH0}} \quad \text{Equation 10}$$

where the brightness temperatures in the denominator represent hypothetical cloud-free ocean brightness temperatures, is approximately related to rain cloud transmittance τ by

$$P \approx \tau^\gamma \quad \text{Equation 11}$$

where the exponent $\gamma \approx 2$ according to a simplified algebraic treatment but is found to be closer to 1.7 based on detailed radiative transfer simulations. P therefore decreases monotonically from unity for a cloud-free scene to near zero for an opaque rain cloud. It is therefore a nearly direct (albeit non-linear) measure of the rain cloud total transmittance, irrespective of the degree of scattering present or of variations in background temperature, ocean surface roughness, atmospheric water vapor content, etc.

For the purposes of the CMIS precipitation module, estimates of the cloud-free ocean brightness temperatures required by Equation 10 are obtained as a byproduct of the CMIS Core Module utilized to retrieve other variables outside of precipitation. Within precipitation, where other environmental parameters cannot be directly retrieved, it is sufficient to interpolate the latter from the surrounding area.

3.4.1.1.1 Dependence of P on local rain rate

The precise relationship between P and surface rain intensity R must be established in part empirically, because it depends on the details of the vertical distribution of hydrometeors, which are highly variable and not well-documented on a global basis. However, a simplified atmospheric model may be used to obtain an approximate relationship, which may be subsequently tuned to fit detailed radiative transfer calculations and direction observations.

First we assume a power law relationship between R and the volume extinction coefficient $k_{ext,R}$:

$$k_{ext,R} = \alpha R^\beta \quad \text{Equation 12}$$

where α and β depend on frequency and the assumed raindrop size distribution. If we then assume an effective geometric depth H for the precipitation layer, then the optical depth due to rainfall alone becomes

$$\sigma_R = k_{ext,R} H = \alpha R^\beta H . \quad \text{Equation 13}$$

Additional contributions to total rain cloud optical depth include that due to cloud water path L and ice water path I :

$$\sigma_L = \kappa_{ext,L} L \quad \text{Equation 14}$$

$$\sigma_I = \kappa_{ext,I} I \quad \text{Equation 15}$$

where κ_{ext} represents the mass extinction coefficient for the constituent in question. The total rain cloud optical depth is thus

$$\sigma = \sigma_R + \sigma_L + \sigma_I \quad \text{Equation 16}$$

and the total rain cloud transmittance can be modeled as

$$\tau = e^{-\sigma / \cos \theta} = \exp \left[- \frac{\alpha R^\beta H + \kappa_{ext,L} L + \kappa_{ext,I} I}{\cos \theta} \right] \quad \text{Equation 17}$$

The values of L and I are expected to be statistically correlated with surface rainfall intensity, but there is no unique one-to-one correspondence that is valid for all rain clouds, nor is even an estimated average global relationship available from field data. However, extinction by rainfall is expected to dominate in most rain clouds, except when the rainfall is very shallow or when

snow is reaching the surface without melting. The observed normalized polarization P can therefore be written as

$$P = \tau^\gamma + \delta_p = \exp\left[-\frac{\gamma(\alpha R^\beta H + f(R))}{\cos\theta}\right] + \delta_p \quad \text{Equation 18}$$

where $f(R)$ represents the empirically determined mean relationship between surface rain rate and combined cloud liquid water and ice water optical depths, the coefficients α and β are determined as best-fit values to theoretical calculations for an appropriate raindrop size distribution (e.g., Marshall-Palmer), and H is closely related to the geometric depth of the rain layer, which in turn is usually assumed (in the case of cold-cloud rainfall) to be closely related to the freezing (melting) level height Z_L . The latter is estimated from the temperature profile retrieved by the CMIS Core Module.

The term δ_p is a catch-all for both random and non-random errors and uncertainties arising from model simplifications, statistical variations in the true relationship between I , L , and R and in the corresponding extinction coefficients and other variables, and instrument noise. In order to maximize the retrieval performance of the Ocean Precipitation Module, it is desirable to minimize the mean and variance of δ_p through careful tuning of the simplified model to full radiative transfer calculations as well as actual microwave observations where available. Equally important is a realistic characterization of the maximum expected magnitude of δ_p , as this information will control the maximum discrepancy that will be tolerated between observed and forwarded-calculated P before an adjustment to the retrieved rain rate field is required.

In the version of the rainfall algorithm originally developed by Petty (1994) for the SSM/I, the function $f(R)$ was actually represented by a constant optical depth computed for 0.5 kg/m^2 of cloud liquid water at the frequency in question. The effective rain layer depth H was taken to be equal to the freezing level Z_L . Both of these ad hoc assumptions yielded good performance in recent SSM/I rainfall algorithm inter-comparisons; however, a more sophisticated approach based in part on detailed modeling studies is anticipated for CMIS.

3.4.1.1.2 FOV-averaged P

The previous model for the dependence of P on surface rain rate R does not account for possible variability of the rain rate within a finite field-of-view (FOV). If horizontal variability in the rain cloud structure is not too extreme, then the rain cloud may be regarded as locally plane-

parallel for radiative transfer purposes. In this case, the average polarization \bar{P} observed over a finite field of view is given by

$$\bar{P} = \iint_{FOV} G(x, y) P[R(x, y)] dx dy, \quad \text{Equation 19}$$

where $G(x, y)$ represents the unit-normalized effective antenna gain function (including the effects of temporal averaging) appropriate to the pixel in question.

For the purposes of the retrieval algorithm, the rain rate field $R(x, y)$ is approximated as an horizontal grid of spatially contiguous, rhomboidal retrieval cells, within each of which the rain rate is assumed to be constant. Thus, for the (i, j) th FOV in a given CMIS data swath, the observed FOV-averaged polarization is modeled as

$$\bar{P}_{i,j} = \sum_{k=-M}^M \sum_{l=-N}^N G_{k,l}^i P(R_{k+i,l+j}), \quad \text{Equation 20}$$

where

$$\sum_{k=-M}^M \sum_{l=-N}^N G_{k,l}^i = 1, \quad \text{Equation 21}$$

where i is the position of the pixel in a scan and j is the scan number in the swath. The weighting coefficients G depend on the sizes of the respective retrieval cells and their positions within the FOV. Because the relative geometry of pixels and rain retrieval cells is assumed constant from scan to scan, the coefficient arrays \mathbf{G}^i depends on i but not j . The dimensions of these arrays are $(2M + 1) \times (2N + 1)$, where M is chosen to ensure that all retrieval cells making a non-negligible contribution to the FOV-averaged polarization are included in the summation indicated by Equation 20. Thus, M is small for high-resolution channels and proportionally larger for low-resolution channels.

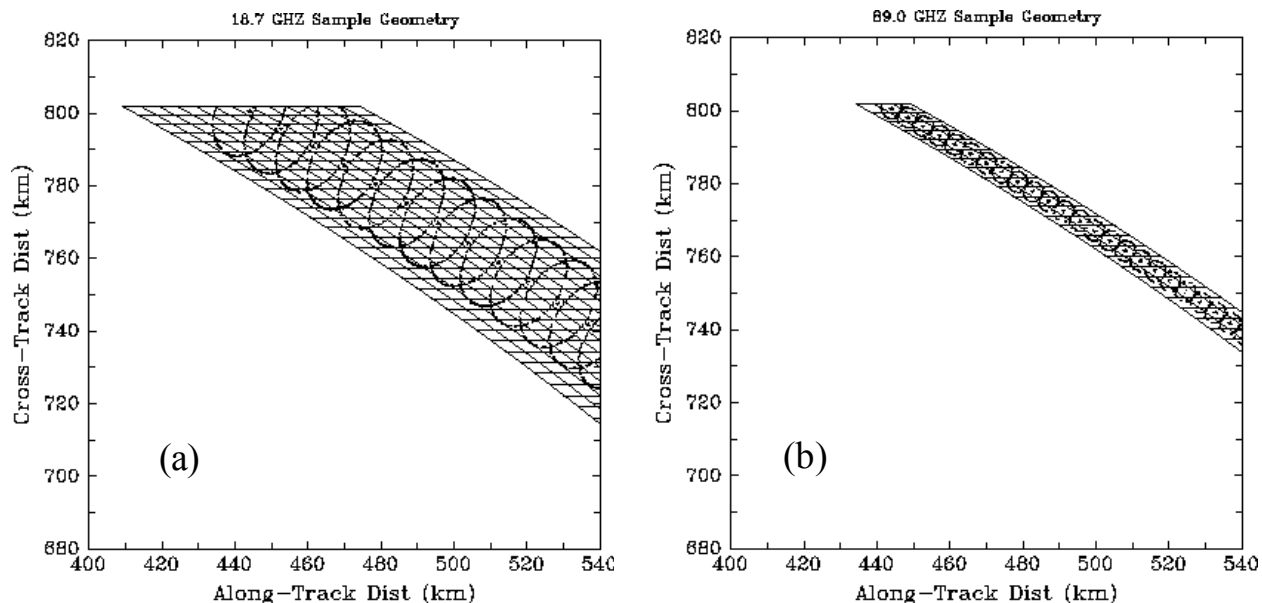


Figure 7: Example of the relationship between rain rate retrieval cells (contiguous parallelograms) and sensor FOVs (ellipses) for a single AMSR scan. a) 18.7 GHz b) 89.0 GHz.

Figure 7 illustrates the relationship between sensor FOVs and rain rate retrieval cells for two channels of a current generation sensor, the Advanced Microwave Scanning Radiometer (AMSR). In this case, the centers of the retrieval cells are chosen to coincide with the centers of the 89 GHz channel FOVs. For CMIS the retrieval grid will be constructed so as to be consistent with the sampling pattern of the 89-GHz brightness temperature CFOV arrays utilized in the rainfall retrieval.

3.4.1.2 Inversion

3.4.1.2.1 Overview

Given a 2-dimensional array of surface rain rates \mathbf{R} , where each element R_{kl} corresponds to an assumed constant rain rate within the k,l th retrieval cell, equations 18 through 20 yield the predicted 2-dimensional polarization field $\hat{\mathbf{P}}$ at a given frequency. Thus, the forward model, while highly simplified in its treatment of radiative transfer through vertical hydrometeor profiles, takes explicit account of the spatial pattern of rainfall within a given FOV.

The objective of the Ocean Precipitation Submodule is thus to find a high-resolution rain rate field \mathbf{R} such that the observed polarization \mathbf{P} field for each frequency utilized in the inversion is consistent with the forward-calculated $\hat{\mathbf{P}}$ to within a specified tolerance ΔP for each pixel. The

tolerance ΔP is carefully chosen for each retrieval frequency to allow for errors associated with the simplified forward radiative transfer model (i.e., the δ_p in Eq. 18), errors due to the simplified treatment of inhomogeneous rainfall (i.e., Eq. 20), and instrument error, which is believed to be a minor contributor to the total error budget. If ΔP is too large for a given CMIS frequency, then the physical information carried by that frequency will have too weak an influence on the final rain rate field. If ΔP is set too small, the retrieval may be overconstrained, leading to instability and, possibly, an inability to find a rain rate field that is simultaneously consistent with all relevant CMIS channels. Because ΔP is designed to allow for significant microphysical and radiative transfer modeling uncertainties, which by definition cannot be quantified a priori, the optimal value of ΔP for each channel must ultimately be determined based in part on experience with actual retrievals.

The actual inversion algorithm takes the following general form:

1. For each rain rate retrieval cell, determine whether or not precipitation *may* be present. Cells deemed unlikely to contain significant precipitation are permanently initialized to zero rain rate and cannot be subsequently modified. The purpose of this step is to help constrain the retrieved rain rate field in cases of partial FOV-filling and to reduce unnecessary computational effort in the inversion.
2. For retrieval cells in which non-zero precipitation is possible, initialize the rain rate to a first-guess value R_0 .
3. For the n th CMIS frequency utilized in the inversion, forward-calculate the polarization field from the current-guess rain rate field.
4. For each pixel in which the difference between the actual and calculated P exceeds the specified threshold ΔP , adjust the relevant rain rate values in a manner which reduces the difference.
5. Repeat steps 3 and 4 for each CMIS frequency utilized in the inversion.

6. Repeat steps 3 through 5 until no pixel violates the consistency threshold ΔP or else the maximum allowed number of iterations has been executed.

The following subsections elaborate on each of these steps.

3.4.1.2.2 No-rain/possible-rain mask

There is a one-to-one relationship between the rain rate retrieval cells and CMIS 89-GHz CFOV pixels. At this frequency, even shallow light rainfall is relatively opaque; therefore, a relatively large value of P effectively precludes the presence of significant precipitation at that location. Furthermore, the 89 GHz channels have the densest sampling and highest resolution of any of the CMIS window frequencies. Thus, the 89 GHz channels are ideal for defining both the geometry of the retrieval grid and the likely presence or absence of precipitation in each cell.

Specifically, a retrieval cell is flagged as containing no rain if the corresponding value of P_{89} is not inconsistent with non-precipitating column cloud water content in excess of 0.5 kg/m^2 . When precipitating ice is present, this criterion can fail because of the polarizing effect of oriented ice particles. However, the presence of such particles is invariably associated with significant scattering of microwave radiation at 89 GHz, which is readily detected via the S parameter defined by Petty (1994a,b):

$$S \equiv PT_{BV0} + (1 - P)T_C - T_{BV} \quad \text{Equation 22}$$

Therefore, an additional criterion for flagging a pixel as containing “possible rain” is the condition that $S_{89} > S_{89,min}$. The latter threshold is chosen large enough to exclude background noise outside of precipitation. For the SSM/I at 85.5 GHz, a threshold of 15 K worked well.

3.4.1.2.3 First guess rain rate

The rain rate field can theoretically be initialized to any reasonable value between 0 and ~50 mm/hr, since it will be subsequently modified to eliminate inconsistencies between forward-calculated and observed P at each frequency. There are two reasons, however, to try to choose the first guess rain rate in each retrieval cell in a less arbitrary fashion:

- *Efficiency*: The closer the initial guess is to the true rain rate, the fewer the iterations required in order to achieve convergence.
- *Additional information at high rain rates*: At high rain rate values, all channels used in the inversion procedure may saturate, in which case the first guess rain rate cannot be modified

based on the information in those channels. In this case, the first guess value is also the final value.

- *Additional information in shallow or frozen precipitation:* When the melting level is at a very low altitude, the depth of the liquid precipitation layer may be very shallow to non-existent. Under these conditions, the precipitating cloud will often be relatively transparent to surface emission, in which case the polarization signature of the precipitation may be smaller than the tolerance ΔP . The algorithm then cannot distinguish between zero precipitation rate and relatively high precipitation rate based on the observed value of P alone. Using scattering information as well (see below) allows a non-zero estimate of precipitation rate to be made based on the presence of frozen hydrometeors.

The first guess rain rate R_0 is thus specified based on the intensity of scattering at 89 GHz, as indicated by the scattering index S_{89} (see definition above):

$$R_0 = \frac{S_{89}}{S_R} \quad \text{Equation 23}$$

where the parameter S_R is chosen empirically and is approximately 4 K per (mm/hr) for the 85.5 GHz channels of the SSM/I. A similar value is expected for the 89 GHz channels of CMIS.

Note that this is the sole point in the algorithm in which scattering information is utilized in the rain rate retrieval. Therefore the first guess is completely independent of the subsequent physical inversion stage.

3.4.1.2.4 Rain rate modification

The overall objective of each iteration during the physical inversion stage is to efficiently eliminate excessive inconsistencies between forward-calculated and observed normalized polarizations while minimizing the disturbance of rain rate estimates that are already consistent with the observations. Thus, the following general principles apply:

- No modification to the rain rate in a given retrieval cell is undertaken if the observed polarization discrepancy $|\hat{P} - P_{observed}|$ is less than ΔP for all pixels overlapping that retrieval cell.

- Where modifications are necessary, the target for new forward-calculated polarization is $P_{target} = P_{observed} \pm \frac{2}{3} \Delta P$, where the choice of sign yields the value of P_{target} nearest to the last forward-computed polarization \hat{P} .
- The degree of modification to the rain rate in the j th retrieval cell is proportional to the sensitivity $\partial \hat{P} / \partial R_j$ of the forward-calculated polarization to changes in the rain rate in that cell. This prevents changes from being made where they would have no effect (e.g., outside of the FOV or in optically thick rainfall) and maximizes changes where they would have the greatest effect. This is, in effect, a multidimensional gradient descent algorithm, with modifications to prevent the appearance of non-physical negative rain rates and to limit the maximum change in any one iteration.
- The total adjustment to all rain rates influencing a given pixel during a single iteration is computed so as to efficiently shift the forward-calculated P toward P_{target} , based on a linearization of Equation 18 with respect to ΔR .
- Because adjacent fields-of-view may significantly overlap and therefore contain redundant information, the actual magnitude of the change in R due to a single FOV is reduced by an effective overlap factor, so that retrieval cells “shared” between two or more FOVs are not over-corrected.

3.4.2. Land algorithm

For the land precipitation algorithm, a statistical algorithm is trained on radiative transfer simulations for a variety of rain cloud properties and surface types. Because of the many degrees of variability in rain cloud scenes over land, as well as the potential non-linearity associated with the use of surface-blind sounding channels, a neural network approach is envisaged:

$$R = f(\Delta \vec{T}_B) \quad \text{Equation 24}$$

where $f(\)$ represents the trained network and $\Delta \vec{T}_B$ is a vector of multi-channel brightness temperature anomalies relative to the precipitation-free background emission, as estimated by the CMIS Core module.

3.4.2.1 Neural-Net Description

The neural-net (NN) used to perform the retrievals consists of a two-layer network (Figure 8) which uses all of the useful CMIS channels (27). (See [EN #13](#).) The transfer function for the

first layer is a sigmoid with 27 inputs and 3 neurons (three outputs). The second layer is linear and contains 1, 2 or 3 outputs, depending on the combination of parameters to be retrieved (IWP, LWP, RR). These functions are described as: $\text{sigmoid}(x)=1/(1+\exp(-x))$ and $\text{purelin}(x)=x$.

Prior to training the algorithm the training dataset was pre-processed with the aim of regularizing it by preprocessing the brightness temperatures (TBs) using the min-max method so that they are within the range $[-1,1]$ and the outputs are also regularized the same way. This has the advantage of minimizing the risk of over-fitting. The training method (i.e., computation of the weights and biases) is based on Levenberg-Marquardt's method. An independent dataset was also used in order to test the resulting neural-net.

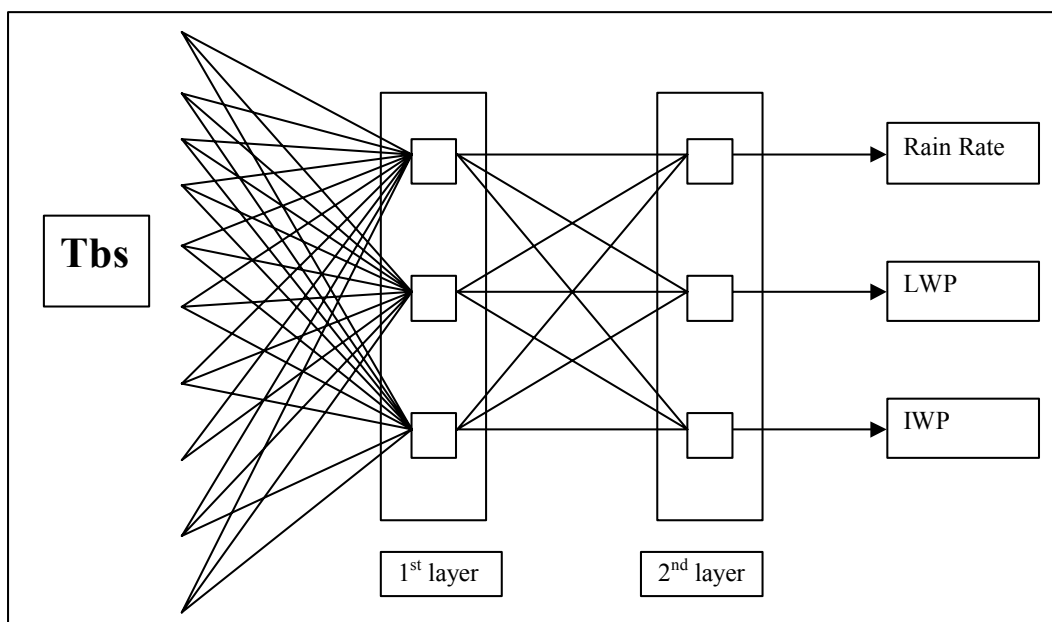


Figure 8: Organization of neural-net algorithm aiming at the simultaneous retrieval of the rain rate, total liquid water path (LWP) and the ice water path (IWP).

3.4.2.1.1 Data for Training Operational Neural-Net Algorithm

Several considerations lead to the conclusion that the neural-net (NN) should be trained using model data rather than measured data (“real data”). First, real data are not representative of global conditions as they are acquired at a single point in time for a single geographical location. The collection of an extensive amount of field data is both time consuming and very expensive. While data from previous campaigns may be used to develop a truth database, care must be taken to ensure that this data is on the proper spatial scales for use by the CMIS algorithm. Model

data, however, can be representative of the large range of conditions to be observed by the operational sensor, and can be tuned to real data from various field campaigns. Thus real data will be used to refine the model data for extreme situations. Another consideration for the use of model data is that training the algorithm using only real data will prevent the algorithm from working right after launch, as time is needed to collect a sufficient amount of co-located satellite and truth (field) data. Further, training the cloud models with real data is limited because there is not enough truth data for the detailed cloud microphysics (particle shape, size distribution, etc.), but one can always generate these parameters randomly using model data in order to span the range of possibilities.

3.4.3. Precipitation Type (Land and Ocean)

The preliminary algorithm for precipitation classification is based on a simple threshold method: If the estimated atmospheric freezing level Z_L above ground level in the vicinity of precipitation, as derived from the CMIS Core module, is less than a threshold $Z_{L,snow}$, then the precipitation is classified as frozen, otherwise it is liquid. The optimal value of $Z_{L,snow}$ requires further investigation but is currently taken as 0.5 km.

3.5. Comments on the Uniqueness of the Solution

Different physically admissible atmospheric states (EDR values) may map to effectively identical microwave multi-channel radiances. To illustrate this problem of uniqueness, two geophysical cases were examined. The spatial characteristics (integrated path amounts) are shown in Table 5 with the vertical profiles shown in Figure 9. The resulting computation of the satellite-observed microwave spectrum is shown in Figure 10. It is clear that it would be very difficult to separate these two profiles given only the radiances. However, not all physically admissible atmospheric states are equally likely. Therefore, given the correct *a priori* statistical distribution of candidate atmospheric states and a perfect forward radiative transfer model (i.e. one that correctly maps a given atmospheric state to its associated microwave observation vector), then, by Bayes Theorem, any given microwave observation vector defines a narrowed point-distribution-function of candidate solutions, from which the maximum likelihood solution and the error covariance may be derived.

In practice the *a priori* statistical distribution of atmospheric states in precipitating cloud systems is poorly known from existing observations. Examples of variables which are critical in mapping EDR variables to microwave radiances, but which are poorly documented on a global

basis, include the spatial and temporal variability of hydrometeor sizes, shapes, phases, concentrations, and particle densities. Two solutions exist which could rectify these problems: (1) a massive field observation program, or (2) the use of cloud models to generate *a priori* statistics. However, field campaigns can obtain only a few variables for a limited set of cases and conditions in order to be cost-effective, while models predict only some of the variables required, and different models yield different results. Further, model validation itself requires extensive field campaigns. Even if *a priori* statistical distributions of hydrometeor mixing ratios and other key rain cloud properties were reasonably well determined, practical microwave radiative transfer models must employ numerous approximations and assumptions, many of doubtful validity (e.g. the assumption of simple plane-parallel geometry despite complex 3-D cloud structure).

The retrieval of rain rate, IWP, and LWP in rain clouds from microwave radiances entails considerable physical ambiguity, even under highly constrained conditions. The ambiguities are exacerbated by a lack of credible statistical constraints on key micro- and macro-physical properties of real rain clouds in different environments. Additional uncertainties arise from the highly simplistic models currently used for extinction and scattering by most ice particle types. Thus greatly improved statistical, microphysical, and microwave optical models of rain clouds are needed both to mitigate the physical ambiguities and in order to derive credible estimates of global algorithm performance.

Parameter	Case 1	Case 2
Cloud Liquid Water Path (CLWP)	0.58	2.30
Rain Water Path (RWP)	1.68	1.44
Graupel Water Path (GWP)	2.36	0.21
Snow Water Path (SWP)	0.66	0.65
Liquid Water Path (LWP = CLWP + RWP)	2.26	3.74
Ice Water Path (IWP = GWP + SWP)	3.02	0.85
Total Water (TWP = LWP + IWP)	5.28	4.60
Rain Rate (RR)	8.0	6.1

Table 5: Rain cloud parameters used to show radiometric ambiguity.

ALGORITHM DESCRIPTION

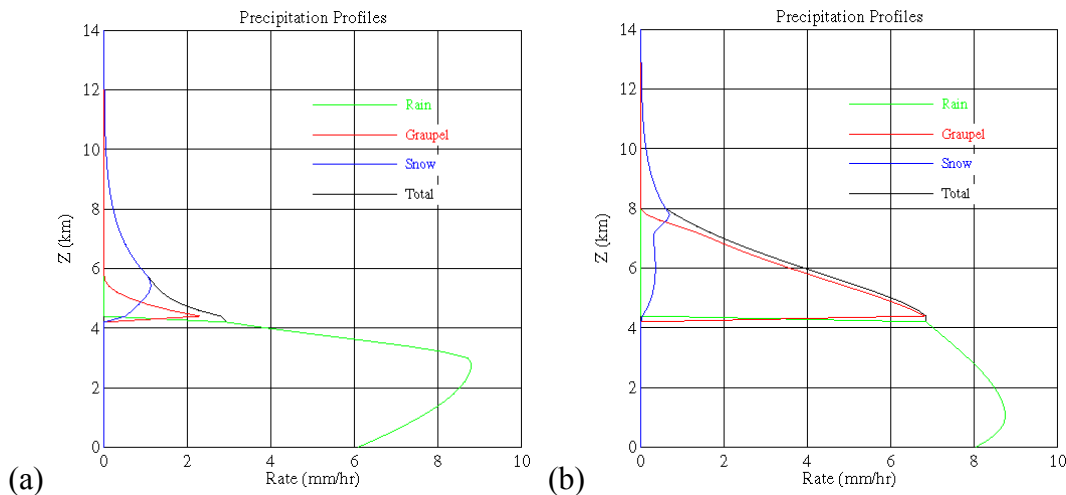


Figure 9: Vertical distributions of horizontally uniform precipitation. The surface rain rates are (a) 8.0 mm/hour and (b) 6.1 mm/hour.

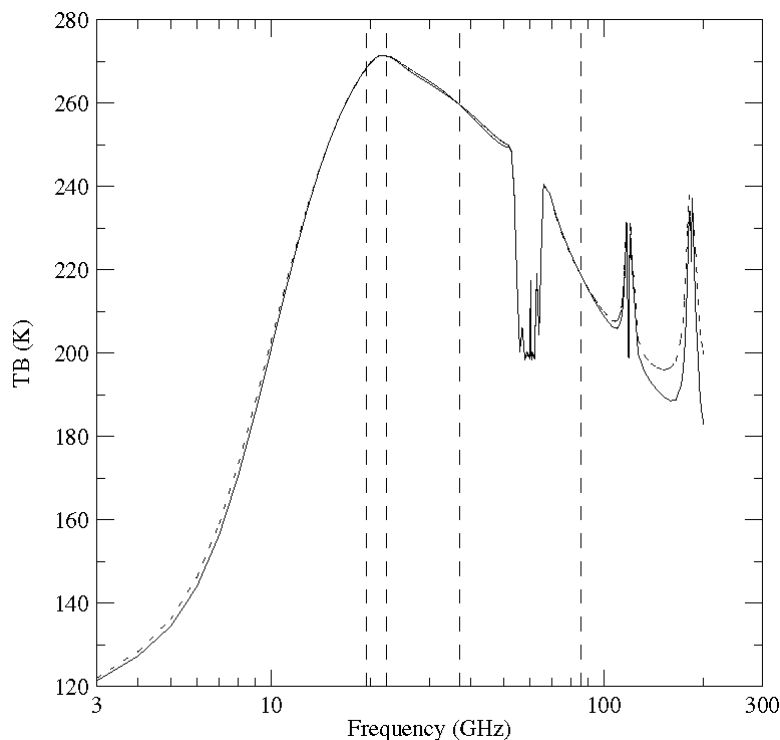


Figure 10: Satellite-observed microwave spectrum for the two precipitation cases described in Table 5 and shown in Figure 9.

3.6. Algorithm Performance

There are three basic approaches that can be utilized to estimate algorithm performance:

1. *Empirical comparison of algorithm results with ground “truth” data.* This is of course impossible with sensors that have not yet been launched. Furthermore, the scarcity of

validation data of sufficient quality and diversity remains a major challenge for validation of rain rates, especially over ocean and unpopulated land areas. Nevertheless, some insight may be gained from the comparative empirical performance of passive microwave algorithms applied to data from earlier sensors, such as the SSM/I.

2. *Simulated retrievals using synthetic satellite data derived from cloud models and radiative transfer models.* This is the preferred approach with new sensors and algorithms. However, it is important to be aware of the impossibility (according to the current state of the art) of credibly reproducing either the global statistical distribution of rain cloud properties or the detailed physics of the interaction of rain clouds with microwave radiation using models alone. Therefore, performance statistics derived from simulations are primarily of qualitative value, e.g., for assessing the role of spatial inhomogeneity, etc., in algorithm performance.
3. *Error budget analysis applied to the algorithm and modeled input brightness temperatures.* This is currently impractical for precipitation retrievals, owing to the very large number of variables that would have to be considered, along with our inability to even guess at the global uncertainties or range of variability associated with many of these variables. The highly non-linear nature of retrieval problem also reduces the usefulness of conventional error budget analysis, since one cannot assume that the cumulative effects of different types of errors combine in a predictable way.

Subsequent sections address each of the first two of the above methods. It must be emphasized that these results are preliminary and regionally limited and that credible, detailed, *global* performance estimates of passive microwave precipitation retrievals remain well beyond the current state of the art. Furthermore, it must be emphasized that raw performance statistics for a single algorithm considered in isolation are nearly meaningless, as these statistics may span a very broad range, depending on the conditions to which the algorithm is subjected. We therefore strongly advocate a focus on the *comparative* performance of competing retrieval strategies applied to identical data sets, whether real or simulated.

3.6.1. Algorithm Performance Over Ocean

3.6.1.1 Empirical Results from SSM/I Algorithm Intercomparisons

Rain rate retrieval results derived using the algorithm of Petty (1995b) applied to SSM/I data were compared with results from other SSM/I algorithms in two recent major intercomparison projects. The first of these, the GPCP's Algorithm 3d Intercomparison Project (AIP-3), validated over-water rain rate retrievals from a large number of algorithms against instantaneous ship-

based radar rain rate estimates over a three month period in the Western Tropical Pacific. Although there remain questions concerning the absolute calibration of the radar rain rates in this exercise, the space-time correlations of the satellite products with the radar instantaneous rain rate fields are believed to provide a meaningful basis for comparing the ability of different algorithms to reproduce patterns of rainfall at 0.5 degree spatial resolution under tropical conditions. The algorithm of Petty (1995b; identified as ‘PE1’ in Figure 11) yielded a significantly greater space-time correlation ($r=0.78$) than any of the other 28 SSM/I algorithms submitted to AIP-3.

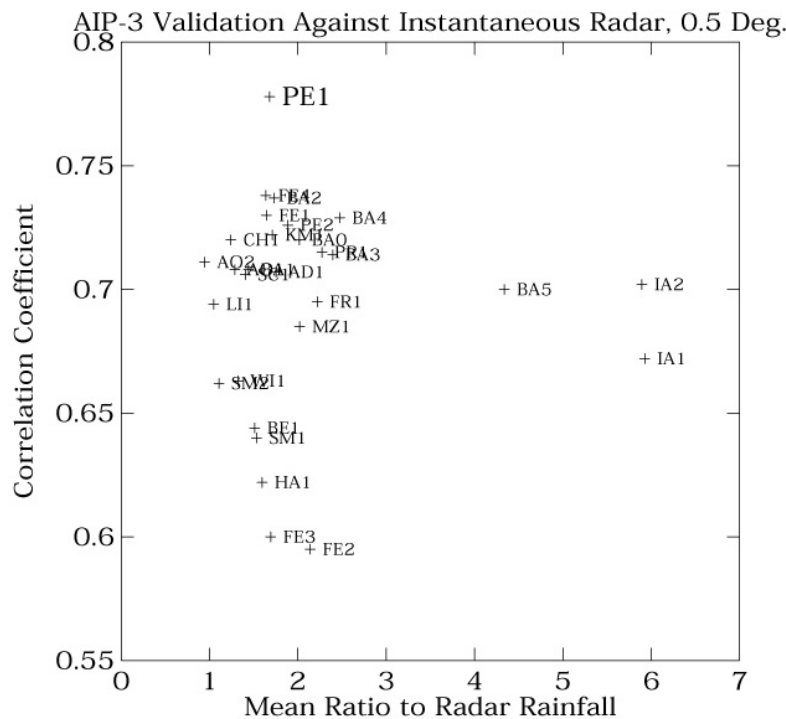


Figure 11: Selected validation statistics for SSM/I algorithms submitted to the 3d Algorithm Intercomparison Project (AIP-3). The Petty (1995b) algorithm is identified by “PE1”. The mean ratio of satellite to radar rainfall is of questionable absolute value owing to concerns about the absolute calibration of the radar rain rates.

A subsequent intercomparison, the 3D Precipitation Intercomparison Project (PIP-3) focused on validation of global monthly rainfall retrievals. Over water, there were only two available validation data sources: (1) a ship-derived climatology of the statistical frequency (not amount) of precipitation (Petty 1995a; Petty 1997), and (2) a few surface rain gauges on small tropical atolls in the tropical Pacific ocean. The first data type was useful for evaluating the qualitative

reasonableness of satellite-derived patterns of rainfall occurrence, while the second was useful for evaluating the calibration of the retrieved rain amounts in the deep tropics only. Both statistics for the 12-month intercomparison period are displayed for all competing SSM/I algorithms in Figure 12. The Petty (1994b) algorithm is identified here as “pur”. This algorithm again achieved the highest overall space-time correlation of ocean rainfall patterns with the ship-derived climatology of fractional-time-raining (FTR), and the second-lowest RMS difference from monthly atoll gauge totals. Furthermore, it excelled at capturing the seasonal cycle in precipitation occurrence (see Adler et al. 2001), unlike many of its competitors.

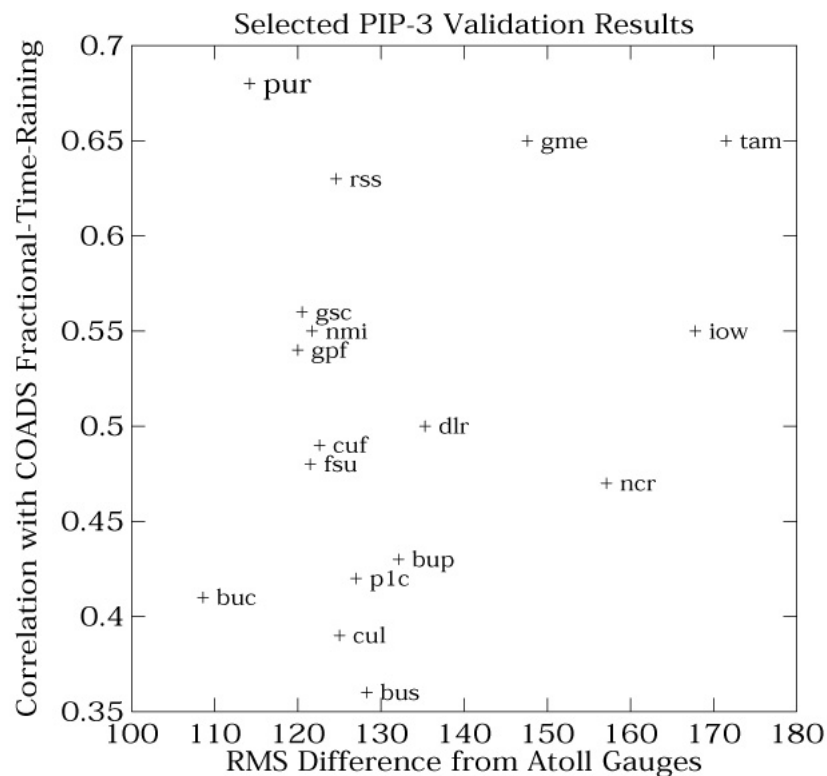


Figure 12: Selected validation statistics taken from PIP-3. The Petty (1994b) algorithm is identified as “pur”.

Although these results do not allow detailed quantitative statements to be made about algorithm performance under varied conditions (in part owing to limitations in the validation data themselves), they nevertheless lend strong credibility to the retrieval strategy chosen for CMIS. In view of the CMIS improvements in spatial resolution and channel diversity, there is every reason to expect that results from this algorithm will be better still than those obtained for the SSM/I.

3.6.1.2 Performance Based On Simulated Retrievals

As noted earlier, performance estimates based on simulated retrievals are subject to numerous caveats, many of these connected with the many known imperfections and errors in both the atmospheric models and the radiative transfer codes. Nevertheless, we have recently undertaken the first known end-to-end simulated passive microwave retrievals using a full 3-D radiative transfer code applied to output from a mesoscale numerical forecast, with realistic sampling and FOV-averaging designed to mimic the characteristics of the CMIS sensor. The analysis entailed the following series of steps, with the results from one step feeding into the next:

1. Simulation of an extratropical frontal rainband using the MM5 community mesoscale model.

The scene in question includes a narrow convective band embedded in widespread stratiform rain. The freezing level varies from 1-2 km in the warm sector to near-surface in the cold sector. In the latter case, precipitation reaching the surface arrives as a mixture of rain and graupel. The horizontal model resolution is 3 km and the domain size is 198 x 198 km. Two different microphysical parameterizations are available in the MM5, each producing very different hydrometeor and rainfall patterns. We used the parameterization of Tao and Simpson (1993) for this simulation. The model output included 3-D distributions of hydrometeor concentrations in 5 categories: rain, graupel, snow, ice, and cloud water. Surface precipitation rates were estimated (for validation purposes) by applying a fall-speed model to the hydrometeor concentrations in the lowest layer of the model domain. Model output was saved at hourly intervals, covering a 24-hour period. Only the results in the last few hours of the simulation were utilized in order to exclude the precipitation “spin-up” time following model initialization.

A notable peculiarity of the simulation results was the occurrence of unrealistically intense surface precipitation rates (in the form of graupel) of up to 250 mm/hr within a few grid boxes. In reality, precipitation rates in excess of 150 mm/hr are rarely observed even in the tropics, and maximum precipitation rates are typically far less still in cold-season cloud systems. This anomaly highlights the difficulty of achieving realism in 3-D rain cloud structures, even using a thoroughly tested and widely used community model like the MM5.

2. Conversion of MM5 hydrometeor output fields to 3-D fields of microwave optical properties.

To accomplish this step, it was necessary to specify an ad hoc relationship between the concentration of hydrometeor mass in each category and the particle size distribution (parameterized here via the exponential slope parameter Λ). For raindrops, the Marshall-Palmer

relationship was utilized. For other hydrometeor types, such as graupel and snow, other exponential relationships were utilized, following the general approach described by Petty (2001b). Once the liquid-equivalent size distribution was specified, it was further necessary to specify effective particle densities (ice-air ratios) and choose one of three possible formulas for the effective dielectric constant of a two-component mixture. We arbitrarily chose the Bruggeman formula. Mie theory (which assumes homogeneous spherical particles) was then utilized to calculate the combined contributions of all hydrometeors to the volume extinction coefficient, single-scatter albedo, and scattering asymmetry parameter in each model grid box.

3. Three-dimensional radiative transfer simulations using a Backward Monte Carlo model. The above 3-D optical properties were input into an updated version of the radiative transfer code described briefly by Petty (1994a). The widely-used Henyey-Greenstein analytic phase function was assumed (known to be sub-optimal for describing microwave scattering, but the only reasonably practical option available). The ocean surface was modeled as a Fresnel surface with appropriate microwave dielectric constant for seawater. The simulation domain was treated as periodic for radiative transfer purposes. The model utilized a simplified scalar treatment of polarization effects due to the ocean surface, as described in Section 4.3. Simulated microwave imagery was produced at 1 km resolution, so as to resolve possible effects of rain cloud 3-D geometry on brightness temperatures. These forward radiative transfer calculations were undertaken for 5 different model time steps, 2 assumptions concerning ice particle size, 5 frequencies, and with/without condensed water mass (in order to establish “cloud-free” brightness temperature fields for computing the transformed brightness temperature variables P and S), for a total of 100 distinct simulations.

4. Remapping of high-resolution TB fields and MM5 surface rain rate fields to CMIS swaths. Gaussian weighting functions with appropriate half-power widths were used to represent the effective fields-of-view. The 198 km model domain from the MM5/radiative transfer model was replicated periodically to fill the entire 1700 km swath of the CMIS. This ensures that performance results will include the effects of varying scan and retrieval grid geometry across the swath (sampling density is higher at the edges than at the center of the swath).

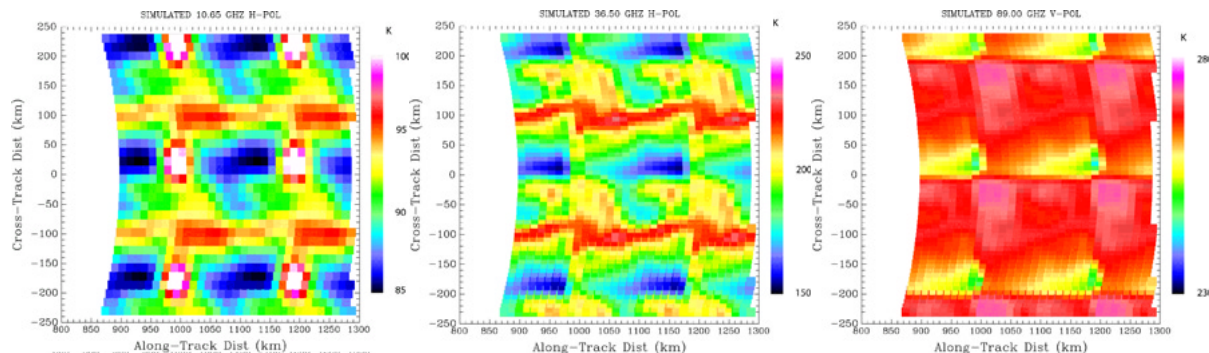


Figure 13: Simulated CMIS brightness temperature swath data from one time step of the MM5 model run. Only the middle of the swath is shown here. Note the absence of strong scattering at 89 GHz (right panel) despite the presence of large surface precipitation rates at some locations in the model domain. The lack of an apparent scattering signature appears to be due to very large amounts of cloud liquid water produced by the model at locations where graupel is also produced.

5. *Execution of retrieval algorithm on simulated CMIS swaths.* The algorithm was used to retrieve surface rain rate patterns at a resolution of 7.5 x 12.5 km (at swath center; higher at edges). Retrieval results, along with the MM5-derived “validation” rain rates, were averaged down to nominal 15x15 km reporting cells for comparison purposes. Note that a number of variables, such as the choice of retrieval channels, the number of iterations, and the choice of “first guess” rain rate field, all affect the details of the retrieved rain rate field. We have not yet attempted to optimize these choices, but simply chose the 10, 18, and 36 GHz channels for the retrieval, with the first-guess rain rate set to zero. A large number of iterations (100) was allowed in order to ensure maximum convergence.

ALGORITHM DESCRIPTION

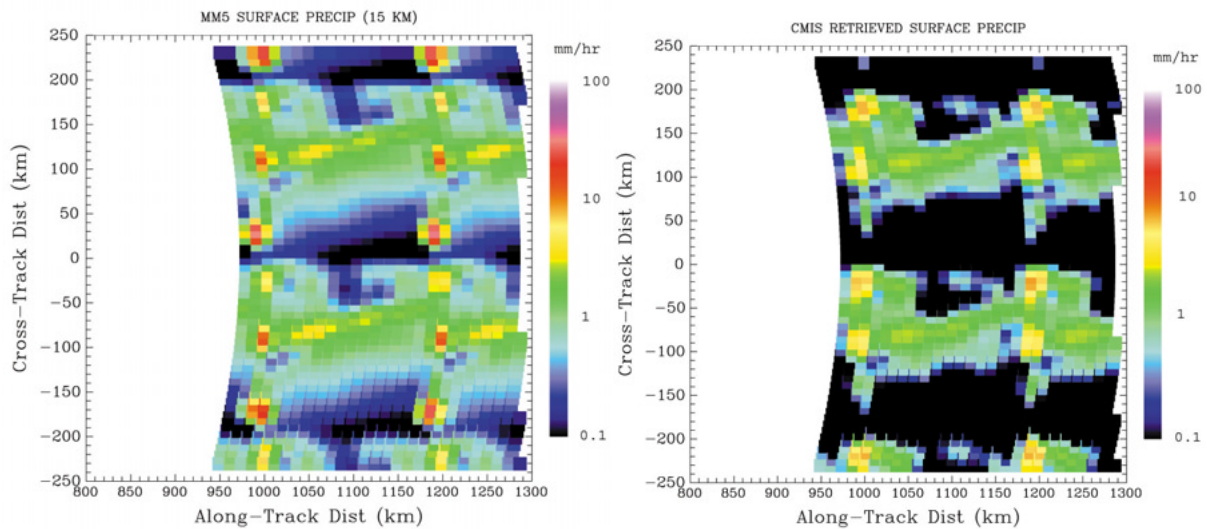


Figure 14: Comparison of “actual” (left) and “retrieved” (right) surface rain rate fields, after averaging of both to 15 km resolution. Note logarithmic color scale spanning three orders of magnitude. Rain rates below approximately 0.3 mm/hr were below the sensitivity threshold of the CMIS retrieval algorithm. Also, instances of very high surface precipitation rate in the model-generated rain rate field are highly localized and could not be resolved by the retrieval algorithm.

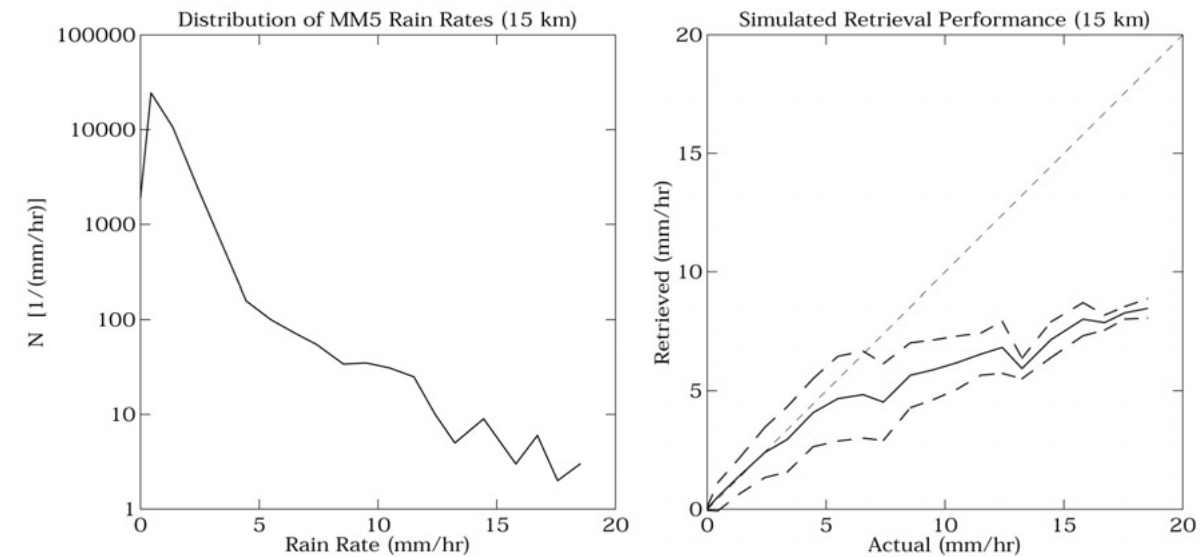


Figure 15: Results of simulated retrievals. Left panel: Distribution of “actual” rain rates in MM5 simulation, at 15 km resolution. Rain rates in excess of 5 mm/hr were rare and highly localized. Right panel: Retrieved vs. “actual” rain rates. Solid line represents the average of the retrievals for each 1 mm/hr “actual” rain rate bin. Dashed lines indicated the standard deviation above and below the mean. Note that retrieval accuracy and precision are very good below 5 mm/hr. At localized higher rain rates, a systematic underestimate occurs because of “smearing” of the retrieved rain rate over a larger area than that occupied by the actual rain cells.

3.6.2. Algorithm Performance Over Land

3.6.2.1 Database Used for Determining Algorithm Performance Over Land

In order to efficiently train the neural network, one needs to have a comprehensive, and yet representative, geophysical database. The non-scattering atmospheric parameters (i.e., the temperature and water vapor profiles) were picked from the NOAA-88 database. A total of 200 profiles were selected. The land surface temperature is also provided by the NOAA-88 dataset. The land surface emissivity is selected randomly from Prigent’s database. The original SSM/I emissivity values of Prigent (1999) are interpolated and extrapolated to the CMIS frequencies. Two databases are created, one with only snow and ice land emissivity types, and the other without any snow or ice. The former is representative of winter conditions a from mid-latitudes to the poles, while the other is primarily of use in the tropics. Further, two sets of these databases are created, one for training the algorithm and the other for validation.

Twenty random hydrometeor profiles were associated to each of the 200 NOAA-88 profiles, thus producing 4000 cases. These hydrometeor profiles consist of liquid and frozen rain-rate profiles, and a cloud liquid water profile. As described in more detail below, these hydrometeors were generated following the scheme Kummerow and Giglio (1994) used for their uniqueness study. Essentially, the RR is selected at random within the required range. The value of RR fixes the range of cloud liquid water (CLW) and frozen precipitation in the first layer. The concentration of each constituent in the first layer determines the range of concentrations in the layers above.

3.6.2.1.1 Heritage of Hydrometeor Database

Kummerow and Giglio (1994) developed a rainfall rate retrieval algorithm based upon statistical inversion techniques. This algorithm takes into account the vertical distribution of the hydrometeor profiles using a limited set of cloud vertical profiles covering a wide range of likely raining conditions. The cloud structures consisted of five vertical layers defining the vertical hydrometeor profiles. The database was constructed by selecting a limited number of cloud structures (27) and then adding variability to these structures by randomly generating the parameters of interest (rain rate, surface parameters and fractional beam filling). A plane-parallel multiple scattering radiative transfer model (RTM) was used to generate the simulated brightness temperatures.

The 27 structures selected by Kummerow and Giglio consisted of 18 convective and 9 stratiform precipitations. To account for different climatic regimes, they took the freezing level is taken between 2 and 4.5 km. Convective structures are defined as those in which a significant amount of liquid water (cloud water, rain drops) exists above the freezing level. The stratiform structures are characterized by the absence of liquid drops above the freezing level. In the retrieval algorithm of Kummerow and Giglio, some preliminary steps are taken prior to performing the actual multichannel retrieval process, with the goal of reducing the number of potential structures to test.

In order not to generate structures unlikely to be observed in nature, some constraints were placed on the hydrometeor profiles (see Figure 16). The model specifies the rain rate, cloud water, and ice precipitation in up to five layers, from the surface to 12.5 km. The surface layer rain rate can vary randomly in the range from 0 to 50 mm/h. Rain rates in successively higher layers decrease and are partially correlated with the layer directly below. Cloud water and ice precipitation in the lowest layers are related to the surface rain rate; as with the rain rate profile,

ALGORITHM DESCRIPTION

values at higher layers are correlated with the values directly below. While completely arbitrary, the authors claim that the resulting cloud structures resemble observed structures and represent a vast array of conceivable, if not realistic vertical structures. The random-but-physically-constrained database used in their study contained only rainy structures (with cloud water, rain and precipitating ice) and lacks cloudy-only (precipitation free) situations. This is because their algorithm pre-processes the cloudy-only structure before starting the actual rainy structure search algorithm.

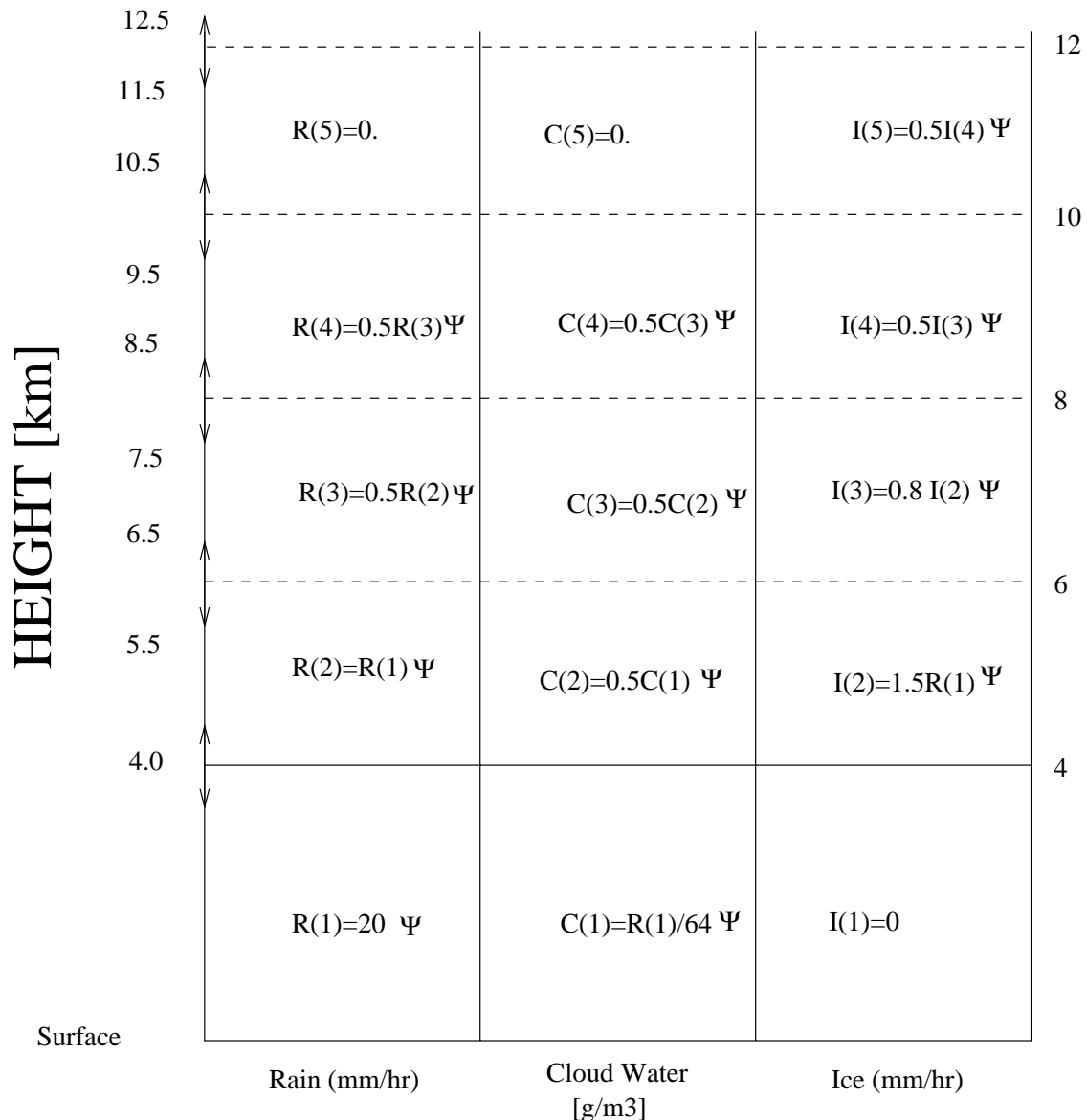


Figure 16: Schematic diagram showing vertical distribution of cloud constituents used for the generation of hydrometeor profiles (Kummerow and Giglio, 1994). The rain-rate (R) is selected randomly within a predetermined range using a random number (Ψ) between 0 and 1. For the case shown here, the RR falls in the range from 0-20.

3.6.2.1.2 Hydrometeor Database Description

We adopted the scheme of Kummerow and Giglio used for their uniqueness study, for the generation of the hydrometeor profiles. We enhanced this scheme with a slight modification to account for cloudy, but rain-free atmospheres by including an additive term in the cloud amount:

$$C(1) = (\Psi/64) * R(1) + (\Psi * 0.1) / (1 + R(1))$$

In this equation C is the cloud amount, Ψ is a random number between 0 and 1, and R is the rain rate. This equation is written to ensure that for non-raining structures there is still the possibility of having non-precipitating clouds. On the other hand, the higher the rain rate, the more negligible the additive term becomes. Table 6 shows the statistics of the different parameters that constitute the training databases.

	CLW (mm)	RWP (mm)	RR (mm/hr)	IWP (mm)	LWP (mm)
Mean	0.86	6.20	25.00	5.04	7.05
Std	0.75	3.40	14.49	3.62	3.90
Range	[0.-3.65]	[0.-15.54]	[0-50]	[0-15]	[0.08-18.58]

Table 6: Atmospheric parameters used for generating the geophysical dataset (ice included). The statistics are shown for the cloud liquid water (CLW), the rain water path (RWP), the surface rainfall rate (RR) and the ice water path (IWP) and the liquid water path (LWP).

In a later paper, just before the launch of the Tropical Rainfall Measuring Mission (TRMM) for which the algorithm was designated, Kummerow et al. (1996) used a different and more sophisticated approach to generate the database. In this approach the hydrometeor profiles came from many realizations of the nonhydrostatic Goddard Cumulus Ensemble (GCE) model, instead of the randomly generated dataset, and the brightness temperatures were computed using a detailed 3D radiative transfer model. Their model, referred as the Goddard Profiling Algorithm (GPROF), is based upon a Bayesian approach and was at that time applicable only to tropical environments due to lack of cloud dynamical model simulations. The conservation equations for two liquid water species (cloud and rain drops) and three ice-phase species (ice, snow and graupel) were included in the formulation. While the main advantage of using dynamic models for the generation of the database is that the microphysical processes are well represented, the

drawback is their limited global applicability. One of the conclusions of the 1996 paper was that the overall performance of GPROF when applied to real SSM/I data was found to be similar to the previous algorithm developed using hypothetical structures, rather than those dynamically derived from the GCE model. This result gives us confidence in the scheme we have adopted for the random generation of the hydrometeor profiles for CMIS performance estimates.

3.6.2.2 Land Performance Results

As stated previously, several combinations of retrieval parameters were tested. The results are given in Table 7 and Table 8. In an attempt to improve the retrieval results, tests were also performed using subsets of the CMIS channels. These simulations were done using a random variation of the surface emissivity for snow- and ice-free conditions. The sensor noise corresponds to that obtained with a spatial resolution of 15 km. A comparison is also made between an algorithm using only the brightness temperatures (Tbs) and an algorithm using the brightness temperature depressions, which are the multi-channel brightness temperature anomalies relative to the precipitation-free background emission (see Section 3.4.2). The results show that the highest precision is obtained using all channels instead of just the sounding-only or window-only channels, with only a minor difference between using Tbs depressions rather than the Tbs themselves. Finally, there is a slight improvement in retrieving the rain rate along with the IWP and LWP.

Detailed performance estimates for land conditions are shown in Figure 17 over the required rain-rate range. However, saturation of the channels occurs for the higher values of rain-rate, thus decreasing the skill of the retrieval. This is seen most clearly in Figure 17 where the scatter plot becomes much more horizontal at about 25 mm/hr. A more reasonable approach, which provides more physically meaningful results, is to determine the retrieval performance for the region where there is retrieval skill. In Figure 18 the performance is calculated only for the low rain-rate cases, and the results are much better.

ALGORITHM DESCRIPTION

(a) Precision (mm/hr) of the RR retrieval algorithm:

	All Channels	Sounding channels	Window channels
Tbs only	9.851	11.248	10.732
Tbs depressions	9.977	11.079	11.298

(b) Accuracy (mm/hr) of the RR retrieval algorithm:

	All Channels	Sounding channels	Window channels
Tbs only	-0.007	-0.221	0.329
Tbs depressions	0.088	-0.574	0.152

(c) Correlation factor of the RR retrieval algorithm:

	All Channels	Sounding channels	Window channels
Tbs only	0.745	0.647	0.686
Tbs depressions	0.737	0.662	0.643

Table 7: (a) Precision, (b) accuracy, and (c) correlation results of the neural-net retrieval of the RR alone.

ALGORITHM DESCRIPTION

(a) Precision (mm/hr) of the RR retrieval algorithm:

	All Channels	Sounding channels	Window channels
Tbs only	9.676	11.333	10.448
Tbs depressions	9.674	10.991	10.329

(b) Accuracy (mm/hr) of the RR retrieval algorithm:

	All Channels	Sounding channels	Window channels
Tbs only	-0.089	-0.207	0.263
Tbs depressions	0.026	-0.575	0.158

(c) Correlation factor of the RR retrieval algorithm:

	All Channels	Sounding channels	Window channels
Tbs only	0.755	0.640	0.706
Tbs depressions	0.755	0.668	0.714

Table 8: (a) Precision, (b) accuracy, and (c) correlation results of the neural-net retrieval of the RR along with IWP and LWP.

ALGORITHM DESCRIPTION

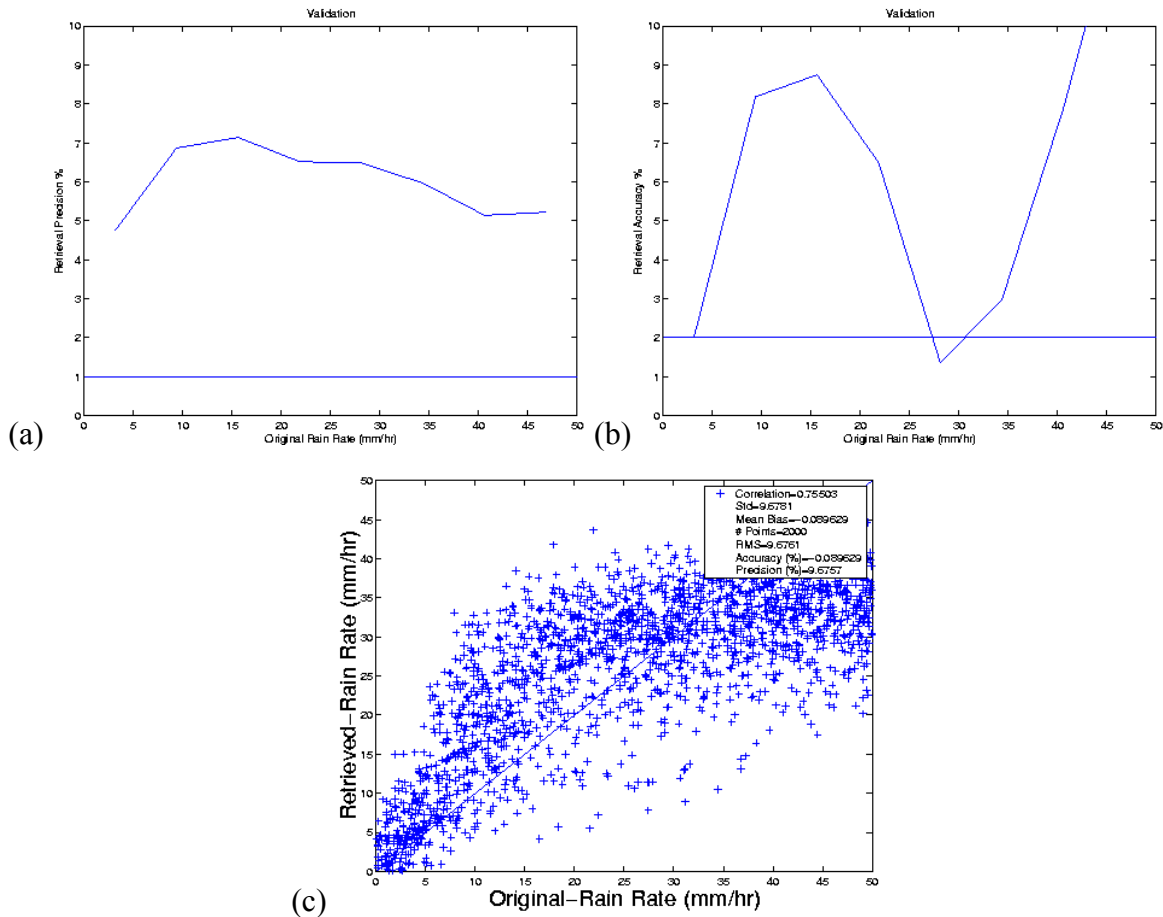


Figure 17: Detailed stratified performance estimates of (a) precision, (b) accuracy, and (c) the scatterplot for the RR retrieval with the simultaneous retrieval of LWP and IWP. This corresponds to the case in Table 8 using the Tbs only for all CMIS channels. The solid horizontal lines correspond to the threshold requirements.

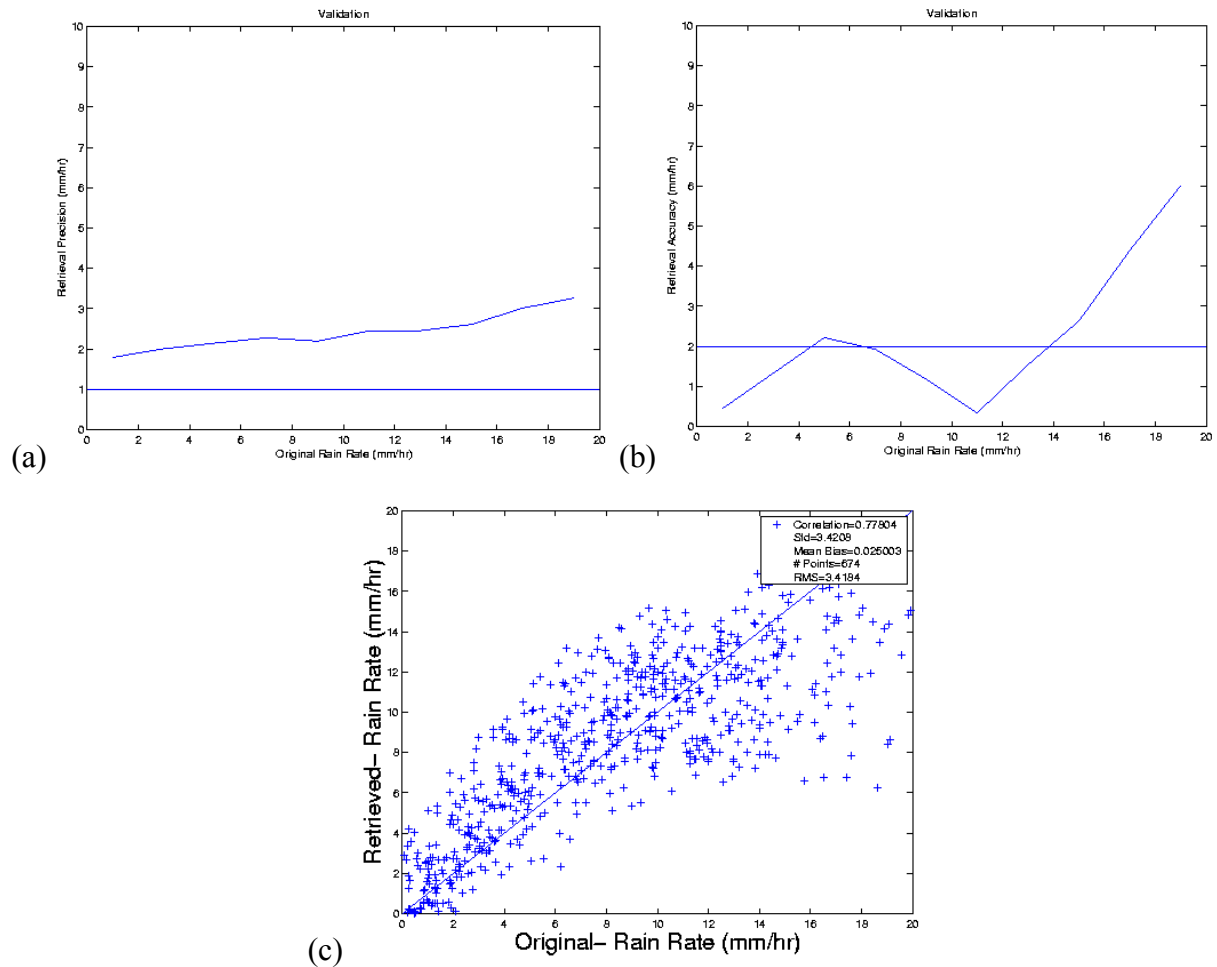


Figure 18: Detailed stratified performance estimates of (a) precision, (b) accuracy, and (c) the scatterplot for the RR retrieval with the simultaneous retrieval of LWP and IWP. This figure is the same as the previous figure except that performance is only calculated for low values of rain-rate.

3.6.2.2.1 Stratification of Performance by Surface Type

For the retrieval results presented above the neural-net was trained on a global set of emissivity types, and the retrievals were performed for a random set of emissivity values. To be sure that these results are representative for a specific emissivity type, the retrievals were also performed on specific emissivity classes, namely “ice” and “snow”. These results are shown in Figure 19 and Figure 20, and are very similar to the results in Figure 17. Thus the set of statistics for the random global emissivity test set are representative of each land surface type when the global set is applied to specific regions.

ALGORITHM DESCRIPTION

The retrieval results presented above do not meet the threshold requirements for the retrieval of rain-rate. However, those tests were conducted using a set of test profiles that included a random set of surface emissivity values. Operationally the algorithm will have access to a dynamic database of surface emissivity, and the retrieval may be constrained to a particular type of emissivity spectrum. Tests will be conducted to evaluate the impact of surface knowledge, as well as misclassification of the emissivity type.

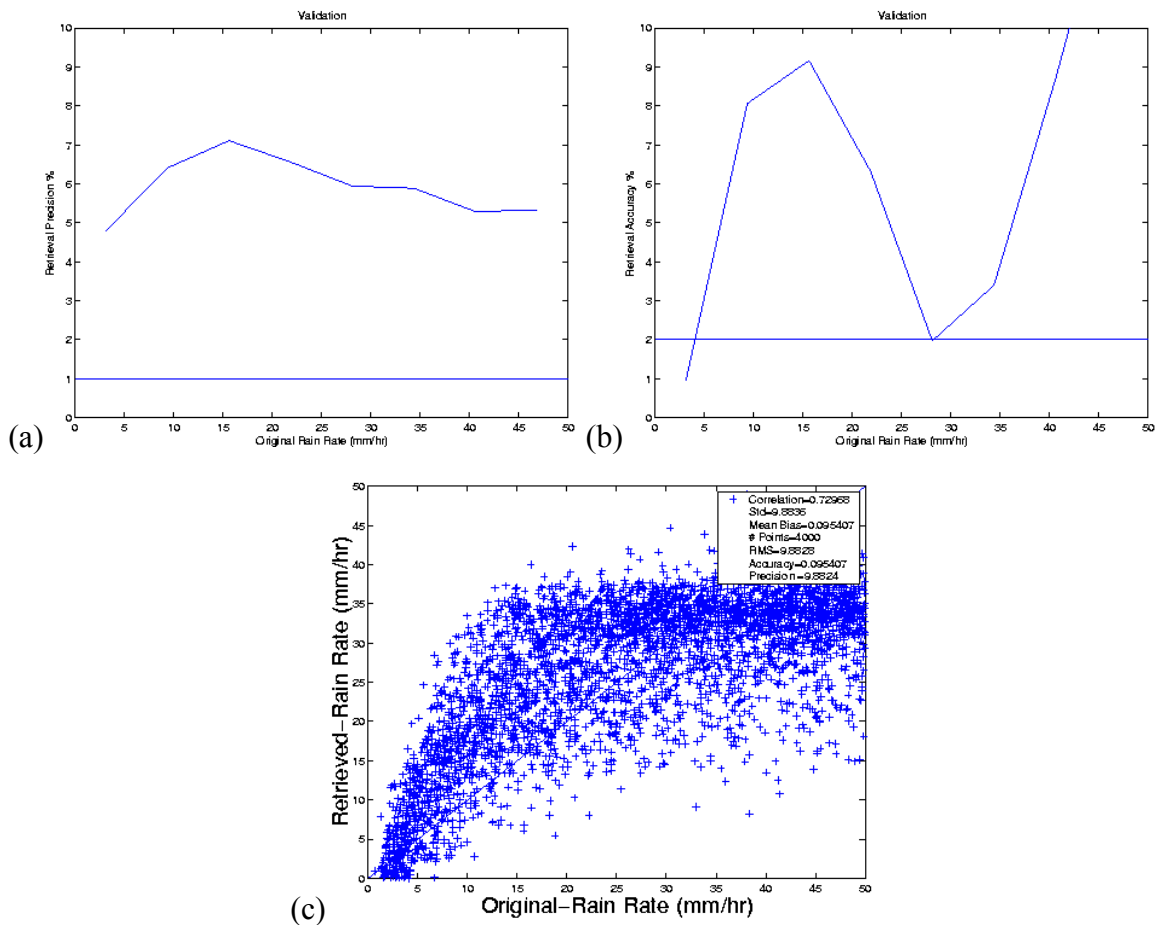


Figure 19: Detailed performance estimates of (a) precision, (b) accuracy, and (c) scatterplot for the RR retrieval with the simultaneous retrieval of LWP and IWP. This corresponds to the emissivity of “ice”. The solid horizontal lines correspond to the threshold requirements.

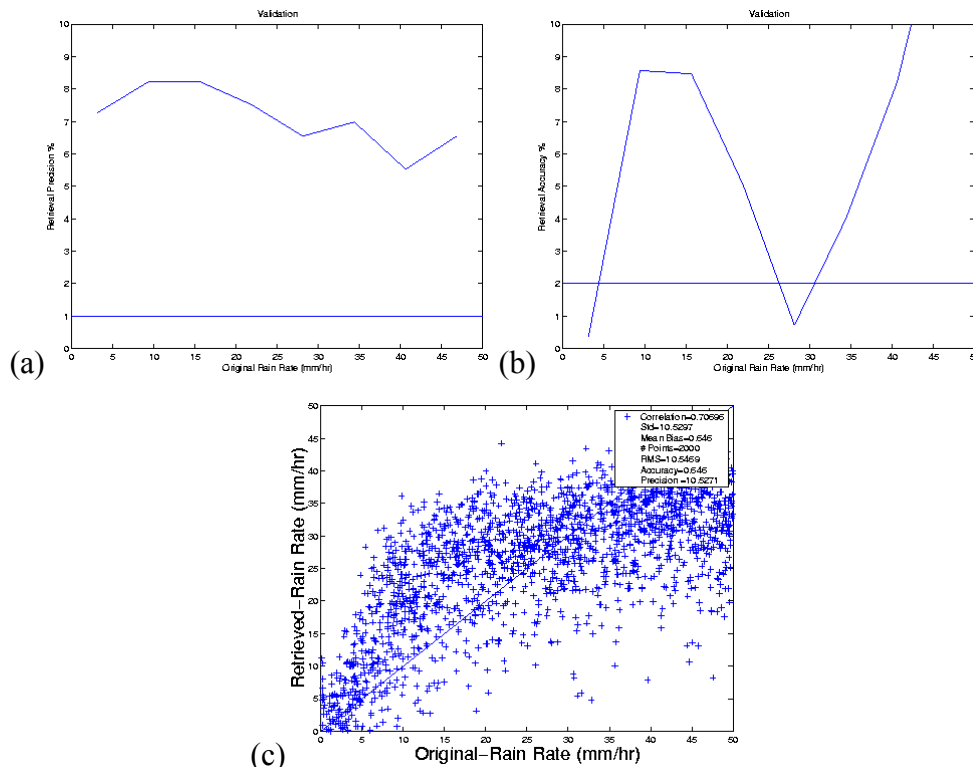


Figure 20: Detailed performance estimates of (a) precision, (b) accuracy, and (c) scatterplot for the RR retrieval with the simultaneous retrieval of LWP and IWP. This corresponds to the emissivity of “snow”.

3.6.3. Limiting Conditions

3.6.3.1 Precipitation Geometry Effects (3-Dimensional Structures)

Of the atmospheric EDRs assigned to CMIS, surface precipitation rate is the variable for which three-dimensional structure is potentially the greatest complicating factor in the design of a retrieval algorithm. Heavily precipitating rain clouds may be optically thick at most microwave wavelengths, and they may exhibit strong horizontal variability on scales comparable to their vertical dimensions. The work presented below was part of a trade study regarding different scan angles of incidence. However, it also pertains to the general phenomenology of how cloud structure will impact the retrieval performance.

Increasing the earth incidence angle of any satellite sensor tends to exaggerate the effects of 3-D geometry, and we therefore expect retrieval performance to degrade at higher incidence, unless the retrieval algorithm explicitly accounts for the expected effects of 3-D geometric and microphysical structure on the observed radiances.

Unfortunately, it is very difficult to make reliable generalizations concerning the three-dimensional geometric and microphysical structure of rain clouds; not only are these properties not yet adequately documented (for remote sensing purposes) in any one cloud type, but they are known to vary dramatically from one climate zone to the next. It is in any case extremely difficult to directly account for 3-D structure effects into retrieval algorithms without incorporating a 3-D radiative transfer model into the algorithm and attempting to explicitly retrieve 3-D fields of hydrometeors. To date, only statistical algorithms using large lookup tables derived from cloud models (e.g., Kummerow et al.) are based on forward calculations from a 3-D model; even these algorithms do not attempt a simultaneous 3-D retrieval of cloud structure. Rather, they simply attempt to find a radiatively-compatible 1-D hydrometeor profile separately for each pixel.

The precipitation algorithm under development for CMIS is unique in performing a 2-D retrieval of surface rain rate, based on a criterion of simultaneous consistency with the observations both in space and across channels, after allowance for the spatial resolution and geophysical sensitivity of each channel. However, even this algorithm cannot be readily modified to account for, or directly retrieve, 3-D rain cloud structure. Like most other algorithms published to date, it relies on a local plane-parallel approximation to microwave radiative transfer, which is equivalent to assuming that the rain clouds have no vertical extent, or at least that their vertical extent is very small in comparison to their horizontal scale of variability.

For nadir viewing, the above approximation is quite adequate. Several studies have shown that purely radiative effects of 3-D structure are not important in rain clouds at microwave wavelengths, on account of the relatively short optical paths involved.

For off-nadir viewing, geometric effects become an issue for any rain cloud which has an aspect ratio (cloud top height divided by horizontal dimension) much greater than zero. Deep convective cloud systems in the tropics may exhibit aspect ratios approaching unity. Furthermore, over water, the effective aspect ratio is doubled because of the reflected image of the cloud from the water surface.

The net result is that the satellite-observed microwave signatures of convective clouds may be dominated by emission from the sides (both direct and reflected) rather than tops of the clouds. In such a case, the local plane-parallel approximation (LPPA) is clearly invalid. However,

because so much depends on details of the assumptions about both cloud geometry and algorithm implementation, neither of which are completely known at this stage, it is not yet possible to quantify the retrieval performance penalty associated with a breakdown in the LPPA. This would require simulated retrievals, using the same methodology as the final algorithm, to be performed on simulated 2-D radiance fields corresponding to rain clouds possessing globally representative microphysical, optical, and geometric structure. Fully realistic simulations of this type cannot be undertaken in the time available. However, we expect to complete a much simpler set of simulations in the near future in order to elucidate the qualitative effect of cloud geometry on the retrievals.

The most important interaction between rain cloud geometry and incidence involves the phenomenon of parallax. Atmospheric emission originating near the surface is “seen” at its correct horizontal location (viewed along the line of sight from the satellite sub-point). Emission originating from an altitude H in the atmosphere appears to arise from a surface point further away than its true horizontal position. The magnitude of the apparent displacement is given by $H \cdot \tan(\theta)$.

Deep convective rain clouds routinely reach altitudes of 16 km or more. Microwave radiances originating from the top of such a cloud will be mapped to a surface location between 20 and 60 km away, for incidence angles between 50 and 75 degrees, respectively. If the cloud is positioned over a reflecting surface, like the ocean, then a similar parallax displacement occurs TOWARD the satellite for the reflected image of the cloud top. It follows that even an infinitely narrow convective column of height H will appear in microwave imagery as a feature having a horizontal dimension of $2H \cdot \tan(\theta)$. At 53.1 degrees, this overall stretching effect could be up to approximately 40 km or so; at 72.1 degrees, the smearing effect increases to almost 100 km, even before the blurring effect of the satellite antenna is applied.

Sample calculations of the cross-scan response of a microwave imager to an idealized cuboidal, non-scattering rain cloud are depicted in Figure 21. The horizontal and vertical dimensions of the rain cloud are 10 km, characteristic of many deep convective cells in the tropics. The nominal rain intensity is 20 mm/hr. In the figures, the vertical dashed lines depict the actual horizontal boundaries of the surface rainfall. The solid, unmarked curve depicts the associated normalized polarization at full resolution. The apparent width of the feature in this depiction is much wider than the actual rain cell. The spreading on the right side of the cell is due to the

reflection of the cell from the ocean surface; the spreading on the left side is the projection of the top of the cloud in the opposite direction along the line of sight. The total increase in the apparent rain cloud width is given by $2H \cdot \tan(\theta)$, and the distortion increases greatly for $\theta = 72.1$ degrees. The smooth curves marked with circles depicts the profile of P after convolution with the cross-scan antenna pattern for the channel in question. The circles themselves indicate how this convolved pattern would be sampled at 12.5 km intervals.

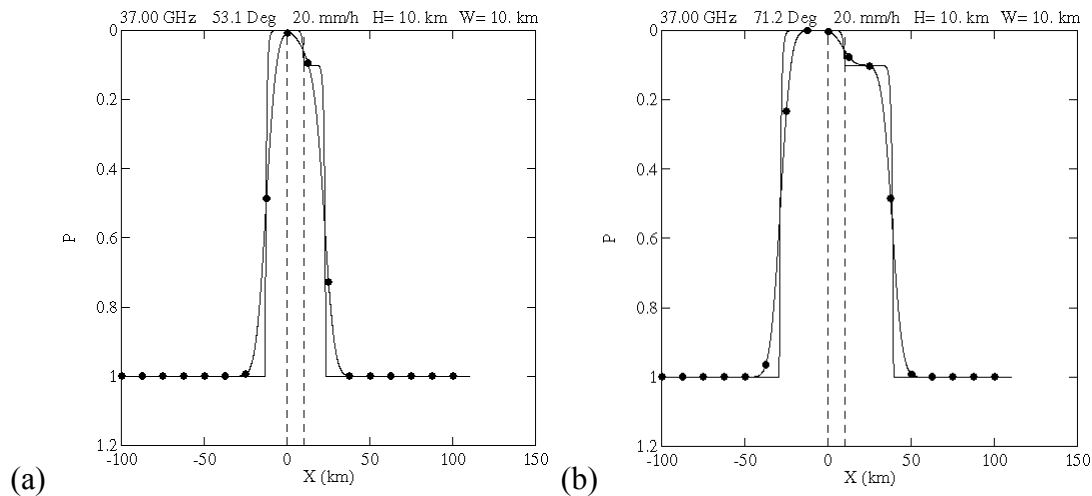


Figure 21: Precipitation geometry effects. The dashed lines mark the cloud extent; the plain solid curve marks the polarization index with infinitesimal resolution; the curve with dots marks the polarization index convolved with the cross-scan antenna pattern, where the dots are at 12.5 km intervals marking the sample spacing.

Simulated 1-D retrievals reveal that the area-average retrieved rain rate is not substantially affected by increasing the incidence angle. However, the parallax effect described above implies that the retrieved rainfall is distributed over a larger area than the true surface rainfall. Local retrieval errors are therefore large near the edges. The retrieval errors are not a strong function of incidence angles beyond 53.1 degrees.

3.6.3.2 Other Limiting Conditions

Certain surface types appear to pose an insurmountable obstacle to the passive microwave retrieval of precipitation in progress. In particular, no method or theory has yet been demonstrated for reliably distinguishing between surface snow cover and frozen precipitation aloft. Although the question is still under study, including the possible role of 166 GHz and other higher frequency channels, it may not be feasible to meet the threshold accuracy or precision requirements for precipitation rate estimates over snow or ice covered surfaces.

Over land it will generally be difficult or impossible to reliably detect rainfall from clouds lacking a significant ice phase component, as scattering due to raindrops alone is often too weak to be distinguished from other sources of brightness temperature variability. The global importance of rainfall from warm clouds remains uncertain; however the recent study of Petty (1998) suggests that warm rain may be climatologically significant in some regions.

3.7. Variance/Uncertainty Estimates

In order to evaluate global uncertainties, need to consider following sources of uncertainty

- Background emissivity
- Estimates of cloud-free brightness temperature within precipitation
- Statistics of variability in rain cloud structure and geometry
- Drop size and ice particle size, shape, density, fall speed
- Models for single scattering and extinction for liquid and frozen precipitation
- Models for dielectric coefficient of water and ice, especially low temperatures, high frequencies

3.8. Sensitivity Studies

Discussion of performance and error modeling, EDR performance stratification; conditions under which performance will not be met or degraded

4. Algorithm Calibration and Validation Requirements

4.1. Pre-launch

4.2. Post-launch

E.g., Train over-land algorithm using surface-blind sounder channels against over-water retrievals derived from more physically direct polarization signatures.

4.3. Special considerations for Cal/Val

4.3.1. Measurement hardware

4.3.2. Field measurements or sensors

4.3.3. Sources of truth data

5. Algorithm Processing Outline

5.1. Processing Flow for the specific algorithm

5.2. Input Data; algorithm output(s)

5.3. Dependencies and Processing Flow

5.4. CMIS data processing flow

5.5. Ancillary databases

5.6. Processing time benchmark data

6. Practical Considerations

6.1. Numerical Computation Considerations

6.2. Programming/Procedure Considerations

6.3. Computer hardware or software requirements

6.4. Quality Control and Diagnostics

6.5. Exception and Error Handling

6.6. Special database considerations

6.7. Special operator training requirements

6.8. Archival requirements

7. Constraints, Limitations, Assumptions

8. References

8.1. Government Documents and Communications

Specifications:

ICSRs and Responses:

8.2. HSC Documents

Specifications:

Memos:

8.3. Technical Literature

Adler, R.F., Kidd, C., Petty, G.W., Morrissey, M. and Goodman, M., 2001: Intercomparison of global precipitation products: The Third Precipitation Intercomparison Project (PIP-3). *Bull. Amer. Meteor. Soc.* (in press)

Beard, K.V, H. Ochs, J.Q. Feng, 1989, *Nature*, **342**, p 408

Bennartz, R. and Petty, G.W., 2001: The sensitivity of passive microwave radiances in precipitating clouds to ice particle size distributions. *J. Appl. Meteor.* (in press)

Bohren, C.F. and D.R. Huffman, 1983: *Absorption and Scattering of Light by Small Particles*. Wiley-Interscience, 530 pp.

Bruggeman, D.A.G., 1935: Berechnung verschiedener physikalischer Konstanten von heterogenen Substanzen: I. Dielektrizitätskonstanten und Leitfähigkeiten der Mischkörper aus isotropischen Substanzen. *Ann. Phys.*, **24**, 636-679

Conner, M.D., and G.W. Petty, 1998: Validation and intercomparison of SSM/I rain rate retrieval methods over the continental United States. *J. of Applied Meteorology*, **37**, 679-700

REFERENCES

- Deeter, M.N., and K.F. Evans, 1998: A hybrid Eddington-single scattering radiative transfer model for computing radiances from thermally emitting atmospheres. *J. Quant. Spectrosc. Radiat. Transfer*, **60**, 635-648
- Evans, K.F., and G.L. Stephens, 1991: A new polarized atmospheric radiative transfer model. *J. Quant. Spectrosc. Radiat. Transfer*, **46**, 413-423
- Evans, K.F., and G.L. Stephens, 1995: Microwave radiative transfer through clouds composed of realistically shaped ice crystals. Part I: Single scattering properties. *J. Atmos. Sci.*, **52**, 2041-2057
- Evans, K.F., and G.L. Stephens, 1995: Microwave radiative transfer through clouds composed of realistically shaped ice crystals. Part II: Remote Sensing of Ice Clouds. *J. Atmos. Sci.*, **52**, 2058-2072
- Evans, K.F., and J. Vivekanadan, 1990: Multiparameter radar and microwave radiative transfer modeling of nonspherical atmospheric ice particles. *IEEE Trans. Geosci. Remote Sensing*, **28**, 423-437
- Goedecke and O'Brien, 1988: Scattering by irregular inhomogeneous particles via the digitized Freen's function algorithm. *Applied Optics*, **27**, 2431-2437
- Grody, N.C., 1991: Classification of snow cover and precipitation using the special sensor microwave imager. *Journal of Geophysical Research*, **96**, 7423-7435
- Kohn, D.J., and T.T. Wilheit, 1995: *Refinement of a semi-empirical model for the microwave emissivity of the sea surface as a function of wind speed*. Master of Science thesis, Texas A&M University microwave group.
- Kummerow, C. and L. Giglio, 1994: A passive microwave technique for estimating rainfall and vertical structure information from space. Part I: Algorithm description. *Journal of Applied Meteorology*, **33**
- Kummerow, C., W.S. Olson and L. Giglio, 1996: A simplified Scheme for Obtaining Precipitation and Vertical Hydrometeor Profiles from Passive Microwave Sensors. *IEEE Transactions on Geoscience and Remote Sensing*, **34**, 1213-1232
- Lane J.A. and J.A. Saxton, 1952: Dielectric dispersion in pure polar liquids at very high radio frequencies. *Proc. Roy. Soc. Ser.*, **A.214**, 531-545
- Lenoble, J. 1985: *Radiative Transfer in Scattering and Absorbing Atmospheres: Standard Computation Techniques*. A. Deepak Publishing, Hampton, VA, 300 pp.
- Liebe, H.J., and D.H. Layton, 1987: Millimeter-wave properties of the atmosphere: Laboratory studies and propagation modeling. *NTIA rep. 87-224*, Natl Commun. And Inf. Admin., Boulder, Colo.

REFERENCES

- Liebe, H.J., G.A. Hufford and M.G. Cotton, 1993: Propagation modeling of moist air and suspended water/ice particles at frequencies below 1000 GHz. *Reprints of the AGARD 52nd Specialist's Meeting of the Electromagnetic Wave Propagation Panel*, Palma de Mallorca, Spain
- Liebe, H.J., G.A. Hufford and T. Manabe, 1991: Model for the complex permittivity of water at frequencies below 1 THz. *Int. J. Infrared Millimeter Waves*, **12**, 659-670
- Marshall, J.S. and W.H. Palmer, 1948: The distribution of raindrops with size. *J. Meteor.*, **5**, 165-166
- Maxwell Garnett, J.C., 1904: Colours in metal glasses and in metallic films. *Philos. Trans. Roy. Soc.*, **203A**, 385-420
- Moncet, J.L., and S.A. Clough, 1997: Accelerated monochromatic radiative transfer for scattering atmospheres: Application of a new model to spectral radiance observations. *J. Geophys. Research*, **102**, 21853-21866
- Petty, G.W., Chiu, J.-Y., and Johnson, B., 1999: Microwave radiances in extratropical precipitation. Poster presentation at the TRMM Science Team Meeting, November 1999.
- Petty, G.W. and Katsaros, K.B., 1994: The response of the SSM/I to the marine environment. Part II: A parameterization of the effect of the sea surface slope distribution on emission and reflection. *Journal of Atmospheric and Oceanic Technology*, **11**, 617-628
- Petty, G.W. and N. Gautam, 2001: Physical and microwave radiative properties of precipitating clouds. Part 3. Passive microwave retrieval of effective hydrometeor profiles and properties in tropical stratiform rainfall. *J. Applied Meteorology* (to be submitted)
- Petty, G.W. and Turk, F.J., 1993: Observed multichannel microwave signatures of spatially extensive precipitation in tropical cyclones. *Preprints, 8th Conference on Satellite Meteorology and Oceanography*, Atlanta, Georgia, 28 January – 2 February }
- Petty, G.W., 1994a: Physical retrievals of over-ocean rain rate from multichannel microwave imagery. Part I: Theoretical characteristics of normalized polarization and scattering indices. *Meteorology and Atmospheric Physics*, **54**, 79-100
- Petty, G.W., 1994b: Physical retrievals of over-ocean rain rate from multichannel microwave imagery. Part II: Algorithm implementation. *Meteorology and Atmospheric Physics*, **54**, 101-121
- Petty, G.W., 1995a: Frequencies and characteristics of global oceanic precipitation from shipboard present-weather reports. *Bull. American Meteorological Society*, **76**, 1593-1616
- Petty, G.W., 1995b: The status of satellite-based rainfall estimation over land. *Remote Sensing of the Environment*, **51**, 125-137

REFERENCES

- Petty, G.W., 1997: An intercomparison of oceanic precipitation frequencies from 10 SSM/I rain rate algorithms and shipboard present-weather reports. *J. Geophysical Research*, **102**, 1757-1777
- Petty, G.W., 1999: The prevalence of precipitation from warm-topped clouds over Eastern Asia and the Western Pacific. *J. Climate*, **12**, 220-229
- Petty, G.W., 2001a: Physical and microwave radiative properties of precipitating clouds. Part 1. Principal component analysis of observed multichannel microwave radiances in tropical stratiform rainfall. *J. of Applied Meteorology* (accepted pending minor revision)
- Petty, G.W., 2001b: Physical and microwave radiative properties of precipitating clouds. Part 2. A parametric stratiform rain cloud model for use in microwave radiative transfer simulations. *J. of Applied Meteorology* (accepted pending minor revision)
- Petty, G.W., A. Mugnai and E.A. Smith, 1994: Reverse Monte Carlo simulations of microwave radiative transfer in realistic 3-D rain clouds. *Preprint Volume, Conference on Satellite Meteorology and Oceanography*, Monterey, California, 6-10 June
- Petty, G.W., and Katsaros, K.B., 1992: Nimbus-7 SMMR precipitation observations calibrated against surface radar during TAMEX. *Journal of Applied Meteorology*, **31**, 489-505
- Petty, G.W., and Katsaros, K.B., 1990: Precipitation observed over the South China Sea by the Nimbus-7 scanning multichannel microwave radiometer during winter MONEX. *Journal of Applied Meteorology*, **29**, 273-287
- Petty, G.W., and Katsaros, K.B., 1992: The response of the SSM/I to the marine environment. Part I: An analytic model for the atmospheric component of observed brightness temperatures. *Journal of Atmospheric and Oceanic Technology*, **9**, 746—761
- Petty, G.W., and W. Krajewski, 1996: Satellite rainfall estimation over land. *Hydrological Sciences J.*, **41**, 433-451
- Pruppacher, H.R. and Klett, J.D., 1997: *Microphysics of Clouds and Precipitation (2nd Ed.)*. Kluwer Academic Publishers, 954 pp.
- Ray, P.S. 1972: Broadband complex refractive indices of ice and water. *Appl. Opt.*, **11**, 1836-1844.
- Reisner, J., R. M. Rasmussen, and R. T. Bruintjes, 1998: Explicit forecasting of supercooled liquid water in winter storms using the MM5 mesoscale model. *Q. J. R. Meteo. Soc.*, **124**, 1071-1107.
- Roberti, L., Haferman, J., Kummerow, C., 1994: Microwave radiative transfer through horizontally inhomogeneous precipitating clouds. *J. Geophys. Res.*, **99**, 16,707-16,718

REFERENCES

- Rosenkranz, P.W., 1998: Water Vapor Microwave Continuum Absorption: A Comparison of Measurements and Models, *Radio Science*, **33**, 919-928
- Rothman L.S. et al., 1992: The HITRAN molecular database: Editions of 1991 and 1992, *J. Quant. Spectrosc. Radiat. Transfer*, **48**, 469-507
- Sekhon, R.S. and Srivastava, R.C., 1970: Snow size spectra and radar reflectivity. *J. Atmos. Sci.*, **27**, 299-307
- Smith, E.A., H.J. Cooper, G.J. Tripoli and X. Xiang, 1992: Foundations for statistical-physical precipitation retrieval from passive microwave satellite measurements. Part I: Brightness temperature properties of a time-dependent cloud radiation model. *Journal of Applied Meteorology*, **31**, 506-531
- Smith, E.A., Xiang, X., Mugnai, A., and Tripoli, G.J., 1994: Design of an inversion-based precipitation profile retrieval algorithm using an explicit cloud model for initial guess microphysics. *Meteorology and Atmospheric Physics*, **54**, 53-78
- Spencer, R.W., B.B. Hinton and W.S. Olson, 1983: Nimbus-7 37 GHz radiances correlated with radar rain rates over the Gulf of Mexico. *J. Climate Appl. Meteor.*, **22**, 2095-2099
- Spencer, Roy W., 1986: Satellite passive 37-GHz scattering-based method for measuring oceanic rain rates. *Journal of Climate and Applied Meteorology*, **25**, 754-766
- Spencer, Roy W., Goodman, H. Michael, and Hood, Robbie E., 1989, Precipitation retrieval over land and ocean with the SSM/I: identification and characteristics of the scattering signal. *Journal of Atmospheric and Oceanic Technology*, **6**, 254-273
- Stamnes K., S.C. Tsay, W.J. Wiscombe and K. Jayaweera, 1988: Numerically stable algorithm for discrete-ordinate-method radiative transfer in multiple scattering and emitting layered media. *Appl. Opt.*, **27**, 2502-2509
- Tao, W.-K., and J. Simpson, 1993: The Goddard Cumulus Ensemble Model. Part I: Model description. *Terr. Atmos. Ocean. Sci.*, **4**, 35-72.
- Turk et al. 1999? (modeling polarization from conical graupel – need ref.)
- Warren, S.G., 1984: Optical constants of ice from the ultraviolet to the microwave. *Applied Optics*, **23**, 1206-1225
- Wilheit, T. T., 1977: Satellite technique for quantitatively mapping rainfall rates over the oceans. *Journal of Applied Meteorology*, **16**, 551-560
- Wilheit, T.T. , 1979: A model for the microwave emissivity of the ocean's surface as a function of wind speed. *IEEE Trans. Geosci. Electron.*, **GE-17**, 244-249
- Wilheit, Thomas T., 1986: Some comments on passive microwave measurement of rain. *Bulletin of the American Meteorological Society*, **67**, 1226-1232

REFERENCES

This page intentionally left blank.

LIST OF ACRONYMS

ADD	Algorithm Description Document
AER	Atmospheric and Environment Research, Inc.
AGL	Above Ground Level
ALFA	AER Local Area Forecast Model
AMS	American Meteorological Society
AMSR	Advanced Microwave Scanning Radiometer
AMSU	Advanced Microwave Sounding Unit
APOLLO	AVHRR Processing Scheme Over Cloud Land and Ocean
APS	Algorithm Performance Simulation
ARA	Atmospheric Radiation Analysis
ARD	Algorithm Requirements Document
ARM	Atmospheric Radiation Measurement
ASRR	Algorithm System Requirements Review
ASTER	Advanced Spaceborne Thermal Emission and Reflection Radiometer
ATBD	Algorithm Theoretical Basis Document
ATOVs	Advanced TOVS
AVHRR	Advanced Very High Resolution Radiometer
BT	Brightness Temperature
CC	Cloud Clearing
CEPEX	Central Equatorial Pacific Experiment
CF	Central frequency
CHARTS	Code for High resolution Accelerated Radiative Transfer with Scattering
CKD	Clough, Kneizys and Davies
CLW	Cloud Liquid Water
CMIS	Conical Microwave Imaging Sounder
COD	Cloud Optical Depth
CTH	Cloud Top Height
CTP	Cloud Top Pressure
DEM	Digital Elevation Model
DMSP	Defense Meteorological Satellite Program
DoD	Department of Defense
DOE	Department of Energy
EDR	Environmental Data Record
EIA	Earth Incidence Angle
EOF	Empirical Orthogonal Function
EOS	Earth Observing System
ESFT	Exponential Sum Fitting Technique
FFT	Fast Fourier Transform
FIRE	First ISCCP Regional Experiment
FOR	Field Of Regard
FOV	Field Of View
GPS	Global Positioning System
GSFC	Goddard Space Flight Center
HH	Hole Hunting
HIRS	High-resolution Infrared Sounder

LIST OF ACRONYMS

HSR	Horizontal Spatial Resolution
IFOR	Instantaneous Field Of Regard
IFOV	Instantaneous Field Of View
ILS	Instrument Line Shape
IPO	Integrated Program Office
IPT	Integrated Product Team
IST	Ice Surface Temperature
IWVC	Integrated Water Vapor Content
JHU	Johns Hopkins University
JPL	Jet Propulsion Laboratory
LA	Lower Atmosphere
LAT	Latitude
LBL	Line By Line
LBLRTM	Line By Line Radiative Transfer Model
LMD	Laboratoire de Météorologie Dynamique
LON	Longitude
LOS	Line Of Sight
LST	Land Surface Temperature
L-V	Levenberg-Marquardt
LVM	Levenberg-Marquardt
MHS	Microwave Humidity Sounder
ML	Maximum Likelihood
MODIS	Moderate-Resolution Imaging Spectrometer
MODTRAN	Moderate Resolution Transmittance Code
MSU	Microwave Sounding Unit
MW	Microwave
NASA	National Aeronautics and Space Administration
NCAR	National Center for Atmospheric Research
NCEP	National Center for Environmental Prediction
NDSI	Normalized Difference Snow Index
NDVI	Normalized Difference Vegetation Index
NEDN	Noise Equivalent Difference
NESDIS	National Environmental Satellite, Data, and Information Service
NN	Neural Network
NOAA	National Oceanic and Atmospheric Administration
NPM	Numerical Prediction Model
NPOESS	National Polar-orbiting Operational Environmental satellite System
NRL	Naval Research Laboratory
NWP	Numerical Weather Prediction
OD	Optical Depth
OI	Optimal Interpolation
OLS	Operational Linescan System
OMIS	Operational Multi-Spectral Imaging Suite
OMPS	Ozone Mapping and Profiler Suite
OSS	Optimal Spectral Sampling
PCA	Principal Component Analysis
PDR	Preliminary Design Review
PSD	Power Spectral Density
POES	Polar Orbiting Environmental Satellite

LIST OF ACRONYMS

Psfc	Surface Pressure
PSURF	Surface Pressure
QC	Quality Control
RDR	Raw Data Records
RH	Relative Humidity
RMS	Root Mean Square
RMSE	Root Mean Square Error
RRTM	Rapid Radiative Transfer Model
RT	Radiative Transfer
RTA	Radiative Transfer Algorithm
RTE	Radiative Transfer Equation
RTM	Radiative Transfer Model
S/N	Signal/Noise
SAR	Synthetic Aperture Radar
SCPR	Simultaneous Cloud Parameter Retrieval
SDR	Sensor Data Record
SEIT	System Engineering Integrated Product Team
SFR	System Functional Review
SGI	Silicon Graphics, Inc.
SPS	System Performance Simulation
SRD	Sensor Requirement Document
SRR	System Requirements Review
SSM/I	Special Sensor Microwave/Imager
SSM/T	Special Sensor Microwave/Temperature
SSMIS	Special Sensor Microwave Imager Sounder
SST	Sea Surface Temperature
SVD	Single Value Decomposition
SW	Shortwave
T	Temperature
TBD	To Be Determined (by contractor)
TBR	To Be Resolved (by contractor/government)
TBS	To Be Supplied (by government)
TIGR	TOVS Initial Guess Retrieval
TIM	Technical Interchange Meeting
TOA	Top Of Atmosphere
TOD	Time of Day
TOVS	TIROS-N Operational Vertical Sounder
TRD	Technical Requirements Document
TSKIN	Skin Temperature
UA	Upper Atmosphere
UR	Unified Retrieval
USGS	United States Geological Survey
VIIRS	Visible/Infrared Imager/Radiometer Suite
Vis	Visible
WPTB	Weather Product Test Bed
WV	Water Vapor
WVF	Water Vapor Fraction

LIST OF ACRONYMS

This page intentionally left blank.